Manuela Sornig

Investigations of Upper Atmosphere Dynamics on Mars and Venus by High Resolution Infrared Heterodyne Spectroscopy of CO_2

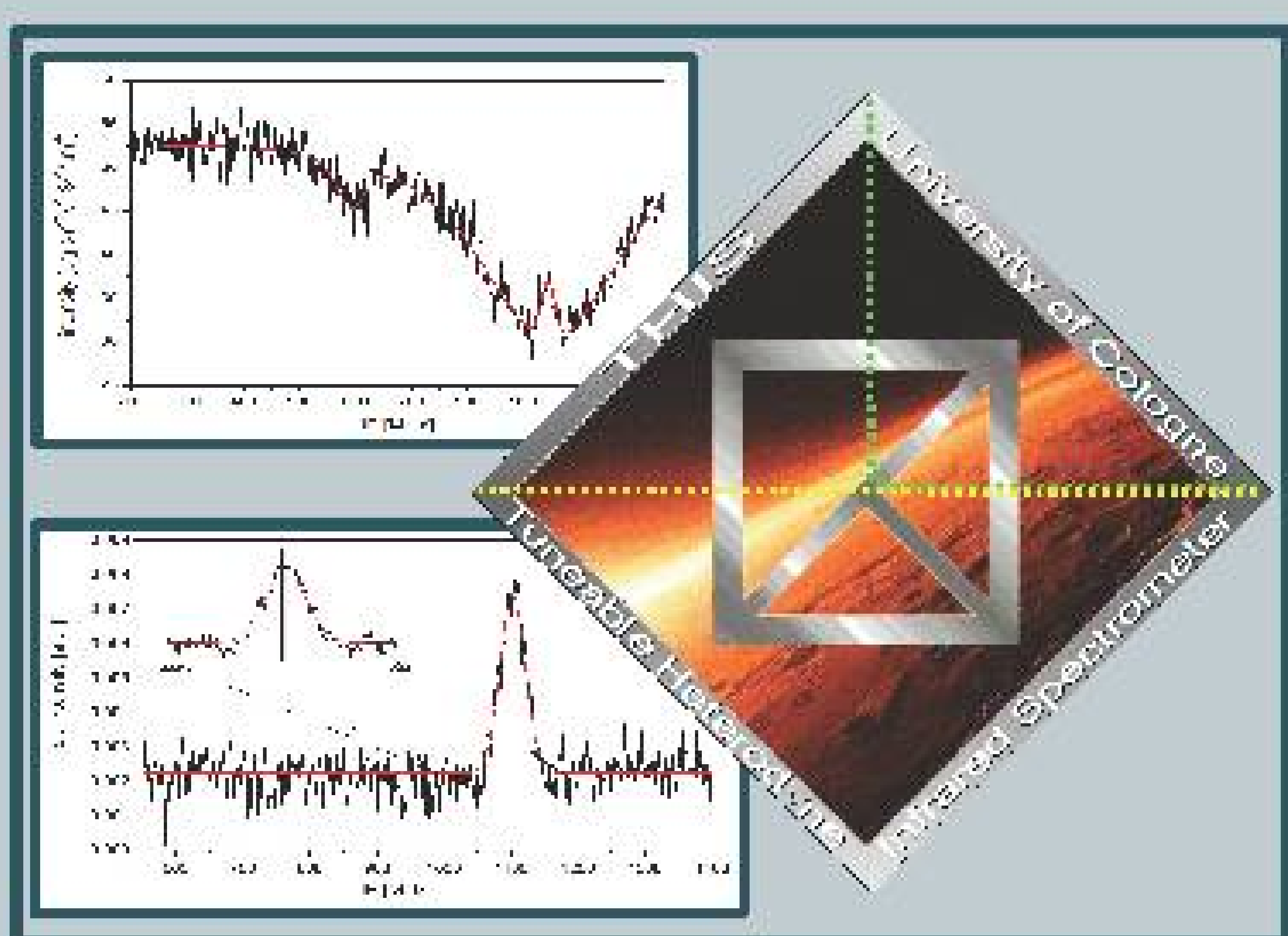

Physik

Investigations of Upper Atmosphere Dynamics on Mars and Venus by High Resolution Infrared Heterodyne Spectroscopy of CO_2

Inaugural-Dissertation

zur

Erlangung des Doktorgrades

der Mathematisch-Naturwissenschaftlichen Fakultät

der Universität zu Köln

vorgelegt von

Manuela Sornig

aus Schladming

2009

Bibliografische Information der Deutschen Nationalbibliothek
Die Deutsche Nationalbibliothek verzeichnet diese Publikation in der Deutschen Nationalbibliografie; detaillierte bibliografische Daten sind im Internet über http://dnb.ddb.de abrufbar.
1. Aufl. - Göttingen : Cuvillier, 2009
Zugl.: Köln, Univ., Diss., 2009

978-3-86727-873-7

Berichterstatter:

Prof. Dr. R. Schieder
Priv.-Doz. Dr. M. Pätzold

Tag der letzten mündlichen Prüfung: 09. Jänner 2009

Nonnenstieg 8, 37075 Göttingen
Telefon: 0551-54724-0
Telefax: 0551-54724-21
www.cuvillier.de

1. Auflage, 2009
Gedruckt auf säurefreiem Papier

978-3-86727-873-7

Contents

List of Figures

List of Tables

Abstract (German)

Ein gutes Verständnis planetarer Atmosphären ist eine Grundvoraussetzung zur Entwicklung von Prognosemodellen. Vorhersagen aus diesen Modellen wiederum tragen wesentlich zum globalen Verständnis dieser Atmosphären bei. Ausgehend von Modellen für die Erdatmosphäre hat die Anpassung und Entwicklung dieser Modelle für Mars und Venus in den letzten Jahren große Fortschritte gemacht.

Wesentlichen Einfluss hatten dabei verbesserte Beobachtungsmöglichkeiten und Raumfahrtmissionen. Zum einen werden Orientierungsdaten für die Parametrisierung benötigt und zum anderen bedürfen Modelle der Bestätigung durch Messwerte. Erdgebundene Beobachtungen insbesondere in höheren Bereichen der Atmosphäre sowie Langzeitbeobachtungen sind daher eine wichtige und kostengünstige Ergänzung zu Weltraummissionen, um Modellvorhersagen zu überprüfen und zukünftige Missionen vorzubereiten.

Eine elegante Methode zur sonst nur schwer möglichen direkten Messung von Windgeschwindigkeiten ist die Beobachtung von nicht-thermischen CO_2 Emissionslinien im Infrarotbereich mit Frequenz hochauflösender Heterodynspektroskopie. Aus beobachteten Dopplerverschiebungen der Frequenzen dieser Linien kann direkt auf die Geschwindigkeiten der CO_2 Moleküle rückgeschlossen werden. Im Unterschied zu Beobachtungen im Radio-Wellenlängenbereich kann im Infraroten auch die notwendige hohe räumliche Auflösung erreicht werden. Zudem ist die ermittelte Windgeschindigkeit der einzelnen Positionen am Planeten unabhängig von zusätzlichen Informationen wie Temperatur- und Druckprofilen.

Ein derartiges Infrarot Heterodyn Empfängersystem mit dem Namen THIS (Tuneable Heterodyne Infrared Spectrometer) wurde am I. Physikalischen Institut der Universität Köln aufgebaut und im Rahmen dieser Arbeite weiterentwickelt, sodass nunmehr regelmässige Beobachtungen der Mars- und Venusatmosphäre mit diesem Instrument möglich sind.

Die Ergebnisse von Windmessungen in den Atmosphären von Mars und Venus aus insgesamt vier Beobachtungskampagnen im Zeitraum von 2005 bis 2008 werden in dieser Arbeit präsentiert. Die Messungen wurden so weit wie möglich in Koordination mit anderen Beobachtungstechnicken durchgeführt und sowohl mit deren Resultaten als auch mit Modellergebnissen verglichen.

Bei Resultaten der Venusbeobachtung stand dabei der Vergleich mit anderen Beobachtungsmethoden, vor allem innerhalb der "Coordinated ground-based campaign to support Venus Express" im Vordergrund, da für Venus noch keine verlässlichen Modellergebnisse in der höheren Atmosphäre zur Verfügung stehen. Die gemessenen Werte sind im Vergleich zu anderen Beobachtungen grundsätzlich etwas niedriger und im Gegensatz zu diesen konnte nur eine moderate zeitliche Variabilität festgestellt werde.

Im allgemeinen hat die koordinierte Beobachtungskampage gezeigt, daß die Dynamik der Venusatmosphäre viel komplexer ist, als bisher angenommen. Daher sind zusätzliche Daten besonders bzgl. zeitlicher Variabilität von Windgeschwindigkeiten notwendig. Weitere Messkampagnen mit THIS sind bereits geplant.

Im Gegensatz zu Venus liefern Marsmodelle hingegen mittlerweile sehr detaillierte Informationen bezüglich verschiedenster atmosphärischer Parameter. Die Resultate unserer Beobachtungen konnten die Vorhersagen eines Models vom Laboratoire de Météorologie Dynamique du CNRS(Paris) in weiten Bereichen bestätigen. Bei Auswertung und Interpretation der Daten wurde dabei hohen Wert auf die Zusammenarbeit mit Modellierern gelegt. Es hat sich gezeigt, dass Messungen mit THIS für eine noch detailliertere Überprüfung der Modelle in Zukunft einsetzbar sind.

Abstract (English)

Understanding of the physical and chemical processes in planetary atmospheres is essential for the development of general circulation models (GCM) and meteorological forecast models. Adopting Earth models to the atmospheres of Mars and Venus has been improved substantially over the last few years due to constraints imposed by improved technology of ground-based observations and data that became available from several space missions.

Observational constraints of the models especially at high altitudes are needed for parametrization and validation. These data can only partially be provided by spacecrafts. Earth-based observations in other atmospheric regions or long term observations are a necessary and cost-efficient complementary observational method to constrain the models and to prepare for future space missions and landers.

An elegant method to measure high atmospheric winds is by observing infrared CO_2 absorption and emission lines with high spectral resolution heterodyne spectroscopy. From line frequency (Doppler)shifts velocities of the emitting and absorbing gas can be directly deduced. In contrast to microwave observations an adequate spatial resolution can be achieved in addition to the high spectral resolution with the infrared heterodyne observing technique. Therefore the retrieved wind velocities at each observed position on the planet are independent from additional assumptions like temperature or pressure profiles.

Such an infrared heterodyne instrument named THIS (Tuneable Heterodyne Infrared Spectrometer) has been developed at the I. Physikalisches Institut at the University of Cologne and has been improved within this work to a level where regular observations of the Martian and Venusian atmosphere are now possible.

Wind velocities measured in the atmospheres of Mars and Venus during four observation runs within a time period from 2005 to 2008 are presented in this work. Observations were accomplished in coordination with other observing techniques and results are compared with them as well as with output parameters of model calculations.

For Venus observations mainly comparison with results from other ground-based observations, in particular within the coordinated ground-based campaign 2007 to support Venus Express, are made due to a lack of reliable model results at higher altitudes. Measured wind values in general are lower than those from other observing techniques and compared to them only a moderate variability with time was observed.

The coordinated ground-based campaign generally showed that the dynamic in the Venusian atmosphere is much more complex than believed before. Hence additional data especially concerning temporal variability of wind velocities are needed. Further observing campaigns with THIS are already in preparation.

On the contrary global circulation models of the Martian atmosphere have already reached a high level and provide detailed information about various atmospheric parameters. The results of our wind observation validate the predictions of one models developed at the Laboratoire de Météorologie Dynamique du CNRS (Paris) over wide range. Data analysis and data interpretation emphasized exchange with modelers and it has been shown that measurements with THIS are a valuable tool for the future to validate and proof these models even in more detail.

Chapter 1

"If you thought that science was certain - well, that is just an error on your part." (Richard Feynman (1918-1988), American Physicist)

Introduction

Knowledge about properties and processes that shape conditions on Earth gives us the ability to arrange our lives to them. To know about natural[h] potentials (e.g. energy generation, natural resources), to predict conditions (e.g. weather forecast, natural disasters, climate changes) and to understand correlations is the base to use our planet without abusing it.

The arising question now is: "What could be the reason to study other planets?".

- Knowledge about other planets will increase the understanding of our own planet. The physics behind processes on different planets are the same as on Earth. They are determined by parameters like characteristic location in the solar system, specific spin/orbital dynamics, chemical composition and distribution, geological properties and activity, energy budget, etc. Studying other planets will lead to $crossfertilization$ of ideas between different planetary environments.

- The description of a global system like the climate is established by complex models. The precision of such models is especially important if predictions are needed (e.g. forecast). Application of the same modeling methodology to more than one planet with enough "common ground" between them opens a new field for validation and verification and leads to a better understanding of the entire system.

- Eventually, we will need to extend our living space beyond the planet Earth. Therefore the exploration of our solar system neighborhood is mandatory.
- And not to forget there is the natural human "thirst for knowledge" which has always and will always motivate mankind to explore and to find answers to open questions.

Therefore, studying other planets is important for a comprehensive understanding of nature and future environmental developments.

The closest planets which can be addressed are Venus and Mars. Having solid bodies surrounded by a thin layer of atmosphere, Venus, Mars and Earth are called the terrestrial planets. Though different in many ways they show several likenesses. Some relevant parameters are listed in Tab. 1.1.

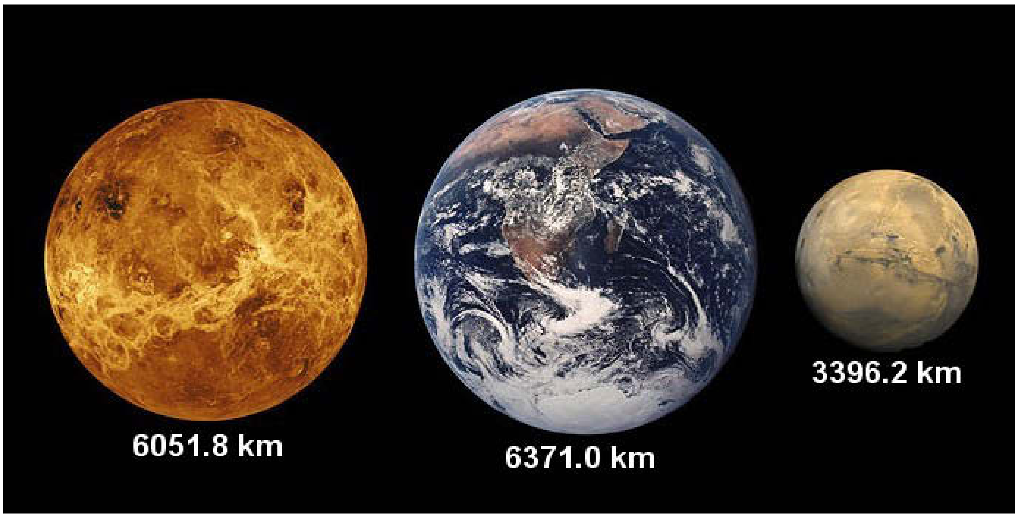

Figure 1.1: *Shown are the terrestrial planets Venus, Earth and Mars (from left to right). The mean radius of the planets are given. Realistic relative sizes are pictured for comparison (NASA [1]).*

Venus and Earth have almost the same size whereas the Martian radius is half of the others. The axial tilt of Mars and Earth is substantial and similar causing e.g. seasonal changes while Venus is more or less upside down with only a small inclination to the ecliptic. Also, Venus is the only planet in the solar system to rotate retrograde, i.e. versus its orbital rotation. The orbital rotation period of Venus is very long (243 Earth

Table 1.1: *Overview of important orbital, physical and atmospheric properties of the terrestrial planets Venus, Earth and Mars.*

Orbital Properties			
	Venus	Earth	Mars
semi-major axis	108 208 930 km	152 097 701 km	227 939 100 km
orbital period (year)	224.70 days	365.256 days	686.971 days
synodic period	583.92 days	-	779.96 days
inclination	3.39471 deg	0 deg	1.850 deg
Physical Properties			
	Venus	Earth	Mars
mean radius	6051.8 km	6371.0 km	3396.2 km
	0.9499 Earths		0.533 Earths
heliocentric distance	0.72 AU	1 AU	1.52 AU
surface temperature	737 K	297 K	210 K
solar day	117 days	24 h	24 h 40 min
axial tilt	177.36deg	23.439281deg	25.19deg
apparent magnitude	up to -4.6	-	+1.8 – -2.91
angular diameter	9.7″-66.0″	-	3.5″ – 25.1″
Atmospheric Properties			
	Venus	Earth	Mars
surface pressure	93 000 mbar	1000 mbar	6.9 mbar
major components	$\sim$96.5 % CO_2	$\sim$78.08 % N_2	$\sim$95.3 % CO_2
	$\sim$3.5 % N_2	$\sim$20.95 % O_2	$\sim$2.7 % N_2
	$\sim$.015 % SO_2	$\sim$.93 % Ar	$\sim$1.6 % Ar
	etc.	$\sim$.083 % CO_2	$\sim$.2 % O_2
		etc.	etc.

days) and in combination with its synodic period resulting in a Venusian solar day of 117 Earth days compared to Earth and Mars days of $\sim$ 24 h.

The environments of the three planets differ drastically. Venus is a hot planet with high surface pressure and a dense atmosphere containing sulfur dioxide. On Mars we find very cold temperatures and a thin atmosphere with low surface pressure. In spite of their different atmospheric parameters the major constituents and their mixing ratios are almost identical on Venus and Mars (mostly CO_2) differing completely from the atmospheric composition on Earth.

General Circulation Models (GCMs) have been developed for the Earth's atmosphere and were later adopted to Mars and Venus. These models improved the general understanding of atmospheric processes but especially one of the key parameters, the dynamic is still not very well understood. Validation of the output values generated by this models is necessary and measurements of atmospheric parameters are therefore needed. Besides occultation observations (at radio and UV wavelength), spectroscopy (in the infrared, microwave and UV region) is widely used as a remote sensing method to gain information about atmospheres of distant objects.

In recent years IR heterodyne spectroscopy has emerged as a powerful tool for atmospheric studies. Many useful information was gathered in the Earth's atmosphere as well as in the atmospheres of other solar system objects [2, 3, 4, 5, 6, 7, 8, 9, 10, 11, 12]. Whenever highest spectral resolution is required heterodyne systems are advantageous because of their high optical throughput compared to direct detection methods like grating spectrometers or Fourier-Transform-Spectroscopy [2, 13, 14].

So far mostly gas lasers (CO_2 lasers) have been used as local oscillators (LO) in infrared heterodyne systems [15, 10]. The main restriction to such instruments is imposed by the fixed gas laser frequencies. Given a typical detector bandwidth of 2 GHz observations are only possible within this small interval around the few laser lines available so that only about 15 % of the spectral range between 9 and 12 μm can be observed this way [15].

This major limitation was overcome by tuneable lead salt diode lasers (TDL) which are commercially available at emission wavelengths ranging from 1 to 34 μm [16]. These lasers were implemented to the Cologne heterodyne receiver THIS (Tuneable Heterodyne Infrared Spectrometer) several years ago. Unfortunately, the system noise temperature of advanced TDL pumped systems proved to be worse by a factor of 3–5 compared to gas laser instruments which is due to the lack of power, incoherent background emission, and the critical response of TDLs to optical feedback [15, 10, 17, 18, 11, 19]. Only recently, quantum cascade lasers (QCL) became available as local oscillators for heterodyne systems. They provide sufficient optical power to reach the shot-noise detection limit and convenient handling compared to TDLs. The use of QCLs improved the performance of the heterodyne receiver THIS to the level of CO_2 laser based systems and made it competitive and with respect to wavelength coverage even advantageous. A detailed description of the parameters and properties of the QCL-LOs used in our system can be found in Sonnabend et al. [20] and Wirtz [21].

The instrument THIS is easily transportable and therefore widely usable at Cassegrain, Nasmyth or Coudé foci of IR or optical telescopes (see chapter 4) and is intended to be a 2nd generation instrument for the airborne observatory SOFIA. In addition interferometric applications are feasible which would then require at least two identical receivers and phase-locked LOs.

Chapter 2

"It often is more spirit and brilliance in a mistake than in a discovery." (Joseph Joubert (1754-1824), French Author)

Dynamics in Planetary Atmospheres

General Circulation Models (GCMs) are commonly used to predict weather and climate of planets and they are a widely used tool for meteorological research. A set of partial differential equations (PDEs) of fluid mechanics can describe the motion of an atmosphere. Theoretically an exact solution exists though solving the equations is limited by computing power. In addition, initialization and boundary conditions at any particular location and time are not known exactly. Therefore, many approximations and assumptions have to be made in order to produce a closed dynamical system.

Attempts to apply terrestrial GCMs to Mars and Venus were made from the beginning. Validation of these models through measurements are obviously much harder to perform than on Earth. Only in recent years with increasing data from ground-based and space-based observations these models and with them our knowledge about atmospheric conditions improved significantly. In the following chapter some historical aspects and the current knowledge about the atmospheric conditions on Venus and Mars with emphasis on their dynamical properties are presented. In addition a brief overview of the general circulation in the Earth's atmosphere is given.

2.1 Dynamics in the Venusian Atmosphere

During the transit of Venus across the Sun on June 6^{th} 1761 the blurriness of the disc was assigned to the existence of an atmosphere by Mikhail Lomonosov. This theory was confirmed later on with the increase in quality of observations. For many years information about the atmosphere and the dynamics was gathered exclusively by ground-based observations. The presence of CO_2 for example was established in 1932 using infrared-sensitive photographic plates [22]. Little more was discovered until 1958 when radio astronomers found much higher surface temperatures than expected. These observations at microwave wavelength of 3.15 cm indicated an extreme version of the greenhouse effect [23], a theory confirmed by observations of following space missions (see 2.2).

A large number of missions have been devoted to study the atmosphere of Venus. NASA started missions to Venus in 1962 with Mariner 2, 5 and 10, flybys followed by the Pioneer Venus Orbiter and Multiprobe in 1978. A windless environment with almost no temperature variation due to high thermal capacity of the massive atmosphere at the surface of Venus was found by the Pioneer Landers.

First dynamical observations at higher altitudes in the atmosphere of Venus were accomplished from the Earth and yielded astonishing results [24, 25]. Near UV imaging measurements detected a 4 day superrotation (see Fig.2.1 [26]) resulting in high wind velocities of $\sim$110 m/s near the equator compared to a sidereal rotation period of 243 days of the planet causing a equatorial rotation velocity of only $\sim$2 m/s.

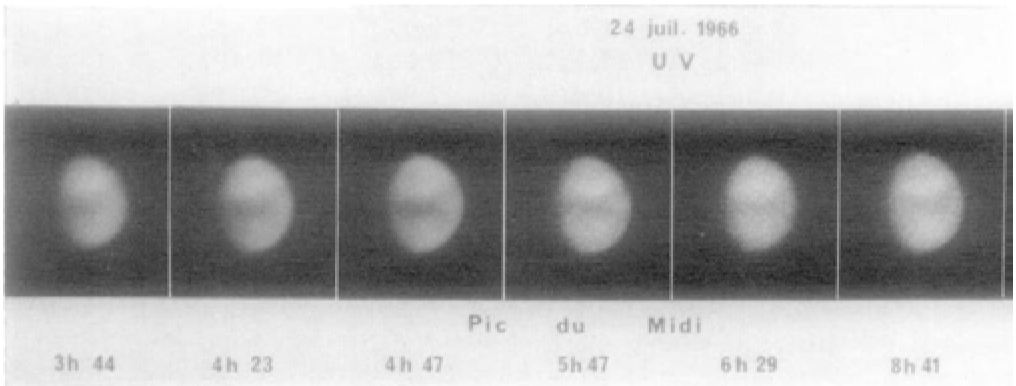

Figure 2.1: *Excerpt of UV observations of the rotation of Y shaped cloud formation observed in 1966 by Boyer and Guérin [26] yielding the 4 day superrotation.*

These patterns where supported by more recent Pioneer Venus Orbiter observations. Profiles of zonal and meridional winds at selected locations on Venus [27, 28, 29, 30, 31] and temporal snapshots of horizontal and vertical wind velocities [32, 33, 34, 35, 36, 37, 38] were yielded by entry probes and ground-based measurements. Later on also the Jupiter-bound spacecraft Galileo took pictures of cloud circulation during flyby. In 1991 the spacecraft Magellan retrieved first temperature profiles (shown in Fig. 2.2) and pressure profiles.

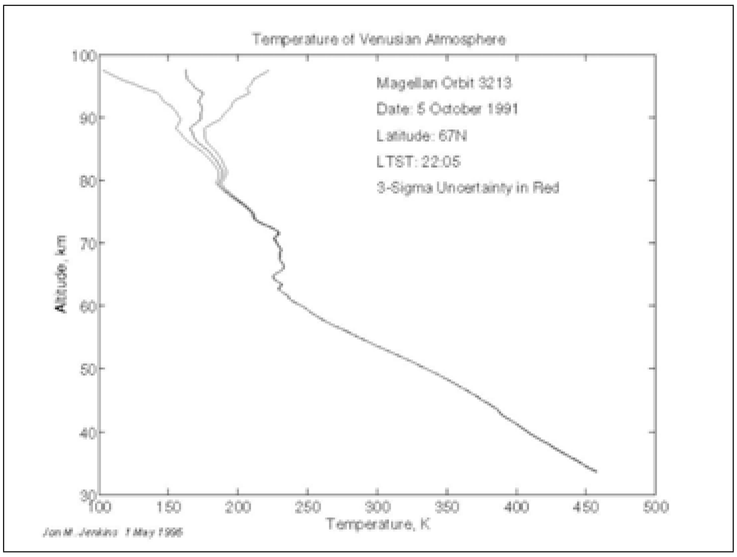

Figure 2.2: *Venus temperature profile measured by the spacecraft Magellan in 1991.*

Also the Soviet Union launched orbiters, flybys, descent and entry probes with Venera 4 – 14 and the radar mapper Venera 15 and 16 followed by VeGa 1 and 2.

Currently, ESA's orbiter Venus Express (launched Nov. 2005) supplies scientists with astonishing new data providing new insights into atmospheric conditions and leading to new theories. Fig. 2.3 shows recently published [39] temperature profiles from radio-sounding observations with Venus Express Radio Science Experiment (VeRa) from 2006.

In addition, the Japan Aerospace Exploration Agency (JAXA) is building the Venus Climate Orbiter VCO (to be launched in 2010) to study the atmospheric properties of Venus with emphasis on dynamical properties.

The most striking feature in the Venusian atmosphere is a cloud layer consisting of small sulfuric acid (H_2SO_4) particles with a bimodal distribution of 0.5 to 2 - 3 μm. Enclosed by a optically thin haze this cloud layer around 45 - 75 km altitude conceals the surface of Venus for visible wavelengths affecting ground-based observations as well as satellite

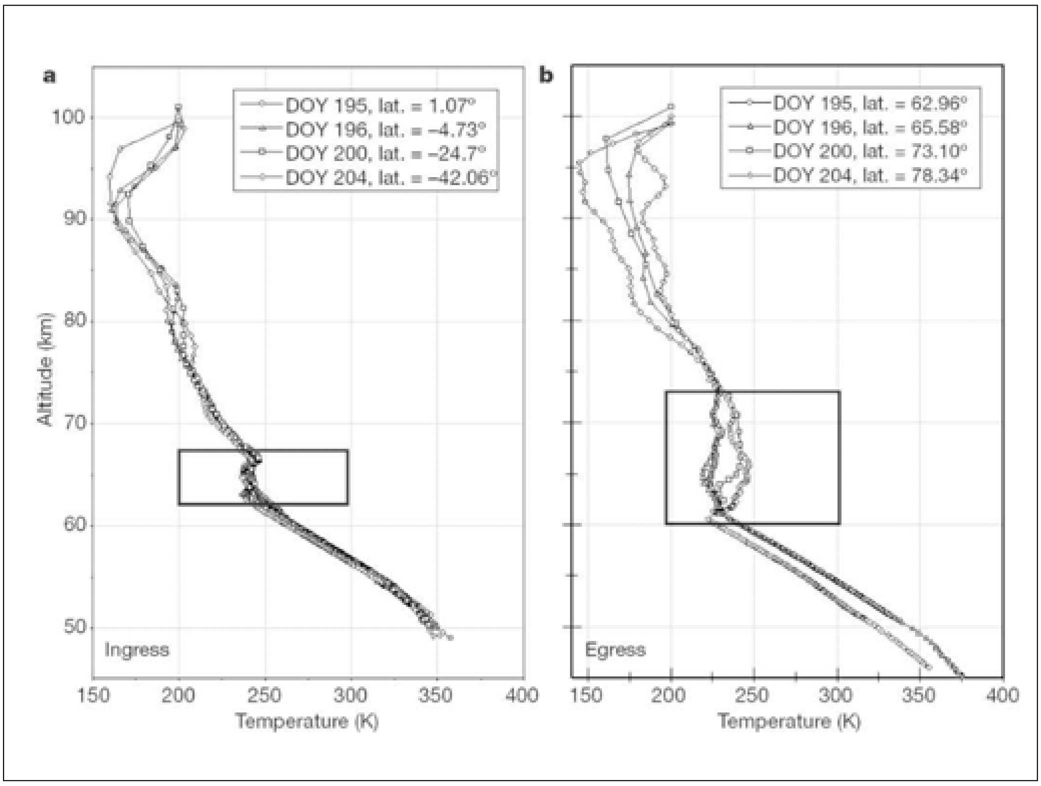

Figure 2.3: *Venus temperature height profiles measured by VeRa (Venus Express Radio Science Experiment) in 2006. The temperature profiles are from southern mid-latitudes (a) and northern high polar latitudes (b) published by Pätzold et al. [39].*

observations from orbit.

The main constituent in the atmosphere is CO_2, along with a small relative amount of nitrogen and other trace gases. The mixing ratio of nitrogen is small compared to CO_2, but the total nitrogen mass is approx. four times higher than on Earth. Geological formations indicate the former presence of water but Venus has lost most of its atmospheric and surface water to space. Today the atmosphere contains water in residual quantities of about 30 ppm. The lack of significant amount of liquid water in the planets atmosphere over geological times has prevented the CO_2 to be transformed into carbonates as it was the case on Earth.

The thermal structure of the troposphere is constrained by the greenhouse effect. About 10% of the solar radiation penetrates the clouds but warms the lower atmosphere and the surface to a temperature of 730 K forming a deep convective region (up to 60 km altitude). This layer is much lager than on Earth due to higher density and optical thickness. The temperature decreases with a constant adiabatic lapse rate beyond the troposphere. The lower mesosphere (60-70 km) is almost isothermal and the adiabatic lapse rate becomes constant again in the higher mesosphere due to the fact that the atmosphere becomes optically thinner [40, 39]. The thermal balance is now determined by upwelling infrared radiation and by emission to upper layers and cooling into space. Only at higher altitudes (~110 km) absorption of solar radiation by water vapor and CO_2 becomes relevant forming a local temperature maximum. The same process occurs caused by ozone on Earth but is much stronger on Venus.

Above 120 km altitude short wavelength solar radiation produces high temperatures during day while low temperatures are found during night caused by efficient radiative cooling by CO_2. Differential solar heating induces pressure gradients triggering the dynamics in this region of the atmosphere.

Ground-based, space-based observations as well as GCM modeling has revealed the dynamics in the middle and lower atmosphere possibly to be constrained by the following patterns (pictured in Fig. 2.4):

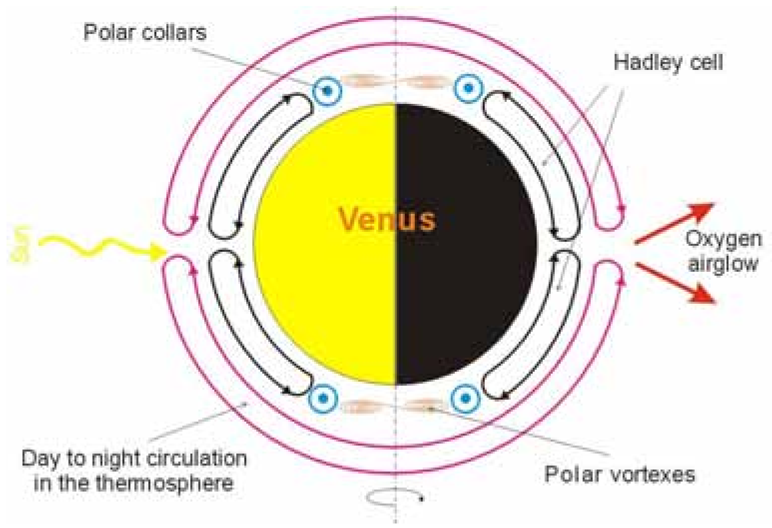

Figure 2.4: *Model of Venusian circulation. In the middle and lower atmosphere convectively driven Hadley cells driven by the concentration of solar heating near the equator are dominant. The return branch lies below the cloud level. In the northern and southern polar regions a "dipole" featured vortex is present. Surrounded by a cold collar circulation at around 70°latitude. Above ~100 km altitude the SS-AS pattern dominates the circulation [41].*

- Venus has a convective and wave-dominated meteorology in the lower latitudes driven by the concentration of solar heating near the equator. Hot air rises and flows toward the North and South Pole due to lower pressure. The air cools down descends and returns back to the equator. This overturning circulation system is called Hadley Cell Circulation and can be found in various versions on all three terrestrial planets (see also chapter 2.2 and 2.3). A slow rotation planet like Venus would have only one main Hadley cell per hemisphere.

- A smoother, banded flow can be found at middle to high latitudes [42]. Around 30 ° from the poles there is a broad cold collar, a region in which the temperature of the clouds is lower than that of the surrounding area [43] mainly observed in the northern hemisphere.
- In the northern and southern polar regions Venus has a dipole shaped vortex with a double-eyed structure rotating within ∼2.6 Earth days (swirling S). It has been first noted in 1974 by observations of Mariner 10 and recently VIRTIS (Visible and Infrared Thermal Imaging Spectrometer) on board VEX has taken pictures of this feature suggesting a long-term stability (see Fig. 2.4 and Fig. 2.5).

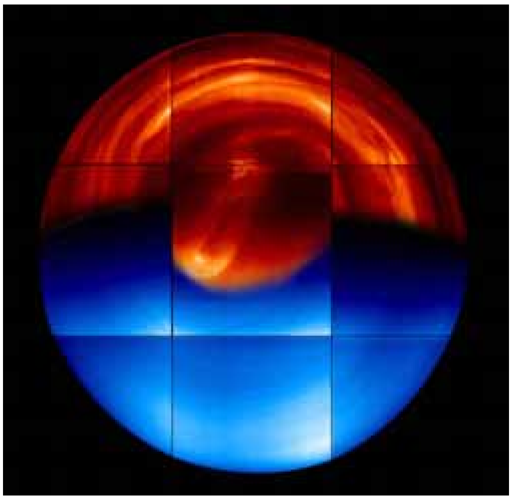

Figure 2.5: *Image of the southern hemisphere of Venus taken by VIRTIS (Visible and Infrared Thermal Imaging Spectrometer) on board VEX. Nightside observations in red show the polar vortex. Dayside observations are in blue. Image: ESA/VIRTIS-VenusX IASF-INAF, Observatoire de Paris (R.Hueso, Univ. Bilbao).*

Venus' upper atmosphere (≥70 km) can be divided into three different vertical dynamical zones [44, 45, 46, 47].

- The lower layer exhibits stable dominant retrograde zonal superrotation (parallel to Venus' solid body rotation) seen from the cloud deck up to about 90 km altitude. The atmosphere at that altitude rotates up to 60 times faster than the solid planet.

- At higher altitudes, as the zonal flow velocity decreases, a strong subsolar to antisolar flow (SS-AS flow) develops. This region at an altitude of 100 – 120 km marks the transition zone from the superrotation region to SS-AS flow dominated region.

- The SS-AS flow is generated by heat input from the Sun and becomes solely dominant in the third layer at about 120 km. Assuming a simple model the SS-AS flow velocity increases linearly with angular separation from the subsolar point [45], as

$$v_{SZA} = v_{max} \cdot \left\{ 1 - \frac{|90 - SZA|}{90} \right\} \tag{2.1}$$

  In this description the outflow velocity reaches its maximum value v_{max} at the terminator, where the solar zenith angle (SZA) equals $90°$. Thus assuming this model, the SS-AS flow velocity at terminator can be determined from velocity measurements elsewhere on the disc.

Though Venus is more Earth-like than formerly believed some key mechanisms of the circulation on Venus are still not fully understood and remain part of an ongoing discussion. The superrotation, especially at the equator is one of the main problems of numerical models. In addition to the slow rotation rate of the planet the vertical stability of the atmosphere seems to play a significant role when simulating an atmospheric rotation faster than the solid body. Contrary to Mars and Earth, where convection and turbulent mixing transfers momentum downward to the surface where it is transferred to the solid body by surface drag, on Venus momentum results in a superrotation of the atmosphere. To compute this superrotation the vertical adiabatic lapse rate profile in Venus' atmosphere has to be taken into account.

Models are currently not reliable above ~90 km altitude. Especially for high altitude regions of the atmosphere, observational constraints to the models are needed to diagnose their ability to reproduce Venus' global circulation.

Spectroscopy is a well-established method to collect information about distant objects. Ground-based observations of fully-resolved molecular transition lines allow the retrieval of physical parameters such as pressure, temperature, molecular abundance, and dynamical properties of the atmosphere [48]. Earth-based measurements of winds above the cloud layer on Venus have been performed by high-resolution mid-infrared spectroscopy of Doppler shifted spectral features [45, 49], as well as by observations of carbon monoxide (CO) at millimeter wavelengths by Shah et al. [50], Buhl et al. [51] and Lellouch et al. [52] and also by visible observations of reflected solar Frauenhofer lines [53]. Visible observations primarily probe near the cloud tops around 70 km altitude, while mm-wave measurements probe the mesosphere/lower thermosphere at $\sim$95-120 km altitude depending on the observed isotope of CO. Mid-IR spectral features probe similar and possibly higher altitudes and can provide higher spatial resolution compared to mm observations, which is important to study dynamical variations over the entire planet. In addition, an unmatched precision of wind determination, down to 2 - 3 m/s, can be achieved using Lamb-Dip stabilized IR heterodyne systems [45, 49]. Previously published results of the different observing methods are summarized in Tab. 2.1.

Using heterodyne spectroscopy at $\sim 10\,\mu$m wavelength wind velocities on Venus can be measured using transition lines of CO_2, the dominant atmospheric constituent. These lines are detected in emission resulting from non-local thermodynamic equilibrium (non-LTE) excitation in the mesosphere (90-120 km altitude). Solar pumped non-LTE emission from Venus was first detected by Betz et al. [3] and later studied by Deming and Mumma [54] using IR heterodyne spectroscopy and modeled by Johnson et al. [55], Deming and Mumma [54] and Roldan et al. [56]. It can be seen in the Martian atmosphere as well [55, 57, 58, 12, 59]. Wind measurements on Mars are also presented within this work (see chapter 2.2).

Table 2.1: *Overview of previous ground-based wind measurements on Venus probing different altitudes from 67 km to 110 km. In addition results from Pioneer Venus (PV) radio occultation data [60] suggesting mid latitude jets with a maximum at 70 km and model results by Bougher et al. [46] are listed*

alt.[km]	$v_{zonal}^{equatorial}$[m/s]	$v_{zonal}^{highlat.}$[m/s]	v_{max}[m/s]	$year_{data}$	obs. method	citation
110	–	–	112	model	model	Bougher et al. [46]
	25±15	–	120±30	1985-1987	IR/CO_2	Goldstein et al. [45]
	130±15[1]	–	95±15[1]	1991	mm/CO	Lellouch et al. [52]
	39.6±2.6	–	118.5±1.5	1990	IR/CO_2	Schmülling et al. [49]
	34.7±1.1	–	129.2±1.2	1991	IR/CO_2	Schmülling et al. [49]
105	90±12	–	90±12	1991	mm/CO	Lellouch et al. [52]
100	–	–	32	model	model	Bougher et al. [46]
99	–	132±10[2]	40[3]	1988	mm/CO	Shah et al. [50]
	60±15[1]	–	65±15[1]	1991	mm/CO	Lellouch et al. [52]
95	40±15	–	40±15	1991	mm/CO	Lellouch et al. [52]
74	83±27[4]	–	–	2001 and 2002	visible/CO_2	Widemann et al. [53]
70	140-150	–	–	1978-1981	radio occ. (PV)	Newman et al. [60]
67	–	–	67±21	2001 and 2002	visible/solar	Widemann et al. [53]

[1]Interpolation from measurements of equatorial velocities at 95 and 105 km
[2]mean value; data from 70 ° S to 61 ° N
[3]suggested upper limit
[4]mean equatorial velocity

Table 2.2: *Overview of ground-based wind measurements on Venus within the coordinated ground-based campaign to support Venus Express probing different altitudes from 66 km to 110 km. Given are published maximum and minimum wind velocities within the diverse observing runs of equatorial zonal wind velocities* ($_{zonal}^{equatorial}$)*, zonal wind velocities from higher/lower latitudes* ($v_{zonal}^{lat.}$) *and cross terminator velocities* v_{max}.

alt. [km]	pres. [mbar]	$v_{zonal}^{equatorial}$ [m/s]	$v_{zonal}^{lat.}$ [m/s]	v_{max} [m/s]	$year_{data}$	obs. method	citation
110		–	68 - 280[1]	–	06/2007	mm/CO	Rengel et al. [61]
110		–	205 - 355[2]	–	06/2007	mm/CO	Rengel et al. [61]
		3±7	≤32±4	52±18	2007	IR/CO_2	this work
		-8±6	≤12±18	80±29	2007	IR/CO_2	this work
				123±24	2007	IR/CO_2	this work
103	0.01	–	195±70 - 235±70[4]	–	06/2007	mm/CO	Clancy et al. [62]
102	0.01	131±13 - 147±3[2]	–	290±44 - 322±25[2]	06/2007	mm/CO	Lellouch et al. [63]
		46±19 - 63±10[1]	–	114±41 - 151±19[1]	06/2007	mm/CO	Lellouch et al. [63]
		-30±53 - 120±36[2]	–	55±53 - 120±36[2]	08/2007	mm/CO	Lellouch et al. [63]
		40±30 - 120±90[3]	–	40±45 - 110±25[3]	08/2006	mm/CO	Lellouch et al. [63]
93	0.1	53±8 - 59±6[3]	–	126±20 - 130±24[3]	06/2007	mm/CO	Lellouch et al. [63]
	0.1	40±30 - 50±13	–	30±11 - 60±30	08/2007	mm/CO	Lellouch et al. [63]
68		92.1±14.1 - 159.9±39.0[5]	–	–	06/2007	visible/solar	Widemann et al. [64]
		104±10[5]	–	–	08/2007	visible/solar	Widemann et al. [64]
67		151±16	–	–	07/2007	visible/solar	Gaulme et al. [65]
66		66±5 - 91±6	–	–	01/2003	visible/solar	Gabsi et al. [66]

[1] dayside measurements
[2] nightside measurements
[3] night and day measurements included
[4] data from 30 ° S to 30 ° N; night and dayside measurements included
[5] mean value

The altitude of the wind measurements is determined by the location of the CO_2 non-LTE emission. In LTE collision is the dominant process that determines the population of the molecules energy levels. Different processes can force a breakdown of the LTE situation into non-LTE. A strong solar radiation field is the prime process for the population of the excited level causing emission at the 10.4 μm band [67, 54, 68]. Near infrared absorption of solar insolation is followed by collisional transfer populating the (00^01) level of CO_2 causing inversion to the (10^00) and (02^00) level. From there radiative decay at 10 μm is possible (see Fig. 2.6).

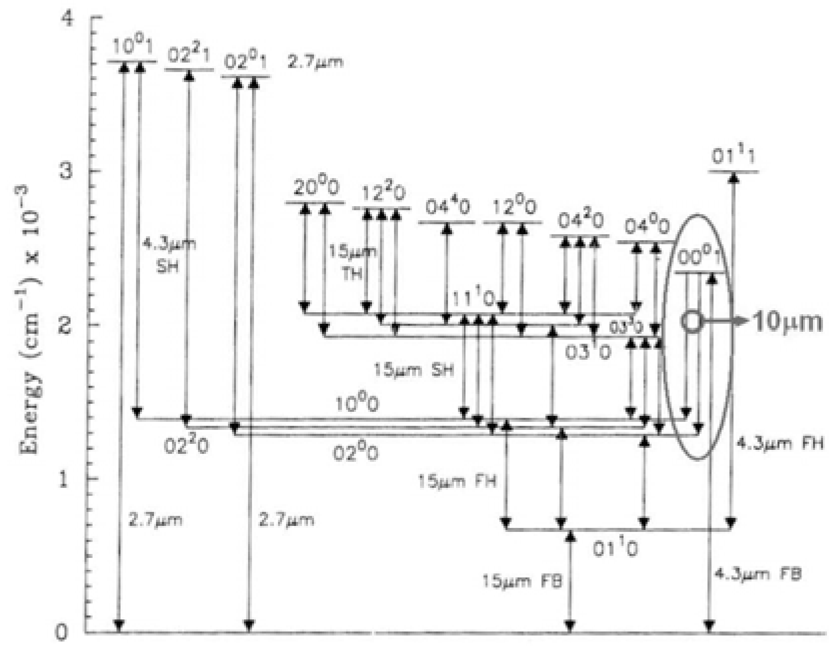

Figure 2.6: *Overview of the vibrational levels and transitions of CO_2 relevant for the 10μm non-LTE emission in planetary atmospheres [67, 54].*

A radiation dominated environment will be generally in non-LTE due to the non-local nature of radiation. As a consequence a given state in a planetary atmosphere is expected to be more likely in non-LTE at lower pressure (means higher up in the atmosphere) and is therefore directly connected to the pressure levels in the planetary atmosphere. Unfortunately it is not yet possible to retrieve altitude information directly from the measured line profiles presented in this work. Therefore it is necessary to refer to other measurements and model predictions.

Deming and Mumma [54] determined the peak of the emission to occur around 109 km. More recently Roldan et al. [56] estimated a maximum of non-LTE emission at $\sim$ 120 km. The VIRTIS instrument on Venus Express observed a peak altitude of 115 km for the 4.3 μm band of CO_2 varying with solar zenith angle (SZA) over a range of $\sim$ 10 km [69]. The altitude for the 4.3 μm band is not necessarily the same as for the 10.4 μm because different non-LTE processes are involved. Deviations from model predictions to a lower altitude peak were found at least in some cases and could be due to variations in the temperature / pressure profile. For the time being an altitude range for wind velocities of 100-120 km is assumed. A more precise information about altitude of the CO_2 non-LTE emission at 10 μm would enhance the quality of the measured data strongly. In coordination with modelers this will be the subject of a following thesis within our group in Cologne.

The line-of-sight component of the wind velocity near the limb leads to a frequency shift of the measured non-LTE emission line that is measurable at spectroscopic resolving power of $\frac{\nu}{\Delta\nu} > 10^6$. Given the observational geometry, the frequency measurement can be inverted to retrieve independent wind velocities at each observed position. One essential advantage of heterodyne spectroscopy is that no additional assumptions about the state of the atmosphere or deconvolution of a line profiles are necessary to retrieve wind velocities, hence this method is independent to models and additional temperature/pressure information.

Within this work we tried to coordinate our observing schedule with that of other groups using complementary techniques mainly through participating in a coordinated ground-based campaign to support Venus Express in May/June 2007. We also took into account specific questions relevant to model developers. All results of atmospheric wind measurements presented in this work (see 4.1) were obtained by heterodyne infrared spectroscopy using the Cologne Tuneable Infrared Heterodyne Spectrometer THIS. A detailed description of the instrument can be found in chapter 3.

2.2 Dynamics in the Martian Atmosphere

In the year 1784 William Herschel correctly concluded the low density of the Martian atmosphere from the fact that two faint stars passing close by Mars showed no effect on their brightness. At the beginning of the 19^{th} century Honore Flaugergues reported about another atmospherical feature on Mars. His observations of "yellow clouds" were the first report of dust storms on the "Red Planet".

Besides observations from Earth, spacecrafts were launched to observe Mars. The first successful fly-by of Mariner 4 in 1965 (USA) provided high spatial resolution images of the Martian surface and the first in situ retrieval of atmospheric surface pressure of 4.1-6 hPa [70] was a milestone in space exploration. Together with ground-based observations and airborne missions, at various time scales information about the surface and atmosphere increased essentially and led to first attempts to describe the general circulation and climate on Mars.

Mariner 4 was followed by Mariner 6 and 7 in 1969 and the first successful orbiter Mariner 9 in 1971. During these missions the first observation of atmospheric ozone was made [71, 72] and the Mariner 9 instrument IRIS provided extensive temperature measurements in the lower atmosphere between 0 - 50 km [73]. The Russians launched their first successful orbiter Mars 2 in 1971.

Within the next years several attempts of landing an object on Mars' surface failed. Only data during decent was returned until 1976 when the US Viking program was started. The Viking landers gave new insights to the atmosphere by first direct surface wind measurements [74] in the lower atmosphere.

In 1996 the Mars Global Surveyor was successfully inserted into Mars orbit followed by the Mars Pathfinder rovers in 1997. More recently (2001) the Mars Odyssey orbiter was launched. The Mars Express orbiter was the first European Mars mission. It is still operational whereas contact to the lander Beagle 2 was lost during decent. The American rovers Spirit and Opportunity (landing in 2004) are still operational as well as the Mars Reconnaissance Orbiter (arrival at Mars in 2005). The Phoenix Spacecraft Lander has been launched in 2007 and arrived on Mars in May 2008 currently providing astonishing data to scientists and the general public.

Mars is still the planet of our solar system receiving most attention. Showing several similarities to our home planet Earth, Mars might have provided or even still provides habitable conditions conducive to the development of life. Though being an interesting question, search for life on Mars should not be the sole motivation for exploration. To understand the global behavior of the Martian atmosphere full account of the complexity and interdependency of many different kinds of parameters and processes are necessary. In order to adopt GCMs from Earth to Mars and to draw conclusions back to Earth it is important to distinguish which features of the climate system are unique to Mars and which are universal. The transformation of terrestrial models to Mars was eased due to the strong similarities:

- The obliquity of both planets is almost the same (23.44° for Earth and 25.19° for Mars) causing similar annual seasonal cycles. Especially the middle atmosphere is believed to be similar to Earth. The inclination seeks the transport of heat from the warm tropics to the cold poles causing a meridional flow and annual variations in mid- and high latitudes.
- The sidereal period of both planets is nearly identical. A Martian day is called "sol" and is 88 775.245 seconds (24 h 39.59 min) long. This fast and similar rotation results in a comparable Coriolis force.
- On both planets most of the sunlight is penetrating through the atmosphere and infrared radiation from the planets surface heats the atmosphere.

But there are also differences strongly impacting the behavior of the atmospheres:

- The distance from Mars to the Sun is approximately twice than the Earth Sun distance. Therefore solar radiation is less intense on Mars.
- In addition, the orbit of Mars is significantly more elliptical than the Earth orbit causing $\sim$45% greater solar flux at perihelion than at aphelion. This elliptical orbit leads to significant asymmetries between northern and southern hemisphere seasons accentuated by the occurrence of perihelion and aphelion close to the solstices. Presently, the northern summer / southern winter is shorter but more intense than the southern summer / northern winter. Due to varying temperature atmospheric pressure changes by $\sim$20% within a year forcing sublimation and refreezing of CO_2 and water at the polar caps. Due to the eccentricity of the orbit, the length of the Martian months vary from 46 to 67 sols over a Martian year. The Martian year with 668.6 sols is approximately twice as long as a year on Earth. To avoid confusions an overview of nomenclature and definitions of Martian days, months and seasons is given in Tab. 2.3 and Fig. 2.7.
- The surface pressure on Mars is around 0.5-1% of that on the Earth, a pressure level below the triple point of water. Therefore even if temperatures would rise higher than the melting point ($\sim$273 K) water would not melt into liquid water but sublime.
- The Martian surface is a dry desert and the low thermal capacity of the surface causes strong reactions to changes of insolation. Due to

Table 2.3: *Overview of the Martian annual cycle. Given are the Martian solar longitude L_S and duration of the months and the Martian seasons. See also Fig. 2.7 [75].*

month	Ls range [°]	sol range	duration [sol]	season
1	0-30	0.0-61.2	61.2	Northern Hemisphere Spring Equinox Ls=0
2	30-60	61.2-126.6	65.4	
3	60-90	126.6-193.3	66.7	largest Sun-Mars distance Ls=71 (Aphelion)
4	90-120	193.3-257.8	64.5	Northern Hemisphere Summer Solstice Ls=90
5	120-150	257.8-317.5	59.7	
6	150-180	317.5-371.9	54.4	
7	180-210	371.9-421.6	49.7	Northern Hemisphere Autumn Equinox Ls=180 Dust Storm Season begins
8	210-240	421.6-468.5	46.9	Dust Storm Season
9	240-270	468.5-514.6	46.1	smallest Sun-Mars distance Ls=251 (Perihelion) Dust Storm Season
10	270-300	514.6-562.0	47.4	Northern Hemisphere Winter Solstice Ls=270 Dust Storm Season
11	300-330	562.0-612.9	50.9	Dust Storm Season
12	330-360	612.9-668.6	55.7	Dust Strom Season ends

the lack of lakes and oceans the day-to-night temperature variation (ΔT=60 K) is much higher than on Earth (ΔT=30 K) causing strong thermal tides whereas this effect on Earth is diluted by the influence of the surface water. Also seasonal temperature differences are much larger than on Earth.

- The planets atmospherical composition is completely different. The Martian atmosphere (being similar to Venus) consists mainly of CO_2 and small amounts of nitrogen and argon and only a very small amount of water vapor can be found.

- Water clouds are less abundant on Mars than on Earth existing 10 km above the surface or higher.

- There is only a modest greenhouse effect on Mars with 5 K warmer environment compared to a planet without an atmosphere. For

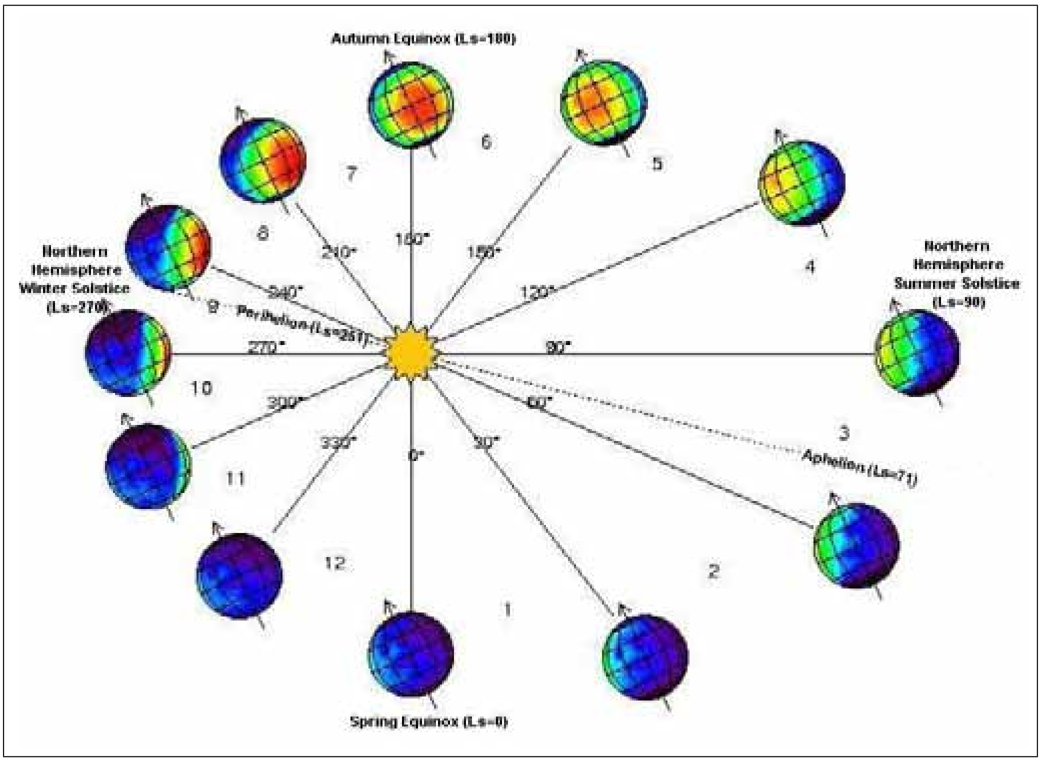

Figure 2.7: *Overview of the Martian annual cycle [75]. The Martian year is 668.6 sols long. One sol, the duration of the rotation of Mars, is 24 h 39.59 min. Because of the eccentricity of Mars' orbit months are not equally long. They vary from 46 to 67 sols. Aphelion, the largest Sun-Mars distance occurs at Ls=71 close to the northern hemisphere solstice. Perihelion, the smallest Sun-Mars distance occurs at Ls=251 close to northern hemisphere winter solstice. See also Tab.2.3.*

> Earth the greenhouse warming changes the temperature from 255 K (-18 C) to an average temperature of 287 K (14 C).

Like on the other terrestrial planets the air around the equator on Mars receives more solar energy than at other latitudes and overturning Hadley cells develop. Since Mars is a fast rotating planet the Hadley cell breaks up into several smaller units. Due to the obliquity the Hadley cell circulation varies strongly with season. During equinox primarily a dual Hadley cell system emerges originating from rising air at the equator induced by solar heating, symmetric in the North and South. This causes westerly zonal circulation due to Coriolis force on the meridional flow of the Hadley cell similar to the equatorial region on Earth (see chapter 2.3). At solstice basically only one large Hadley cell from high latitudes in the summer hemisphere to high latitudes in the winter hemisphere evolves. Coriolis torques exerted on the meridional flow generate zonal easterlies (retrograde) circulation in the summer hemisphere and westerlies (prograde) circulation in the winter hemisphere [76].

A detailed description of the Martian atmosphere needs to be highly sophisticated and complex. GCMs are dependent on observational constraints for parameterization and also for validation of models. To date the ability to describe circulation at high altitudes is limited and the lack of observational constraints in these atmospheric regions is a drawback for a global understanding of the Martian circulation. This was the motivation to apply the Cologne heterodyne spectrometer THIS to planetary wind measurements. Like in the case of Venus ground-based measurements can provide complementary data not available from space missions probing other atmospheric regions. In addition, only ground-based observations can provide the opportunity of long-term studies.

Ground-based direct wind measurements on Mars have mainly been carried out by millimeter observations of CO at much lower spatial resolution. Even interferometric observations allow only 4x4 independent points on Mars [77]. Strong retrograde winds between 100 and 200 m/s were found at the western equator [77] and in the southern hemisphere [78, 79] at different Martian seasons (see Tab. 4.14). These observations probe an altitude region between 35–80 km.

For our IR observations of CO_2 the altitude of measured winds is determined by the location of the CO_2 non-LTE emission and therefore directly connected to a certain pressure level (see chapter 2.1). With the exceptional high spectral resolution of the instrument THIS this molecular lines with a width of $\sim$25 MHz can be resolved and an observed frequency shift can be directly converted into a line-of-sight wind velocity (see also Eq. 2.1). Like on Venus altitude of the emission-forming region cannot be determined from the observed lines directly so far. In the case of Mars, observations of non-LTE emission line at 10 μm with the Thermal Emission Spectrometer on Mars Global Surveyor by Maguire et al. [58] are available. Non-LTE emission from limb observations was found to peek at $\sim$70 km altitude, with the emission-forming region ranging from 50 and 90 km altitude. This is consistent with model predictions by Lopez-Puertas and Taylor [67]. An overview of ground-based measurements, important parameters like spatial resolution etc. and results is given in Tab. 2.4.

Table 2.4: Overview of previous Martian Doppler wind observations. The table contains the addressed altitude, the field-of-view (FOV), the angular diameter of Mars, Martian season, the year of observation and the corresponding publications.

alt. [km]	transition	FOV arcsec	Mars arcsec	latitude [°]	season [Ls]	v_{zonal} [m/s]	$year_{data}$	citation
35-80	CO 2-3	13″	25″	20°S	251 – 254	-120 – -200	2003,2005	Clancy et al. [78]
40-70	CO 2-1	12″	23.8″	20°S	279	-160 ± 80	1988	Lellouch et al. [79]
45-69	CO 1-0, 2-1	-	9″-23″	0	140, 196, 262, 317	-100 ± 20	1999,2001,2003	Moreno et al. [77]
60-80	CO_2 2-1	2″	1″	20°N	308	-74 ± 22	2003	Sonnabend et al. [80]

2.3 Dynamics in the Earth Atmosphere

Several similarities and differences to Mars and Venus were already mentioned in the chapter above. To complete the comparison of the general circulation in the terrestrial planets' atmospheres the main characteristics of the Earth Global Circulation will be briefly presented in this section. No measurements in the Earth' atmosphere have been accomplished using THIS within this work, however future observations might be feasible and are currently under consideration. On Earth there

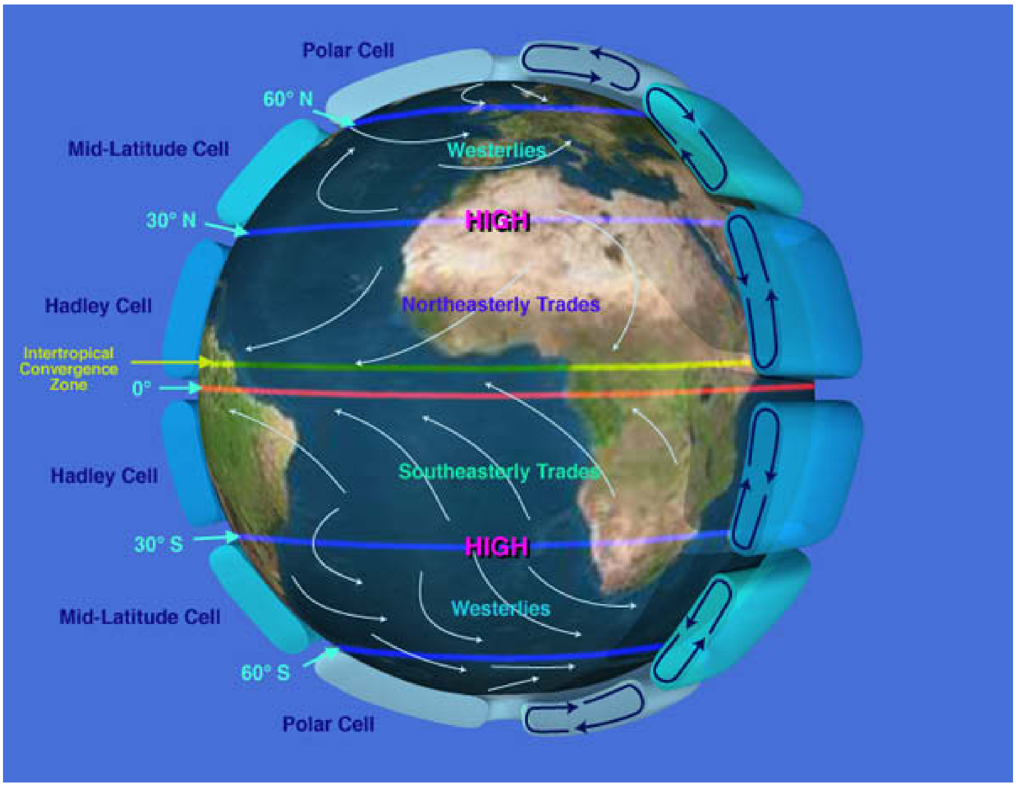

Figure 2.8: *Scheme of the global Circulation on Earth dominated by three Hadley cells on each hemisphere, the easterly trade winds at low latitudes and westerly winds at high latitude [81].*

are three Hadley cells on each hemisphere forming six belts surrounding our planet:

1. The Equatorial Hadley Cell:
   The air at the equator is heated by solar radiation. It rises, cools down and precipitates. The now dryer and cooler air moves towards the poles. At the so called "horse latitudes" (around 30°

North and South) the air meets downwelling air from the poles. It compresses, warms and absorbs moisture from the surface thus forming the large deserts around the ”horse latitudes”. Part of the air returns to the equator and forms the first Hadley cell.

2. The Mid-Latitude Hadley Cell:
   The other part moves towards the pole where it meets very cold air from the pole and is therefor forced to ascent. It cools and looses moisture. The mid-latitude cell of the circulation behaves in a thermodynamically indirect way - the air rises at the cold side of the cell and descents at the warm end.

3. The Polar Hadley Cell:
   Lastly, the polar cell is formed by very cold air coming from the North / South ascending at around 60° North and South were it meets the air from the middle cell. After ascending and precipitating the very dry air returns toward the poles and sinks immediately.

The Earth is like Mars a fast rotating planet and the cells get shifted by the Coriolis force. This results in easterly dominated zonal trade winds in the equatorial and polar Hadley cells and westerly dominated zonal trade winds in the mid-latitude Hadley cells.

Chapter 3

"A theory is something nobody believes, except the person who made it. An experiment is something everybody believes, except the person who made it." (Albert Einstein (1879 – 1955), German-born physicist)

The Tuneable Heterodyne Infrared Spectrometer: THIS

High resolution spectroscopy is a versatile tool to study planetary atmospheres. In the thermal (or mid) infrared wavelength regime the highest possible spectral resolution is provided by applying heterodyne techniques. At a spectral resolution of more than 10^7 observations of fully resolved molecular features are possible allowing retrieval of many physical parameters from single lines. In addition, due to the fact that many of the observed species are abundant also in the Earth atmosphere, high resolution measurements allow to peak through the telluric features to see their Doppler-shifted counterparts with less ambiguity than presented by low resolution data (see 3.1).

The following chapter gives a short introduction to the heterodyne principle and a detailed description of the setup of the Cologne heterodyne receiver THIS.

3.1 Characteristics of a Heterodyne Receiver

Heterodyning, in principle, is the generation of new frequencies by mixing signals in a nonlinear device. For an astronomical receiver this

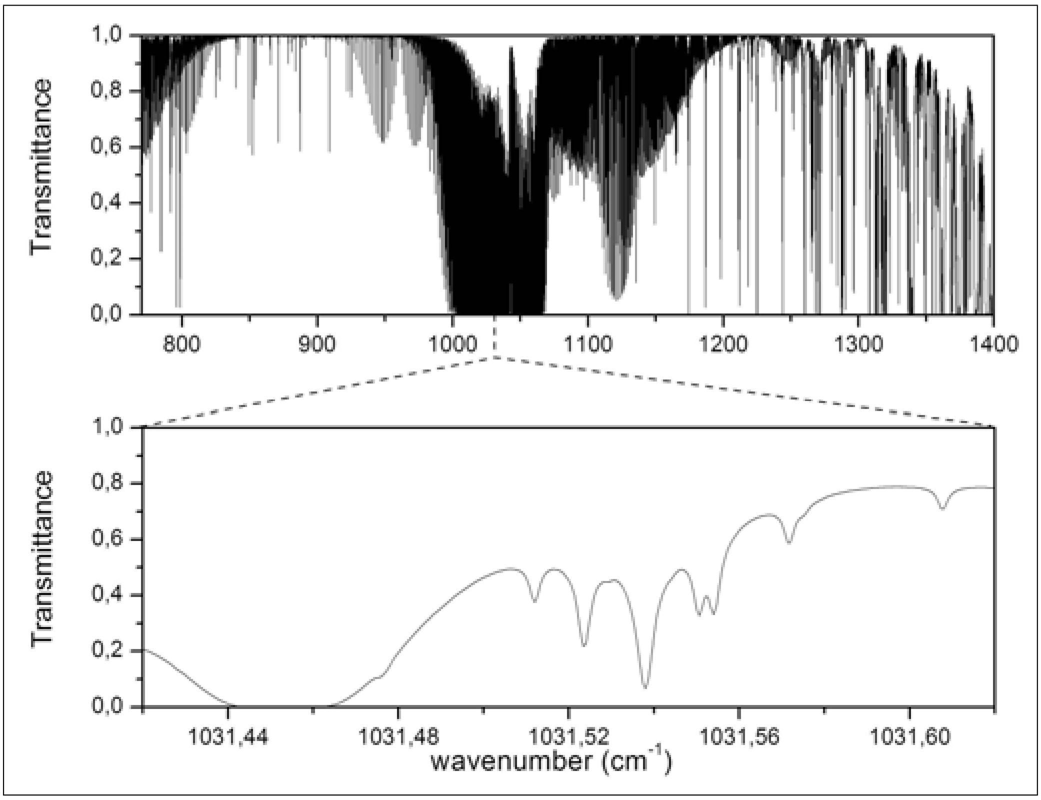

Figure 3.1: *The transmittance of Earth's atmosphere is poor between 7 and 13 μm. The upper panel shows the limited transmittance due to O_3, CO_2 and H_2O molecules. Infrared heterodyne spectroscopy fully resolves individual absorption features (lower panel) allowing to peek through atmospheric windows providing the only ground-based access to features in planetary atmospheres when they are Doppler shifted away from their telluric counterparts towards regions of higher atmospheric transmittance (arrow).*

means mixing of a monochromatic source, the local oscillator (LO), and the signal to be detected from the telescope. The superposition and the interaction of the two signals can be described by summation of their electric fields. Using a mixing device with a square-law characteristic detects the incident power which is proportional to the square of the electric fields. The incident power P_{det} at the mixer causes a total photo current I_{det} of

$$I_{det} = \frac{\eta \cdot e_0 \cdot P_{det}}{h \cdot \nu}$$

where ν is the observed frequency, e_0 the elementary charge, h the Planck constant and η is the quantum efficiency of the detector describing the ratio between the number of incident photons and the number of detected photons. This yields contributions at the original frequencies, the difference of the LO and the sky signal and their sum. The sum and the original frequency components of the signal are too high in frequency and are averaged by the detector thus resulting in a DC photo current. Only the difference frequency, the so called intermediate frequency (IF), induces an oscillation of the charge carriers in the detector. This process finally results in a total photo current I_{det} of:

$$I_{det}(t) = I_{lo} + I_{sig} + 2 \sum \sqrt{I_{lo} \cdot I_{sig}} \cos(\Delta\omega_i \cdot t)$$

where I_{lo} and I_{sig} are the photo currents induced by the LO and by the signal producing the DC component whereas the third term is responsible for the mixed signal with $\Delta\omega_i$ representing the frequency difference between LO and signal radiation. The IF signal contains all the spectral information from the original IR signal. The bandwidth of a typical heterodyne detector is in the range of a few GHz. Due to the symmetry of the cosine the negative and positive frequency difference can not be distinguished. Therefore signal from above (upper sideband) and below (lower sideband) the local oscillator frequency will be detected simultaneously at the same IF frequency. Thus a heterodyne spectrum is always a so called double sideband (DSB) spectrum unless one of the two sidebands gets suppressed by filters. Electronical filters are commonly used in radio frequency heterodyne receivers but optical filters, necessary in the mid infrared, are not feasible. Contributions from the superposition of the different frequencies in a broadband source (self beating) can be neglected due to the fact that the power of the LO is several orders of magnitude higher than the broadband signal power.

A detailed description of the instrument including important specifications is given in the following sections. Further information about the characteristics of a heterodyne receiver can be found in publications by Sonnabend et al. [82] and Schieder [14].

3.2 Setup of the Spectrometer THIS

The transportable IR heterodyne receiver THIS was designed by Sonnabend [83] based on a laboratory experiment setup by Schmülling [84] and Harter [85]. The most important difference to other existing IR heterodyne systems is the use of tunable lasers as local oscillators instead of CO_2 lasers extending the accessibly wavelength range considerably. The mobility of the system was the precondition for initial measurements of telluric molecular features using the Sun, Moon and Mercury as background sources. The results of these measurements were used to verify and improve the instrument performance before first scientific relevant data were gathered observing molecular absorption features in sunspots [86, 21].

The next step in evaluating the performance of the instrument was the detection of fainter sources than the Sun. Molecular transition lines in the atmospheres of other planets were chosen to be the target and test measurements of Martian CO_2 absorption and emission lines were accomplished in 2003 and published by Sonnabend et al. [80]. Based on these results and experiences the spectrometer was improved to be routinely available for scientific observations. The current instrument setup and performance will be presented in detail in the following sections.

The spectrometer basically consists of two parts:

a.) The Optical Receiver,
with all optical components necessary for matching the instrument to different telescopes with different F-ratios (F#) as well as the beam combining optics. Housed in an aluminum frame having dimensions of $\sim 80 \times 60 \times 45\,\mathrm{cm}^3$ and a weight of ~ 80 kg (see Fig. 3.2) it contains also the detector and the LO.

b.) The Electronical Equipment
The main components are the acousto-optical spectrometer (AOS) used as back–end spectrometer and a personal computer used for remote control and data acquisition. Together with additional necessary electronic equipment (e.g. power supplies for LO, alignment lasers and the detector; IF-box; temperature control and heater for the LO; supply and control unit for the scanner) they are mounted in two 19″ racks (see Fig. 3.3).

Figure 3.2: *The optical receiver displayed here is one of two parts of the transportable instrument THIS*

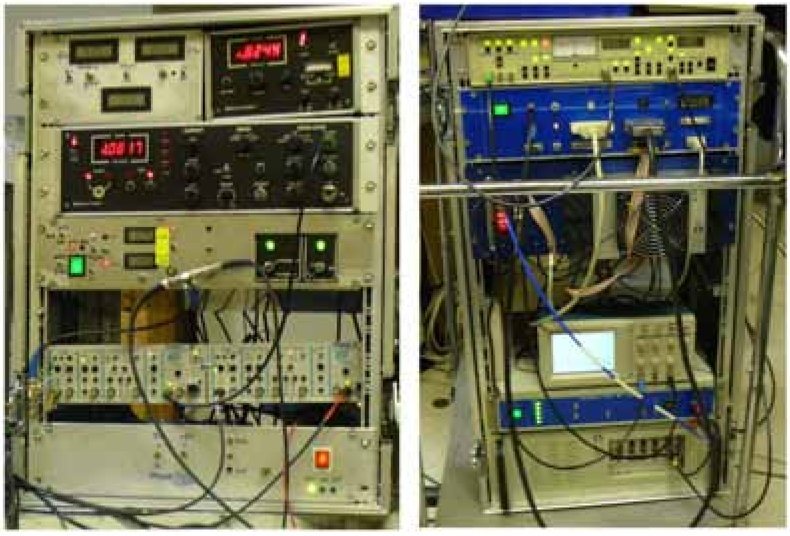

Figure 3.3: *The electronical equipment shown in this figure is the second part of the heterodyne spectrometer THIS.*

The optical receiver and the electronical equipment will be described in detail in the following sections.

3.2.1 Optical Receiver

The most important components of the opical receiver are:

- the **Quantum Cascade Laser (QCL)**, used as LO.
- the **Confocal Diplexer** for efficient superimposing of signal and LO.
- the **Galvano Scanner** providing high speed switching between different loads.
- the **Mercury-Cadmium-Telluride (MCT) Detector** providing IF signal up to 3 GHz.
- the **Beam Matching and Optical Guide System** to match the spectrometer to various telescopes and provide accurate pointing during observations.

A schematic of the setup can be found in Fig. 3.4.

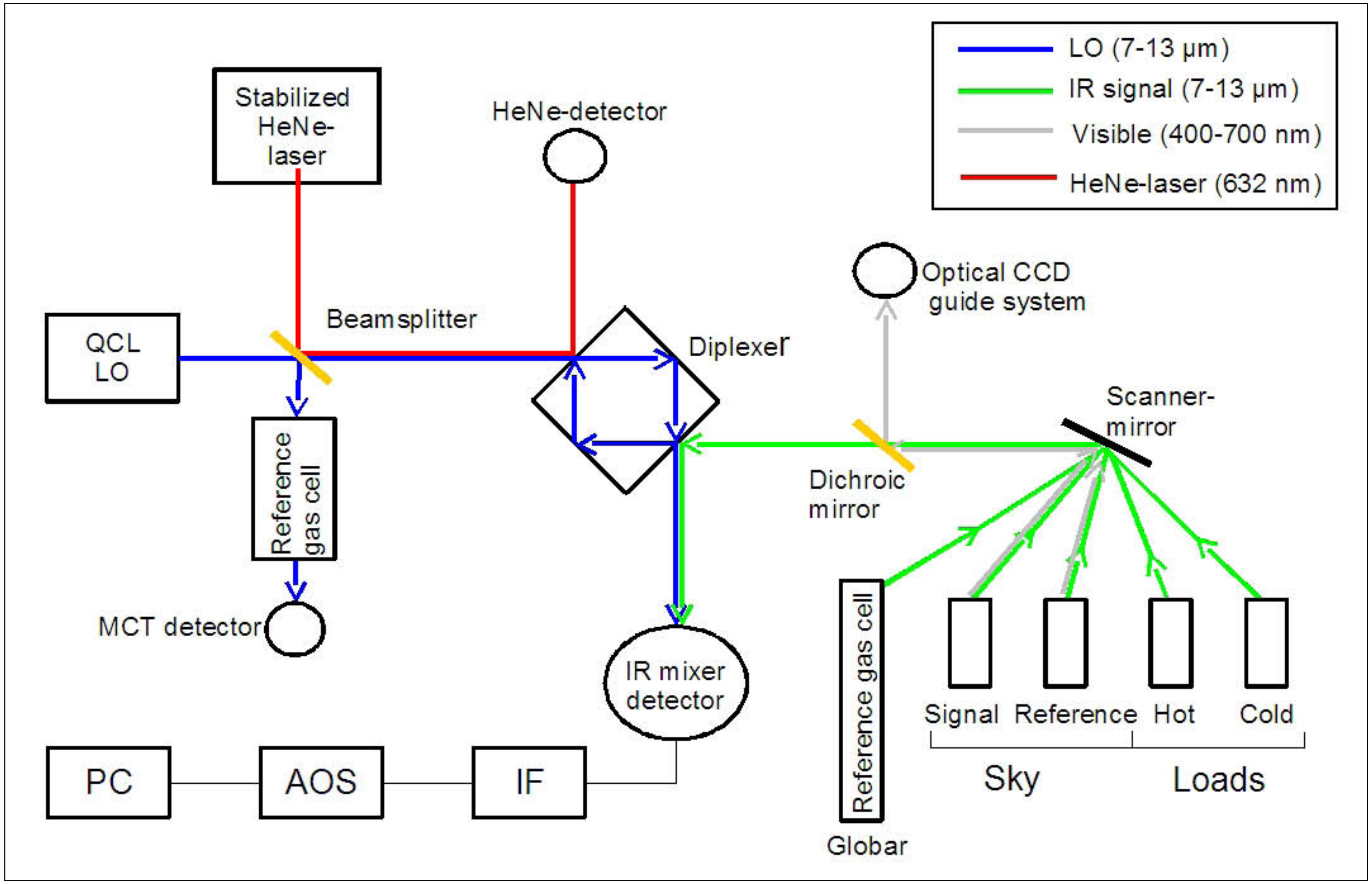

Figure 3.4: *Schema of the spectrometer THIS. The QCL-LO beam passes the diplexer in transmission. By means of a scanning mirror different sources can be selected for observation and calibration. Those signals are reflected at the diplexer. The superimposed beams are then focused on the MCT mixer detector which generates a photo current (i.e. the IF signal) which is analyzed by an AOS and processed by a PC.*

The Local Oscillator

The operating wavelength range of the spectrometer is determined by the tuning range of the local oscillator (LO) and the detector and its bandwidth. For THIS Quantum Cascade Lasers (QCLs) are used as LOs. QCLs are solid state lasers providing high output power due to multiple usage of the electrons in a GaInAs/AlInAs or GaAs/AlGaAs multilayer quantum cascade structure (see Fig. 3.5). The output wavelength is determined by the design of the potential barrier of the multilayer structure and can be engineered to match the desired wavelength. Furthermore the wavelength of a fabricated device can be tuned by the current and temperature changing the refractive index in the device and thus the frequency. This tuneability provides continuous access to different wavelengths, not accessible using gas lasers. In contrast to other solid-state lasers, i.e. lead salt TDLs (tuneable diode lasers) which have been used previously, QCLs provide two orders of magnitude higher optical power thus allowing efficient pumping of the heterodyne mixers [20].

QCLs at mid-IR wavelengths are usually multi-mode lasers. By introducing an additional grating structure onto the device (internally) or in an external cavity lasers can be forced to single mode operation. This is a necessary precondition for their use as a LO in a heterodyne setup. Lasers with an internal grating structure are called "distributed feedback" (DFB) lasers and can be tuned within a range of a few wavenumbers. A detailed description of QCLs and their application as LOs is given in Wirtz [21].

Using a QCL without DFB structure, a so called Fabry-Pérot (FP) QCL, in combination with an external cavity (EC) increases the tuneability by a factor of up to 100. A laboratory setup for a EC-QCL-LO has been accomplished by Maulini et al. [87] and also by Stupar [88] within our group at the University of Cologne. The next step will be the implementation of the EC-QCL-LO to the spectrometer THIS thus greatly expanding the accessible wavelength range [11, 89].

The LO QCL for THIS is mounted in a LN_2 cooled dewar and collimated by an off axis parabola (OAP) mirror. THIS can be operated at wavelengths between 7 μm and 13 μm using different QCLs manufactured by Alpeslasers (CH), Thales (F), Maxion (USA) and the University of Neuchatel (CH). Tab. 3.1 shows the currently available LOs and thus the wavelengths THIS can be operated at.

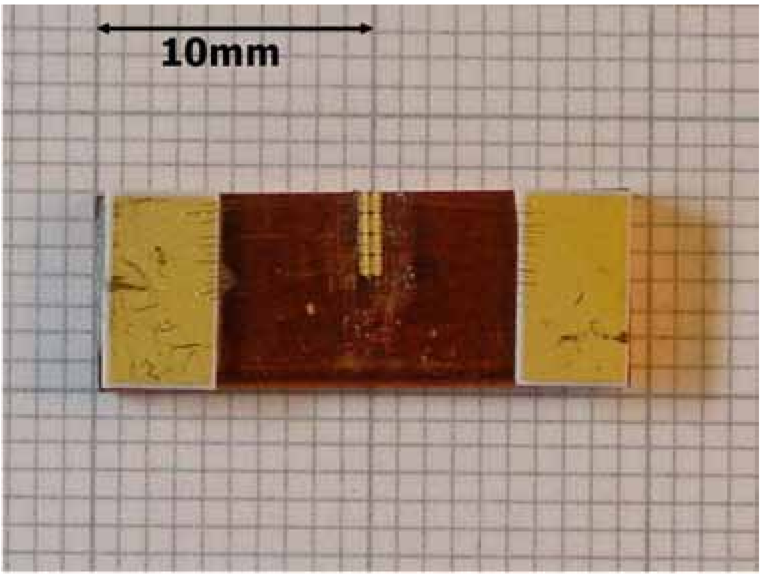

Figure 3.5: *Photograph of a QCL used as LO for the IR heterodyne receiver THIS. The golden bar in the center of the copper mounting is the QCL connected to the bond pads (gold) at the left and right.*

Table 3.1: *Currently available LO QCLs for the spectrometer THIS.*

Laser Wavelength [μm]	Manufacturer	Design
7.75–7.85	Alpeslasers	DFB
8.5–8.8	Thales	FP
8.4–9.6	Uni Neuchatel	Broadband FP
9.55-9.65	Alpeslasers	DFB
10.35–10.45	Alpeslasers	DFB
10.4–10.8	Maxion	FP
10.55–10.65	Maxion	DFB
11.5–11.9	Maxion	FP
12.8–13.2	Maxion	FP
13.15–13.25	Maxion	DFB

The Diplexer

To optimize the superposition of the signal and the laser and to provide a relative frequency standard a confocal Fabry–Pérot ring resonator is used, the so called diplexer. The diplexer consists of two focusing elliptical mirrors and two reflective beam splitters [11]. A picture of the designed diplexer is shown in Fig. 3.6.

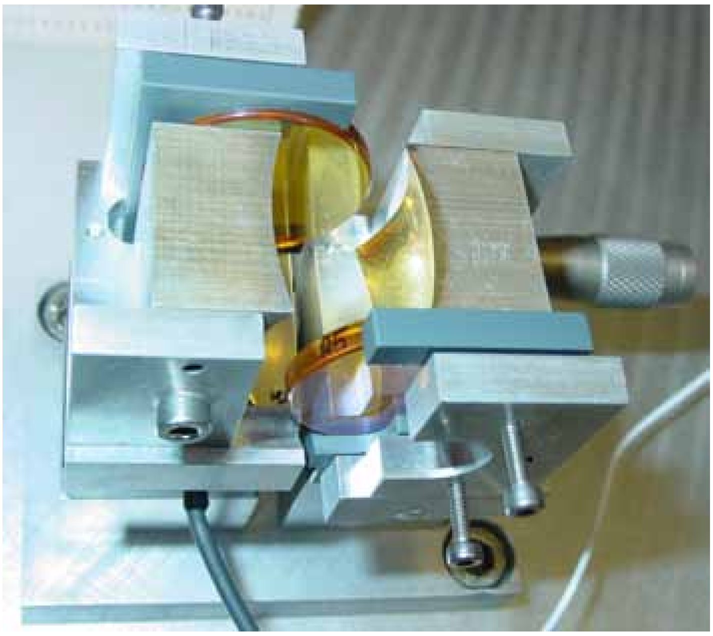

Figure 3.6: *Photo of the diplexer with a free spectral range (FSR) of 5 GHz consisting of two focusing elliptical mirrors with a focal length of 15 mm and two highly reflective ZnSe beam splitters having a reflectivity of ~ 90 %.*

The diplexer serves multiple functions:

a.) **Superposition of signal from sky and LO**
The diplexer allows combination of the signal power with the LO power at an efficiency not possible with a simple beam splitter. The reflection and transmission are determined by the reflection coefficients of the beam splitters and by losses in the device. It follows the Airy function (see Fig. 3.7). The transmission maxima of a confocal resonator in general are separated by $\Delta\nu = \frac{c}{4 \cdot l}$ where l is the length of the resonator. For a well aligned coupling of the LO signal to the confocal resonator however the distance between the transmission maxima increases to $\Delta\nu = \frac{c}{2 \cdot l}$.
Using QCLs with high output power shifted the priority from high

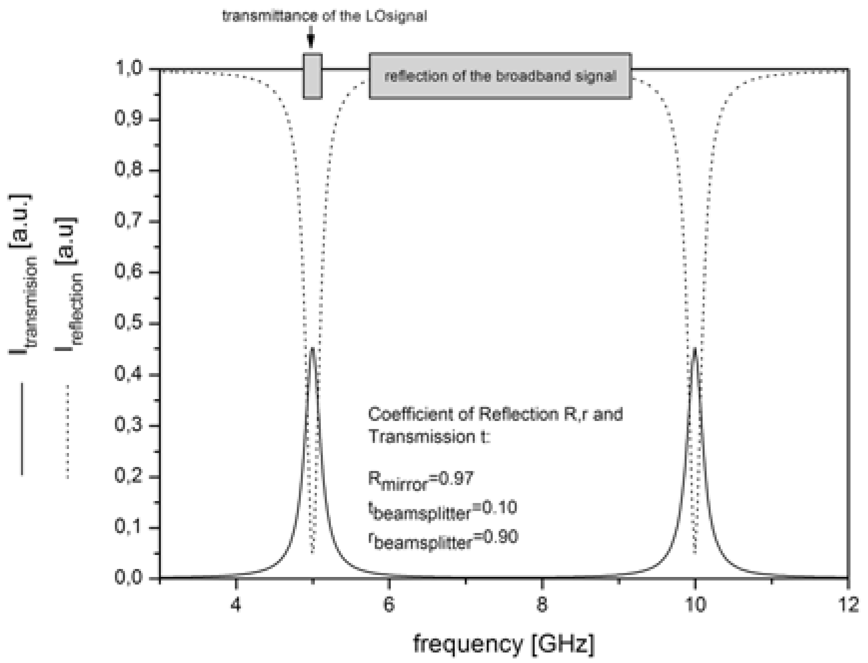

Figure 3.7: *The Airy function describing the transmission (solid) of the LO and reflection (dashed) of the broadband signal through the diplexer. Depending on the reflectivity of the used beam splitters a transmission of* $> 45\,\%$ *(at the frequency of the LO) and a reflection of more than 95 % (within the signal bandwidth) can be achieved over the free spectral range of the Fabry–Pérot.*

transmission of the LO to maximum reflected broadband signal.

The wider bandwidth of recently fabricated detectors implemented in the system and a newly developed broadband AOS [90] required the construction of a new diplexer with an extended free spectral range (FSR) of 5 GHz. Mirrors with a focal length of 15 mm were arranged at a distance between the mirrors of 21.2 mm. A schema of the designed diplexer is given in Fig. 3.8. The used beam splitters, manufactured by the II-IV Ltd are ZnSe windows with a standard coating for 10.6 μm, reflecting $\sim 90\,\%$ within 9–11 μm at one surface, and an anti-reflex coating on the other surface.

Using these beam splitters the diplexer provides a reflected broadband signal of $> 95\,\%$ (fed into the diplexer at port 3 shown in Fig. 3.8) superimposed to the transmitted LO signal of $> 45\,\%$ (fed into the diplexer at port 1). At other wavelength the coating of the beam splitters has to be adapted. Hence the mechanical design of the diplexer had to allow the change of beam splitters coated for different wavelengths during an observation run with minimum effort and time consumption.

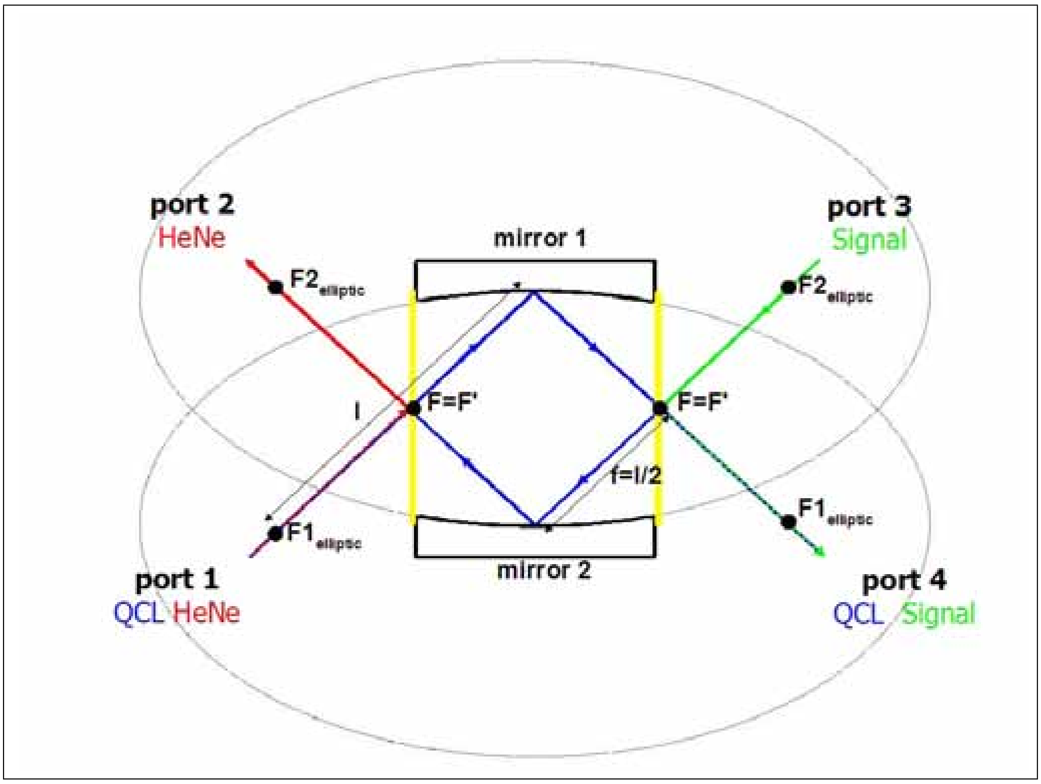

Figure 3.8: *Schematic of the Diplexer responsible for superimposing the broadband signal (green) with the QCL (blue). The HeNe laser (red) is used for stabilization of the QCL. The diplexer consists of two elliptic mirrors and two highly reflective beam splitters. Note that the arrangement is confocal meaning the focal point F of the first elliptic mirror is on the same position as the focal point of the second mirror F'. The focal length f of the mirrors is half the distance l to the focal points ($F1_{ellipse}$ and $F2_{ellipse}$) of the ellipse.*

The superposition of broadband signal and LO signal is the main function of the diplexer but there are further advantages providing a stable performance of the entire system:

b.) **Suppression of side modes and unwanted signal feedback from optical elements**
Possible side modes of the LO are suppressed by the resonator. The inherent side mode suppression of the DFB lasers is essentially enhanced to avoid unwanted emission. In addition, accidental feedback from optical elements in the beam path (e.g. windows), which could lead to standing wave patterns in the IF signal, is suppressed too.

c.) **Frequency Stabilization of the Receiver System**
A stable LO frequency is essential for high spectral resolution observations in general but especially important for the determination of wind velocities through Doppler shifts in the range of a few MHz. The diplexer provides a relative frequency reference and is used for frequency locking of the QCL. The locking process is performed in two steps:

- At first, a stabilized Helium-Neon (HeNe) laser operating at 632 nm (frequency stability $\frac{\nu}{\Delta\nu} \approx 10^8$ within 8 hours) is fed into the diplexer via port 1 as shown in Fig. 3.8 and detected at port 2 by a photo resistor. The optical components of the diplexer are not optimized for the HeNe laser wavelength but fringes are still detectable. The position of one mirror of the diplexer is slightly modulated by a piezo actuator at a frequency of a few hundred Hz. The variation of the signal from the HeNe at the photo resistor is fed into a lock-in amplifier. This lock-in amplifier provides an error signal which can then be used to actively control the diplexer resonances via the piezo actuator.
- In a second step the transmission of the QCL through the diplexer via the DC component of the heterodyne detector is fed into a second lock-in/feedback circuit to control the QCL current keeping the signal at the maximum of the diplexer transmission curve. Following this procedure the LO can be stabilized in frequency to $\sim$1 MHz RMS (see 3.4). The stabilization feedback loop consists of two Lase Lock units manufactured by TEM Messtechnik.

The Galvano Scanner

The IR signal to be detected is selected by means of a fast moving galvano scanner (manufacturer General Scanning, model M3). The measurement of five different sources are finally combined for one complete observation necessary for absolute and relative calibration:

- on-source on the sky
- off-source on the sky as reference
- blackbody emitter as hot load for calibration purposes
- absorber at ambient temperature as cold load for calibration purposes
- reference gas cell with globar for absolute frequency calibration

The processing of collected data to calibrated spectra is described in detailed in chapter 3.3.

The Detector

As mixer detector we use a four pixel Mercury Cadmium Telluride (MCT) p-i-n photo diode manufactured by Raytheon Vision Systems. Each pixel has an integrated resonator structure to optimize the sensitivity at a specific wavelength. The four different pixels cover the wavelength range from 7.5 μm to 12 μm at a quantum efficiency of up to 80 %. The mixer as well as an in–house built HEMT (high electron mobility transistor) amplifier with integrated bias-tee are cooled to LN_2 temperature. The co-axial cable connection between mixer and HEMT is minimized in length. This makes cable standing waves due to impedance mismatch negligible. Through combined detection of LO and broadband signal the mixer generates an IF signal with a bandwidth of up to 3 GHz in both, upper and lower sideband, simultaneously.

Beam matching and Optical Guide System

To adjust the beam waist from the telescope ($\omega_{telescope}$) to the beam waist at the diplexer ($\omega_{diplexer}$), the position where the two signals get superimposed, a combination of various collimating OAP mirrors are used. For a confocal diplexer the beam waist is depended on the wavelength of observation (λ) and the distance between the two mirrors d. It is given by

$$\omega_{diplexer} = \sqrt{\frac{d \cdot \lambda}{2 \cdot \pi}}, \tag{3.1}$$

whereas a maximum aperture efficiency of the telescope is achieved by a telescope waist of

$$\omega_{telescope} = 0.22 \cdot \sqrt{T_e} \cdot \frac{F}{D} \cdot \lambda \tag{3.2}$$

T_e is the so called Edge Taper. A maximum aperture efficiency of η=0.81 for circular antennas with unblocked aperture and Gaussian illumination can be achieved at a value of T_e=10.9 dB. F and D are the focal length and the aperture of the telescope [91]. The setup is designed to provide high flexibility in the implementation of different collimating OAP mirrors combinations to match the system to various telescopes as good as possible. Table 3.2 gives an overview of the values for the used instrument setup and telescopes.

Table 3.2: *Overview of the beam waist at the diplexer ($\omega_{diplexer}$) for the given instrument setup and the beam waists from the telescope ($\omega_{telescope}$) at the McMath-Pierce (MMP) Solar Telescope and the IRTF at a wavelength of 10.4μm.*

	mirror focus	mirror distance	$\omega_{diplexer}$
diplexer	60mm	21mm	223μm

		tel. focus	tel. aperture	$\omega_{telescope}$
telescope	MMP	82.6m	1.51m	414μm
	IRTF	105m	3m	265μm

To ensure accurate pointing on the target source the instrument is equipped with an optical guide system. The light from the telescope is split by a dichroic mirror into an IR and a visible component. The dichroic mirror is located in the collimated beam behind the focal plane of the telescope. Therefore it is ensured that the visible signal follows the same path as the IR and thus the visible beam is pointing to the same position on the sky as the IR detector. The IR signal is reflected at more than 90 % efficiency while the visible signal is transmitted at more than 50 %. The guide signal is then focused using a standard 140 mm photo lens and detected using a CCD camera (Santa Barbara Instrument Group, SBIG–STV).

These are the most important components in the optical part of the receiver assembled in the 80x60x45 cm^3 aluminum frame. It is directly mounted to the various telescopes during observation. To control the different components and to run the entire system a set of electronical equipment, described in the following chapter is necessary.

3.2.2 Electronical Equipment

The electronical equipment needed for operation of the instrument consists mainly of the following components:

- The **QCL Laser Control Module** fabricated by Spectra-Physics (Model: SP5820 & SP5720) is used to operate the QCL. Beside the low-noise power supply it provides temperature control of the QCL.

- The **Lase Locks** are utilized for frequency stabilization (TEM Messtechnik; Lase Lock 3.0).

- The **IF electronics** match the received signal from the detector to the back end spectrometer.

- The **Acousto Optical Spectrometer (AOS)** serves as back-end spectrometer and allows analysis of the IF signal with a spectral resolution of 1 MHz.

- The **PC** controls the measurement procedure and stores the received data.

IF electronics

The detector unit contains a first amplifier directly after the detector and provides a 0 - 3 GHz radio signal at a power level of approximately -50 dBm. This signal has to be processed to match the back-end spectrometer requiring a power level of approx. 10 - 20 dBm in a frequency range of 3.5 - 6.5 GHz. Therefore amplification and equalization of the incidenting signal is necessary as well as an additional frequency shift.

Due to the implementation of a new detector with a broader bandwidth and a new broadband AOS the IF electronics had to be completely designed within this work. The principle setup is shown in Fig.3.9. Via a SMA connector the signal, coming form the optical receiver is fed into the IF box and gets amplified and equalized followed by a system of several switches to provide a selection between the signal, a zero signal and a comb signal. The comb signal with a spacing of $\delta\nu$=100 MHz is provided by a comb generator manufactured by EMF (Series 95).

After the switches a digital variable attenuator provides remotely selectable variation of signal levels because intensity levels of the targeted astronomical sources can be essentially differ (e.g. Sun, faint stars). A splitter couples a fraction of the broadband signal to the RF crystal detector especially useful for the detection of faint sources.

The signal incidents on a mixer also fed by an amplified signal from a tunable VCO (Voltage Controlled Oszillator) at 6.5 GHz (Hittite; HMC358MS8G) causing the frequency shift to the required frequency range of the AOS. The shifted signal is equalized and amplified in a last step before it is fed into the AOS at an level of $\sim$ 10 - 20 dBm. A schematic of the IF assembly is shown in Fig. 3.9.

The Acousto Optical Spectrometer

The real-time analysis of the IF signal is provided by an (in house built) AOS with a bandwidth of 3 GHz [90].

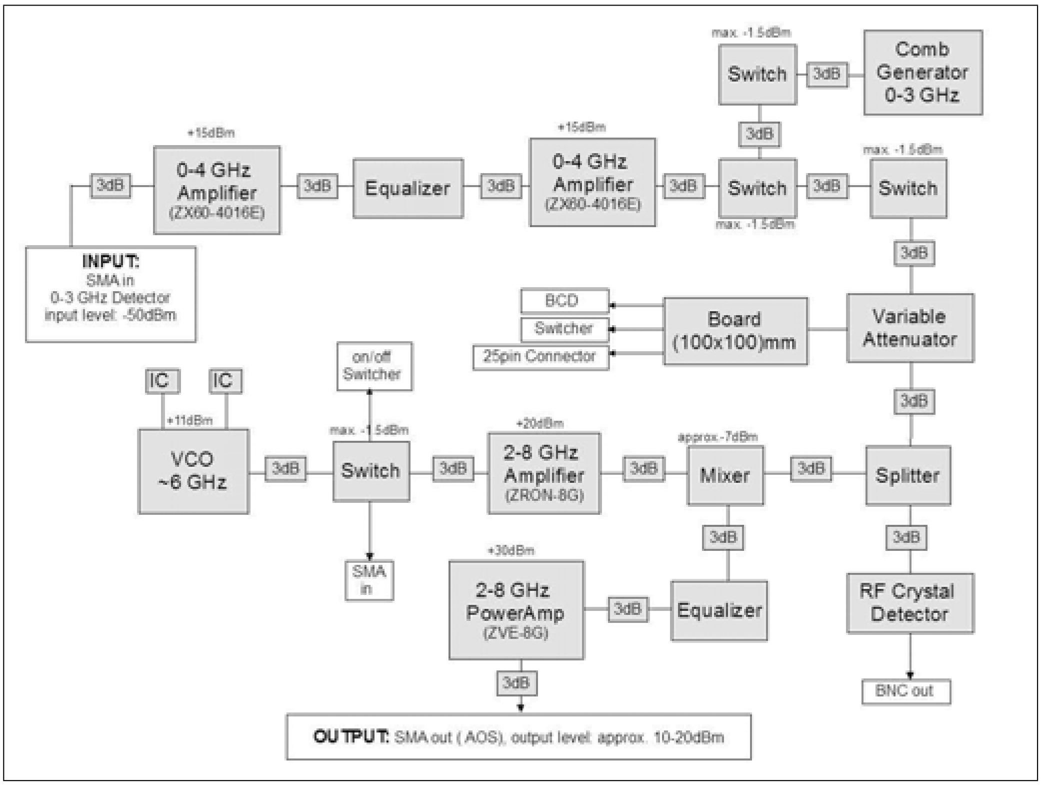

Figure 3.9: *Schematic of the electrical components included in the IF-box. The IF signal from the mixer detector is fed into the IF-box at a level of -50dBm. After first amplification the comb generator and the zero signal can be selcted. A digital variable attenuator provides variation of signal levels before a splitter couples out broadband signal to the RF crystal detector. The signal incidents on a mixer which is also fed by an amplified signal from a VCO. The shifted signal from the mixer is equalized and amplified in a last step before it is fed into the AOS at a level of ∼10-20 dBm.*

The basic idea of an AOS is to obtain spectroscopic information by the diffraction of light in a crystal, the so called Bragg-cell, modulated by ultrasonic waves (Fig.3.10). A piezoelectric transducer, driven by the IF signal from the mixer detector, generates an acoustic wave in the Bragg-cell. This acoustic wave modulates the refractive index and induces a phase grating. A collimated laser beam is send through the Bragg-cell and then focused on a linear CCD (6000 pixel), leading to a simultaneous detection of the full 3 GHz bandwidth. The angular dispersion of the diffracted light represents a true image of the radio frequency spectrum according to the amplitude and wavelengths of the acoustic waves in the crystal providing a resolution bandwidth of the AOS of ~ 1 MHz. The final spectra is displayed and stored via a PC.

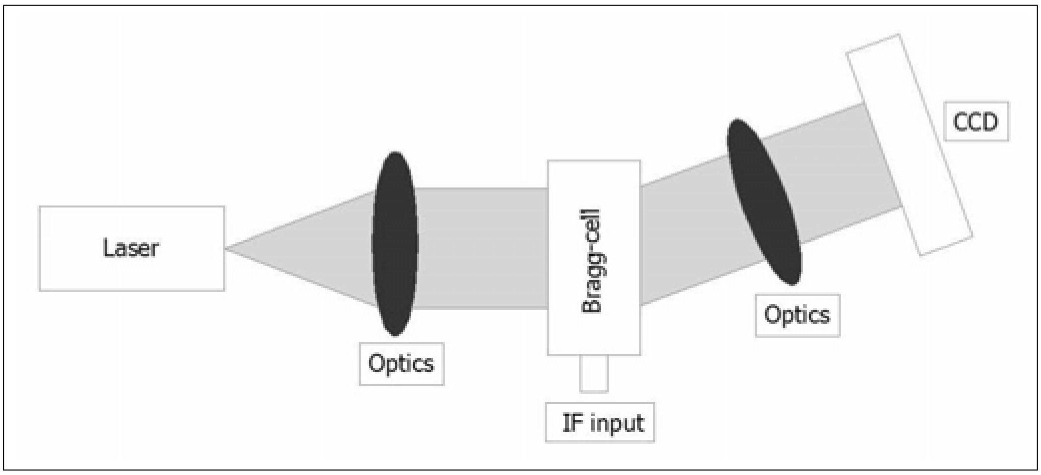

Figure 3.10: *Principle of the acousto optical spectrometer AOS used as back-end spectrometer in the heterodyne infrared receiver THIS*

3.3 Data Acquisition and Reduction Scheme

To get spectra with minimum noise contribution the following procedure has to be proven feasible. A typical integration cycle measures five positions in appropriate fractions of the total integration time in order to achieve the highest possible SNR (signal-to-noise ratio): on-source on the sky, off-source on the sky as reference, blackbody emitter as hot load for calibration purposes, absorber at ambient temperature as cold load for calibration purposes, and the reference gas cell with globar for absolute frequency calibration. This single cycles are added together resulting in one single spectrum, referred to as ”scan”. For planetary observations it has been proven to be feasible to add ∼32 cycles to one scan. If necessary, (e.g. due to weather problems) single cycles can be excluded from the resulting spectrum later on. In addition a zero measurement and a comb signal measurement are attached to every scan. The comb measurement with a spacing of 100 MHz is necessary to assure a precise frequency calibration of the AOS.

The calibrated spectrum is calculated using

$$J_i^D = \frac{S_i - R_i}{H_i - C_i} \cdot (J_H - J_C), \tag{3.3}$$

in which S, R, H and C denote the counts provided by the AOS while looking at on source / off source, on the hot load, and on ambient temperature, respectively, in a given time interval. The index i denotes the frequency pixel of the spectrometer and will be omitted in the following. Taking differences of counts in the numerator removes the background counts generated in the spectrometer and dividing by the blackbody differences corrects for the non-uniform gain of the receiver across the IF band. The differences in the count rates are directly proportional to the differences in (brightness) temperatures of the different radiation sources.

The factor $(J_H - J_C)$ (both values given in K) provides the brightness temperature calibration using the known temperatures of the calibration loads. Since we operate outside the range of the Rayleigh–Jeans approximation the brightness temperatures of the two loads J_H and J_C are to be calculated by using the Planck equation (see Eq. A.2). Thus Eq. 3.3 directly provides the brightness temperature difference J^D between the signal and reference position as seen by the detector including all losses, e.g. in the receiver and telescope optics. A more detailed description can be found in Sonnabend et al. [19, 86] and Schmülling et al. [11].

As described above spectra were taken both on and off the planet (i.e. source versus sky background) using two instrumental beam paths. In addition the source was also alternated (beam switched) between the two beams to minimize systematical errors like standing waves, etc. This technique of "double beamswitch" is a commonly used technique in radio astronomy.

Before single spectra are added to achieve an adequate SNR each individual spectra is first resampled to 1 MHz spectral resolution to account for the non-linearity of the acousto optical spectrometer.

In the case of planetary observations the individual beamswitched spectra have to be shifted in frequency to correspond to a single representative velocity, correcting for the known variation in the topocentric velocity between Earth and the observed planet. Then the single spectra are co-added to achieve spectra with similar SNR.

For planetary wind observations by Doppler shift measurements precise absolute frequency calibration is essential. This absolute frequency calibration is obtained from measurements of a reference gas absorption spectrum during the measurement procedure and yields frequency precision uncertainties of $< 1\,\mathrm{MHz}$ (see chapter 3.4). The difference between the measured frequency and the predicted frequency of the lines for the reference radial velocity yields the line-of-sight velocity v_{los} using the Doppler equation.

The weighted beam centroid position on the planet is known, yielding the position at which the line-of-sight velocity is measured. Depending on the given geometry the line-of-sight velocity can be converted into horizontal and vertical velocity components.

3.4 Receiver Performance

In the following section relevant parameters and measurements demonstrating the performance of the instrument are presented.

The sensitivity towards the source on the sky is probably the most important parameter for any astronomical instrument. It specifies the detection capability and limitations.

The spectral stability is important to make use of the nominal resolution of the back-end spectrometer. It is essential to verify that the line width of the LO is narrow enough and the frequency of the system is stable enough to meet the requirements of Doppler shift measurements.

And finally a very brief comparison between heterodyne and direct detections systems is given.

Sensitivity

For many years, gas lasers have been the only available LOs for mid-IR heterodyne observations. After the failed efforts using lead salt TDLs it was most important to prove that using a QCL (together with the diplexer for beam combining) instead of a CO_2 laser yielded equivalent performance. In Sonnabend et al. [20] it was shown that the system sensitivity is indeed equivalent during operation with both types of lasers.

To specify the sensitivity of a heterodyne receiver we use the system noise temperature T_{sys} commonly used in radio astronomy. It is dependent on the detector and its intrinsic specification corresponds to the noise power p of a non–ideal system per bandwidth.

$$k_B \cdot T_{sys} = \frac{p}{\delta_{res}}$$

k_B is the Boltzmann constant and δ_{res} is the resolution bandwidth. The main advantage of T_{sys} is that it allows intercomparison between different (heterodyne) instruments as it is not dependent on spectral resolution. It determines the minimum detectable temperature difference ΔT of the system via the well established radiometer function.

$$\Delta T = \frac{T_{sys}}{\sqrt{B_{fl} \cdot t_{int}}} \tag{3.4}$$

B_{fl} is the fluctuation bandwidth of the spectrometer and t_{int} the integration time. Observing time is usually limited and as shown in Eq. 3.4 the detection limit decreases linearly with increasing sensitivity but only with the square root of the observing time. The transformation from T_{sys} into NEP (Noise Equivalent Power) commonly used for receivers in other wavelength regions is given in App. A.

Neglecting all additional noise sources a heterodyne system has a natural sensitivity limit, the "quantum limit" T_{ql} which is set by the noise contribution caused by spontaneous emission in an ideal system. This quantum limit is determined by the frequency ν, the Planck constant h and k_B as

$$T_{ql} = \frac{h \cdot \nu}{k_B} \tag{3.5}$$

It represents the fact that the power of one photon per second and per Hertz is emitted by the mixer into the IF independent of the presence of a signal.

Using the heterodyne receiver THIS at 10 μm, as was the case for the observations presented in this work, results in a T_{ql} of 1440 K for double sideband operation. This value converts to a NEP of $\sim 8 \cdot 10^{-17}$ W/$\sqrt{Hz}$ (see Eq. A.5).

The sensitivity of the system can be measured by observing loads at known temperatures as discussed in App. A and Eq. A.2 and A.3. Meanwhile, the best performance achieved at 10.4 μm wavelength yielded a system noise temperatures of below 2500 K or a NEP of $\sim 1.4 \cdot 10^{-16}$ W/$\sqrt{Hz}$. This value is only 70 % above the quantum limit which is an exceptionally good value for any heterodyne receiver! Fig. 3.11 shows a typical sensitivity over the full 3 GHz bandwidth of the AOS with a mean system noise temperature of 3100 K at a wavelength of 10.4 μm routinely reached during astronomical observations.

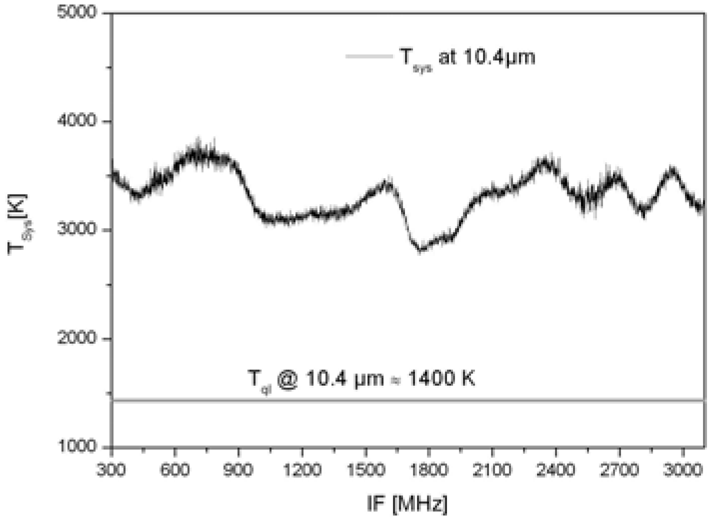

Figure 3.11: *Instrument performance at 10.4 μm wavelength. Shown is the system noise temperature T_{sys} vs. the IF. The value for T_{sys} is approximately two times above the quantum limit. The fluctuations with IF frequency are due to impedance mismatch and standing waves in the IF processing electronics.*

Especially for detection of faint sources (e.g. stars) it is important to provide prognoses of the detection limits of THIS. Using Eq. 3.4 the system noise temperature of 2500 K leads to a minimal detectable brightness temperature difference of 50 mK within 10 minutes at the fluctuation bandwidth of 1 MHz. This corresponds (see also Eq. B.1) to a minimum flux difference of $\Delta F_{\frac{1}{\lambda}} = 0.4\,\mathrm{ergs}/(\mathrm{s}\cdot\mathrm{cm}^2\cdot\mathrm{cm}^{-1}\cdot\mathrm{Sr})$ detectable with THIS with the current setup within the given 10 min.

Spectral Stability

Given the performance described above, the frequency stability of the system remains to be determined in order to qualify the instrument for high resolution observations. This is not only important for wind measurements by Doppler shifts but also for observations of weak signals requiring long integration times (in the order of a few hours).

To prove the quality of the spectral stability of the entire system molecular absorption lines (ethylene; pressure $\sim$5 mbar) were recorded. Data was taken every 30 s over a time periode of 4500 s simulating observing conditions. The absorption feature was fitted with a Gaussian line profile and the frequency position of the peak was determined. A typical result is shown in Fig. 3.12. The observed peak–to–peak variation in frequency is 2 MHz with a mean value of 1065.9 MHz and a standard deviation of 0.3 MHz. Variations are therefore sufficiently small for all discussed observing targets with a maximum observing duration of $\sim$ 1 h. In addition, due to the simultaneous detection of the reference cell during observation possible long term drifts in absolute frequency can be easily corrected.

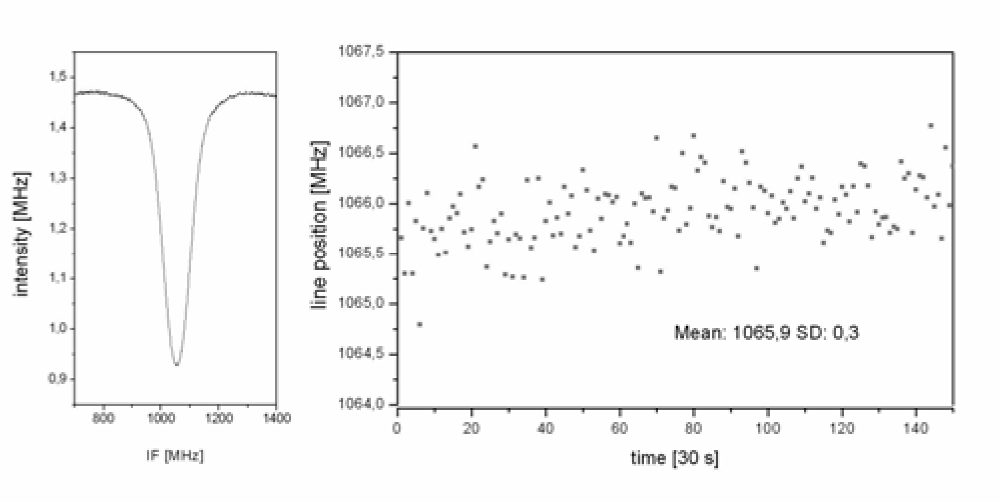

Figure 3.12: *Variation of the fitted frequency position of an ethylene absorption line around 10.4 μm detected through a gas cell (left). Data were taken every 30s over 4500s. The mean value and standard deviation are shown (right).*

The achievable spectral resolution depends not only on the frequency stability of the LO but also on its line width, the frequency resolution and stability of the back-end spectrometer and the IF processing.

The properties of the QCL-LO have been studied in detail in Sonnabend et al. [20]. The line width was shown to be less than 1 MHz. Recently, line widths of QCLs down to the kHz range have been reported [92].

The frequency stability of the AOS and the IF processing depends on the ambient temperature of the instrument. For most applications the inherent stability is sufficient but nevertheless the absolute frequency is controlled by routine measurements of a high–stability comb–generator spectrum with a known base frequency at the start of any observation. In case instabilities are detected the observed spectra can be corrected.

Heterodyne vs. Direct Detection

In this section I would like to give a short overview of the fundamental differences of heterodyne and direct detection without quantitative evaluation. A detailed analysis including quantitative considerations and background of noise comparison between direct and heterodyne detection in the IR can be found in Schieder [14].

The main difference of heterodyne detection compared to direct detection (e.g. grating spectrometers) is the order in the detection process and spectral analysis. A direct detection system receives signal photons and spectral splitting is done by a dispersive element before the detection.

In the case of heterodyne detection we also have to include the photons of the LO into our calculations and the spectral analysis of the generated IF signal takes place after detection and amplification of the signal. Signal and noise contributions have to be considered differently and advantages and disadvantages of both techniques have to be studied carefully.

The system noise temperature T_{sys} for a heterodyne system will always be restricted by the quantum limit T_{ql} (see Eq. 3.5 and 3.4) depending on the frequency whereas T_{sys} for a direct detection system (see Eq. A.4) can become significantly smaller than that value. On the other hand, the optical throughput for direct detection instruments reduces with higher spectral resolution while the sensitivity for a heterodyne receiver does not depend on the resolution. As a result, there is a specific resolution bandwidth at a given wavelength beyond which one technique is more favorable.

In addition extremely high resolution measurements ($\sim 10^7$) like the non-LTE observations presented in this work are not feasible by direct detection techniques due to technical limitations.

3.5 Important Specifications for the Cologne Heterodyne Receiver THIS.

To complete the chapter about the instrument THIS a summarized overview of the instruments specifications is given in the table below.

Table 3.3: *List of important specifications for THIS.*

Local Oscillator:	Quantum Cascade Lasers
Operating Wavelengths[1]:	7.75–13.25 μm
Spectral Resolution:	10^7, adjustable
Sensitivity:	System noise temperature <3000 K at 10 μm
Mixer Detector:	Mercury-Cadmium-Telluride photo diode
Detector IF Bandwidth:	3 dB cutoff, >3000 MHz
back-end Spectrometer:	AOS, 3 GHz, 6000 channels
Telescope Configuration:	Coude, Nasmyth, Cassegrain
	F# adjustable from $\sim$10–60
Receiver Dimension	80x80x45 cm^3
Receiver Wight:	$\sim$80 kg
Power Consumption:	$\sim$500 Watt
Cooling:	liquid nitrogen

[1] Detailed information can be found in Tab. 3.1

Chapter 4

"Venus, the goddess of love and beauty, vegetation goddess and patroness of gardens and vineyards."
"Mars, the god of war, spring, growth in nature, and fertility and the protector of cattle." (http://www.pantheon.org/articles)

Observations of Dynamics in Planetary Atmospheres

Observations of any planetary object require several independent decisions concerning observing date, time and location. Various aspects have to be taken into account depending on specific objectives and the used observing method. Most key points for the observations of dynamics in the atmosphere of Venus and Mars accomplished with the heterodyne receiver THIS are given below.

There is always a scientific motivation to choose a certain observing time and location on a planet. Spatial distribution according to latitude and local time of wind velocity including their variabilty, complementary measurements of wind velocities etc. have to be taken into account to reach the goal of gathering additional information on scientific questions.

The visibility of the object on the sky is a self-evident condition. A high transit elevation means long appearance within one night at low airmass. Only as long as the astronomical object is above $\sim 30^\circ$ elevation on sky ($\equiv 2$ airmass) observation is feasible. Obtaining a maximum of data within one run is especially important for observation with "visitor instruments" which have to be prepared and shipped to telescopes for every run.

The spatial resolution during observation is dependent on the diameter of the telescope mirror and on the orbital position of the planet. The closer to Earth the larger will be the apparent angular diameter of the planet increasing the precision of the spatial information of the measured wind velocities.

Another aspect regarding the orbital position is the relative Doppler shift between Earth and the targeted planet varying between $\pm 18\,\mathrm{km/s}$ resulting in frequency shift of $\leq 1.7\,\mathrm{GHz}$. This effect is even more severe for the outer planets like Jupiter or Saturn with relative Doppler shift velocities up to 28 km/s. The observed molecular line has to be close to the frequency of the LO (within the 3 GHz bandwidth of the detector) but free from disturbance by telluric lines.

For CO_2 the relative Doppler shift moves the observed molecular lines originating on Venus and Mars away from the the corresponding feature in the telluric atmosphere. In case of broad lines e.g. of methane observations are only possible at specific relative Doppler shift velocities between Earth and the targeted planet. These limitations are much easier to handle with tunable LOs like the QCLs used in THIS compared to gas lasers with fixed frequencies.

Atmospheric conditions at the location of the telescope to be used determine the quality of observation and are important as well as the design of the telescope. The requirements to the stability of our instrument is much higher using e.g. a Cassegrain telescope where the instrument moves with the telescope during observation compared to a Coude focus where the instrument stays in the same position during the entire observing run. Also not every telescope is accessible to "visitor instruments".

Finally, logistical and financial aspects are crucial to choose certain telescopes and time periods. Transporting the instrument by car to a telescope nearby is e.g. much easier and cheaper than shipping it overseas.

The resulting observing time is in general a compromise between the aspects given above and further conditions like availability of telescope time, successful telescope proposals, coordination with other observers etc.

Within this work the results of four observing runs addressing Mars and Venus at the McMath-Pierce Solar Telescope on Kitt Peak in Arizona, USA and at the NASA IRTF on Mauna Kea in Hawaii, USA are presented. An overview is given in the Tab. 4.1 below and detailed observing conditions are described in the following chapter 4.1 and 4.2

Table 4.1: *Overview of the observing runs accomplished within this work.*

observing period	observed object	telescope
December 2005	Mars	McMath-Pierce Solar Telescope
May/June 2007	Venus	McMath-Pierce Solar Telescope
November 2007	Mars, Venus	McMath-Pierce Solar Telescope
March 2008	Mars	NASA IRTF

4.1 Observation of Dynamics in Venus Upper Atmosphere

After a pause of several years Venus returned back into the focus of scientific exploration due to the European Space Agency's mission Venus Express (VEX). Recent ground-based observations in combination with data from VEX show more variability of the atmosphere than expected based on earlier data [93, 53, 52, 69, 42]. Hence dynamic measurements on Venus were and are highly demanded.

Having already verified the technique of wind measurements with the heterodyne receiver THIS on Mars it was obvious to apply this technique also to Venus. Consequently we participated in a coordinated campaign of different ground-based observation methods to support VEX. The related observing run took place in May/June 2007. A second observing run was accomplished in November 2007 taking the chance to get additional data during daytime while observing our main target (Mars) during the night. Further observations are planned in the near future (see chapter 5).

4.1.1 Observing Conditions: Venus

In particular for Venus the observing geometry for wind measurements is important for gaining separable information about the zonal wind component and SS-AS component. Observing Venus at maximum western/eastern elongation provides an illumination of the apparent disk of $\sim$50% with the subsolar point at the limb (see Fig. 4.1). At this configuration the SS-AS flow moves along the limb not contributing to the measured line-of-sight velocity. On the other hand observation at inferior conjunction is preferable for measuring the SS-AS flow. Having only a small lit Venus crescent provides the maximum SS-AS flow at the terminator in the line-of-sight direction. In addition at that time the angular diameter of the Venus disk is at maximum providing the highest possible spatial resolution. The dates given in Fig. 4.1 provide the largest angular diameter of ~ 55 arcsec close to inferior conjunction but a smaller angular diameter of ~ 24 arcsec during maximum western elongation.

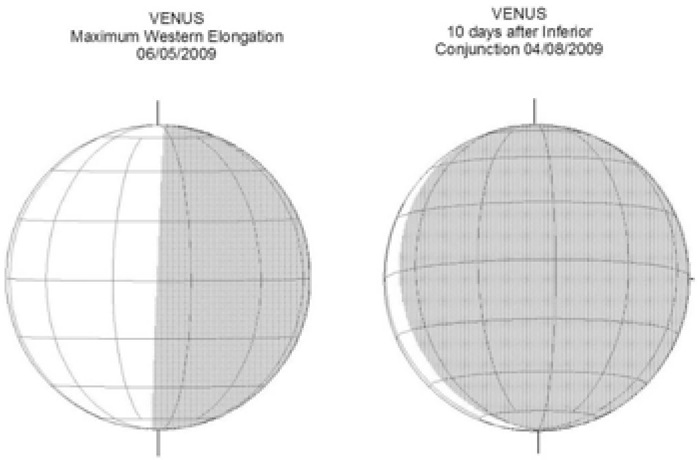

Figure 4.1: *The best condition to observe the SS-AS flow is close to inferior conjunction(right) when the terminator with the maximum SS-AS flow velocity is close to the limb position.*

Venus Campaign A (Kitt Peak, May 2007)

Participating in the coordinated ground-based campaign to support VEX (05/23/2007 – 06/09/2007) left little choice in selecting a specific observing geometry. Observations were carried out from May 28 to June 4, 2007 at the 1.5 m McMath-Pierce Solar Telescope of the National Solar Observatory on Kitt Peak, Arizona, USA (see Fig. 4.2). The observing geometry is shown in Fig. 4.3.

Venus orbital position was ~ 3 month prior to inferior conjunction. It was visible in the evening sky and was illuminated $52 - 56\%$. The subsolar point at $\sim 84\,^\circ$ West of CML and $1.6\,^\circ$ South was close to the West limb, allowing a determination of the zonal wind with negligible contribution from the SS-AS flow for the limb observations, assuming a SS-AS flow velocity originating near the subsolar point with radially symmetric outflow.

The angular diameter of Venus varied from 20.6 to 22.5 arcsec over the course of the observing period, compared to the diffraction-limited field of view (FOV) of the telescope of 1.7 arcsec. The relative sizes of the beam and the disk of Venus are pictured in Fig. 4.3. The pointing uncer-

Figure 4.2: *The McMath-Pierce Solar Telescope of the National Solar Observatory on Kitt Peak, Arizona/USA with a 1.5 m main mirror.*

tainty was estimated to be ~ 1 arcsec.

The Earth-Venus topocentric radial velocity varied between -14.4 and -13.6 km/s (approaching), determined from the HORIZONS on-line ephemeris service provided by the NASA Jet Propulsion Laboratory [94]. Having a ≤ 5 min acquisition time of each single measurement implies topocentric velocity changes of < 9 m/s, resulting in a modest maximum ~ 0.86 MHz broadening of the measured spectral feature, centered on the frequency at the midpoint of the scan.

The absolute frequency calibration is obtained from intermingled measurements of ethylene absorption lines at 959.4075 cm^{-1} and 959.3072 cm^{-1} yielding an absolute frequency precision uncertainty of ≤ 1 MHz.

The instrument THIS was mounted on the spectrograph table at the primary focus of the telescope as pictured in Fig. 4.4.

Observations were carried out at the West limb and at one additional position on the equator 45°West of the central meridian. 6 different latitudes on Venus (see Fig. 4.3) were observed with a total of 31 individual

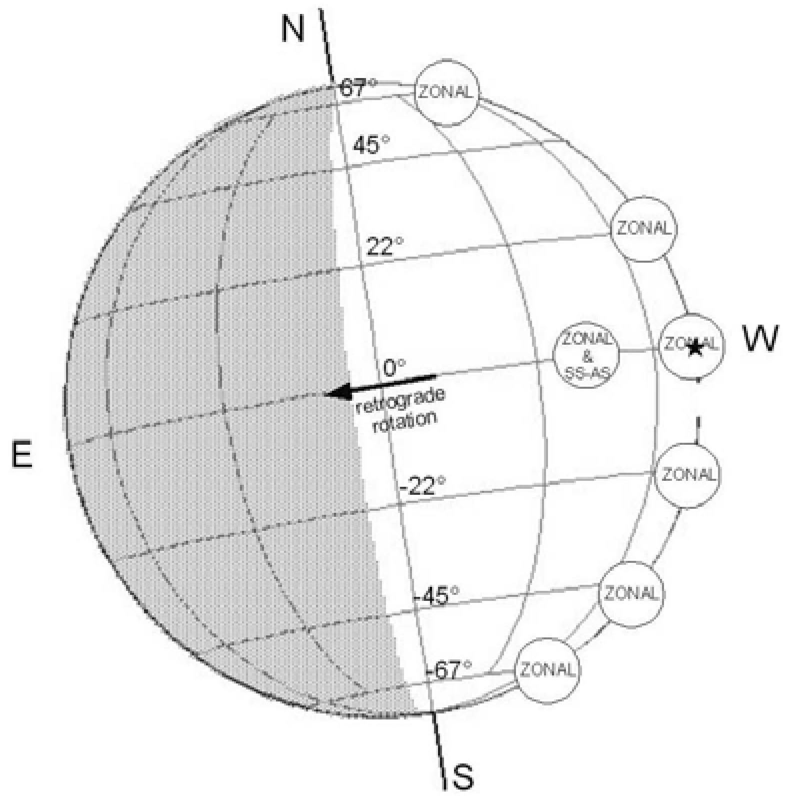

Figure 4.3: *Observing geometry on Venus during the period May 28 to June 4, 2007. The field of view was* ~ 1.7 *arcsec and observed positions are indicated. Typical integration time was* ≥ 16 *min. Venus (*~ 20 *arcsec in diameter) was half illuminated with a subsolar point near the equator/West limb position (black star). Hence observations at the limb lead to zonal wind information whereas the position on the planet was used to extract SS-AS flow information.*

observations, each lasting ≥ 8 min. An overview of relevant data for observation is given in Tab. 4.2. Retrieved spectra are displayed in Fig. 4.5 and Fig. 4.6.

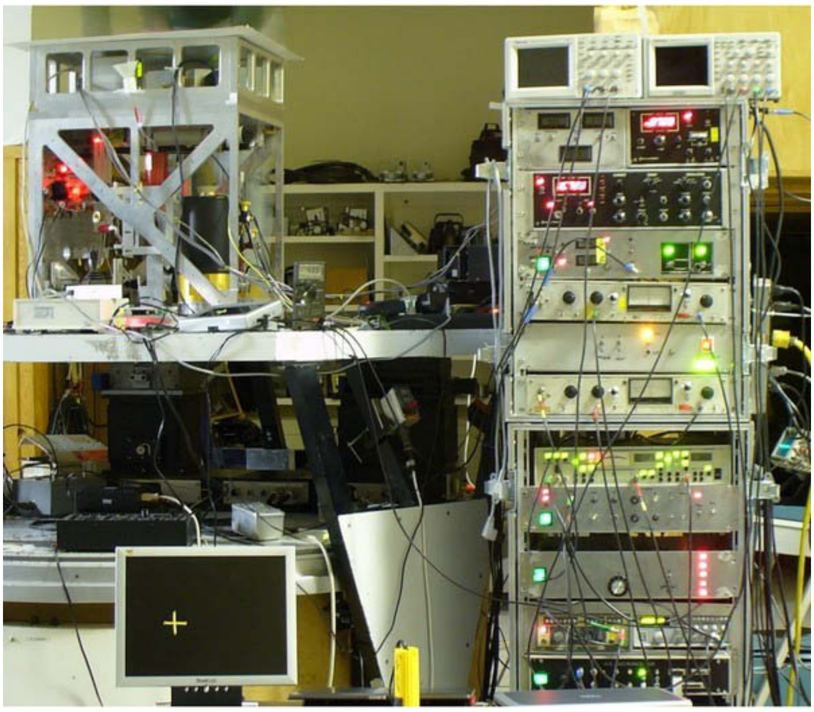

Figure 4.4: *The heterodyne spectrometer THIS at the primary focus of the 1.5 m McMath-Pierce Solar Telescope of the National Solar Observatory on Kitt Peak, Arizona/USA.*

Table 4.2: *Overview of the observed positions on Venus. Given are the positions on Venus, dates, the quantity of taken scans, the scan numbers and the total integration time in minutes.*

Campaign A (Kitt Peak, May and June 2007)

	lat/long [°]	date [month/day]	nr. of scans	scan	int. time [min]
1	67N/limb	(05/30),(06/01)	4	(32-33),(45-50)	32
2	22N/limb	(05/30),(06/01)	3	(26-27),(38-41)	24
3	0/limb	(05/28),(05/30)	2	(1-2),(2-3)	16
4	22S/limb	(05/29),(05/31)	6	(2-3),(9-12)	48
		(06/01),(06/03)		(36 and 38),(9-12)	
5	45S/limb	(05/30),(05/31)	5	(12-13),(25-28)	40
		(06/01)		(42-45)	
6	67S/limb	(05/31),(06/01)	6	(39-42),(50-53)	48
		(06/03)		(29-32)	
7	0/45W	(05/28),(05/30)	5	(9-10),(37-40)	40
		(06/04)		(26-29)	

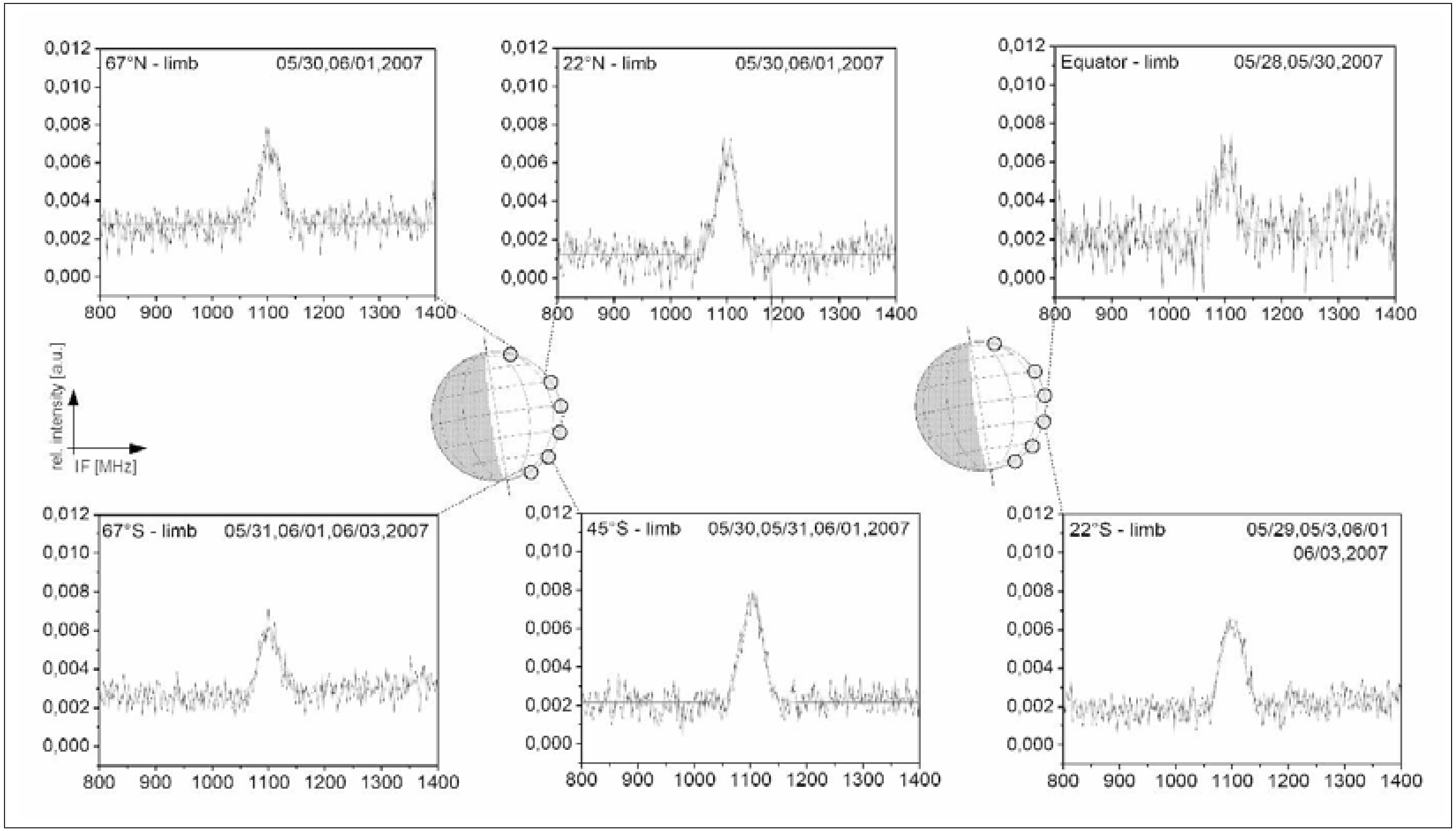

Figure 4.5: *Spectra from several positions at the western limb on Venus retrieved during the observation run at the McMath-Pierce Solar Telescope of the National Solar Observatory on Kitt Peak, Arizona/USA in May and June 2007. Measured data is shown in black whereas the best fit is given in red.*

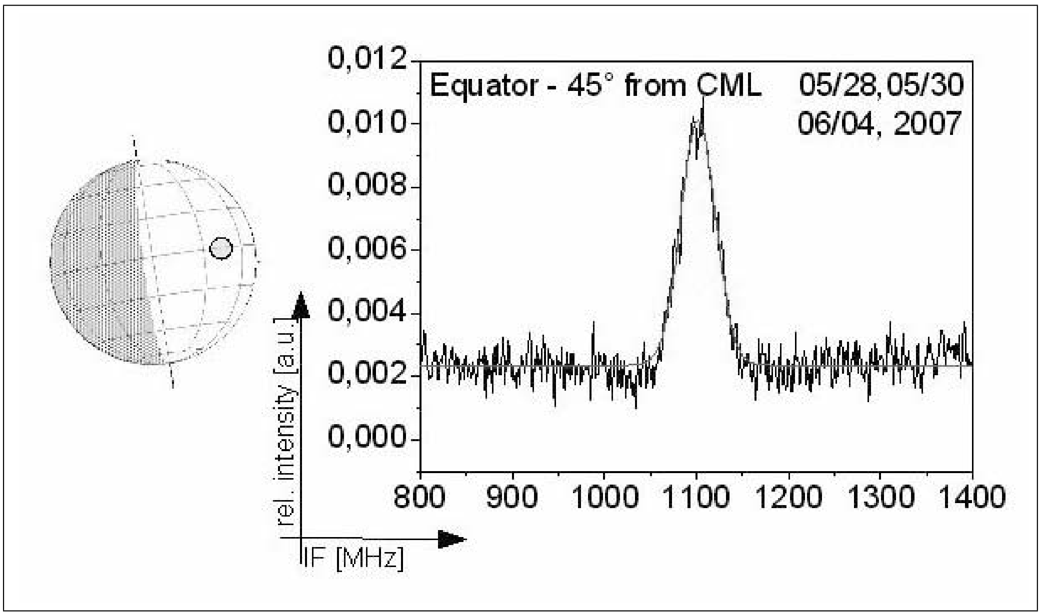

Figure 4.6: *Measured spectrum (black) and the best fit (red) at a position 45°West from CML on Venus retrieved during the observation run at the McMath-Pierce Solar Telescope of the National Solar Observatory on Kitt Peak, Arizona/USA in May and June 2007.*

Venus Campaign B (Kitt Peak, November 2007)

The second observing run took place in November 2007 once again at the 1.5 m McMath-Pierce Solar Telescope. Applicable data was collected from November 23 to November 28, 2007. Venus was observable in the morning sky from ∼6:00 am to ∼12:00 am (with reference to Mountain Standard Time UT-7 h, the local time in Arizona). The observation geometry is displayed in Fig. 4.7.

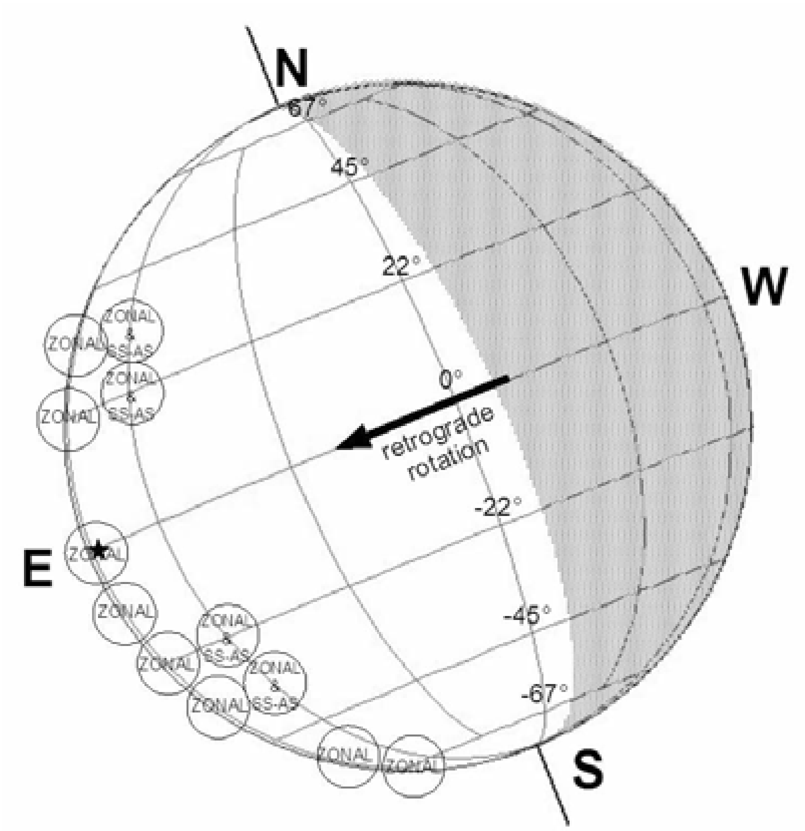

Figure 4.7: *Observing geometry of Venus during the targeted period November 23 to 28, 2007. The field of view was* ~ 1.7 *arcsec and observed positions with an integration time* ≥ 16 *min are indicated. Venus (*~ 18 *arcsec in diameter) was slightly more than half illuminated with a subsolar point close the equator/East limb position (black star). Hence observations at the limb lead to zonal wind information whereas the position on the planet was used to extract SS-AS flow information.*

The conditions were similar to the May run. This time Venus, ~ 3 month past inferior conjunction (August 18, 2007), was moving away from Earth at a topocentric radial velocity varying between +12.4 and

+12.3 km/s during the observing period. Consequently the eastern half of the planetary disk was illuminated for this observing campaign. Illumination of the Venusian disk varied between 62 % to 65 % within the time period. The subsolar point at $\sim$ 71° East of central meridian longitude (CML) and 2.3° South was close to East limb (see Fig. 4.7).

The angular diameter of Venus was slightly smaller than during observing campaign A varying from 18.0 to 19.1 arcsec over the course of the observing period, compared to the FOV of the telescope of 1.7 arcsec. The pointing uncertainty was estimated to be $\sim$ 1 arcsec.

Limb measurements are used for zonal wind determination due to minor influence of the SS-AS component. 8 different latitudes on Venus (see Fig. 4.7) were observed with a total of 21 individual observations, each lasting $\geq$ 8 min. Measurements at 45 ° East of CML were used to retrieve the SS-AS flow velocity. In this case 4 different latitudes on Venus were observed with 8 individual observations of $\geq$ 8 minutes.

An overview of the observed positions are given in Tab. 4.3 below. Fig. 4.8 and Fig. 4.9 show several example spectra at various positions on the planet.

Table 4.3: *Overview of the observed positions on Venus during observing campaign B in November 2007. Given are the positions on Venus, dates, the quantity of taken scans, the scan numbers and the total integration time in minutes.*

Campaign B (Kitt Peak, November 2007)

	lat/long [°]	date [month/day]	nr. of scans	scan	int. time [min]
1	33N/limb	11/25	3	(0-5)	24
2	22N/limb	11/23	2	(26,27,29,30)	16
3	0/limb	11/25	2	(6-9)	16
4	11S/limb	11/23	2	(18-21)	16
5	22S/limb	11/23	2	(22-25)	16
6	33S/limb	11/23	2	(1-4)	16
7	56S/limb	11/24	2	(12-15)	16
8	67S/limb	11/24	3	(16,17,22-26)	24
9	33N/45E	11/28	2	(1-3,7)	16
10	22N/45E	11/24	2	(8-11)	16
11	22S/45E	11/24	2	(4-7)	16
12	33S/45E	11/23	2	(5-8)	16

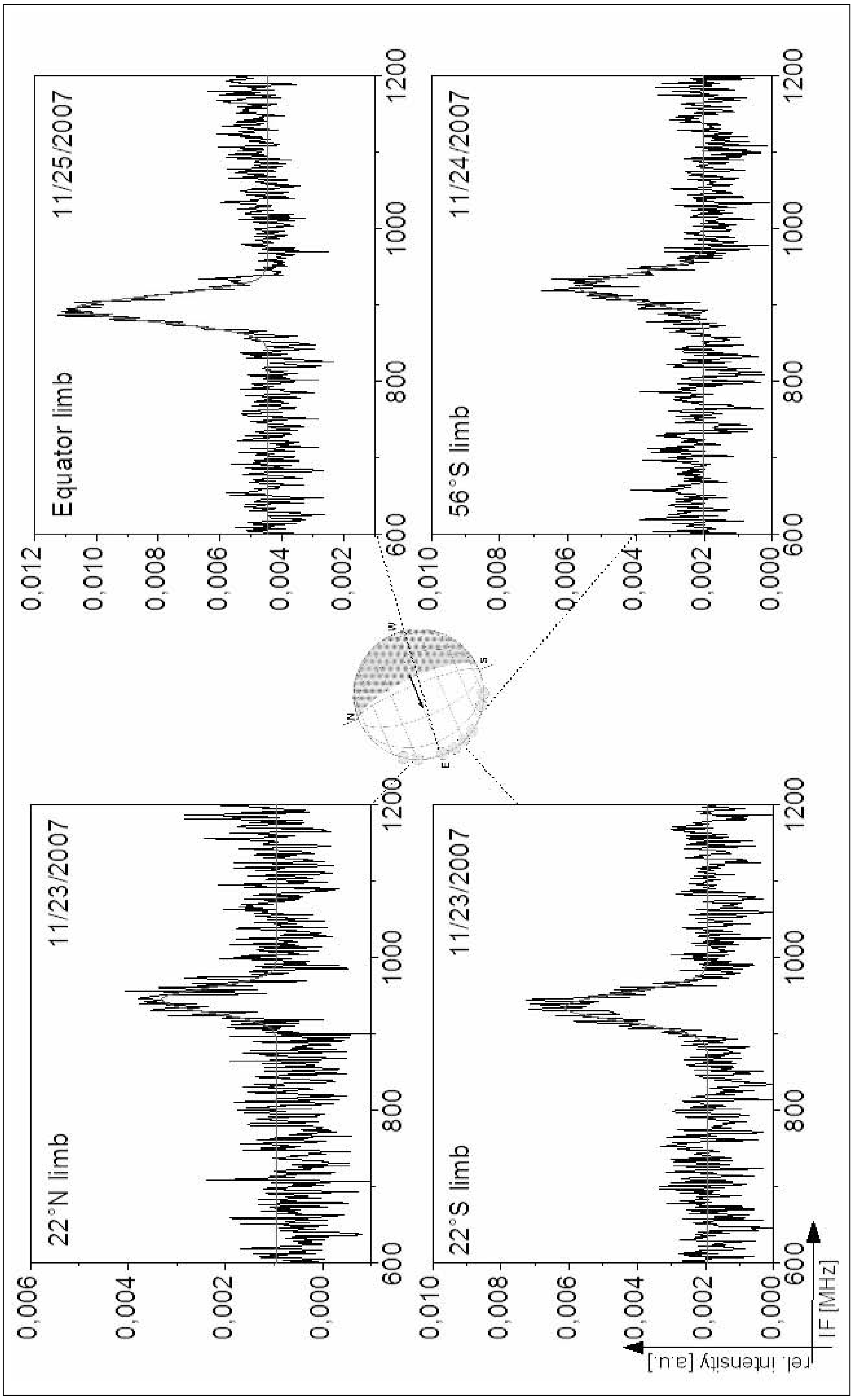

Figure 4.8: *Measured sample spectra (black) from several positions at the eastern limb on Venus retrieved during the observation campaign B in November, 2007 at the McMath-Pierce Solar Telescope of the National Solar Observatory on Kitt Peak, Arizona/USA in November 2007. The spectral resolution of the spectra are 1 MHz and the red line gives the best Gaussian fit to data.*

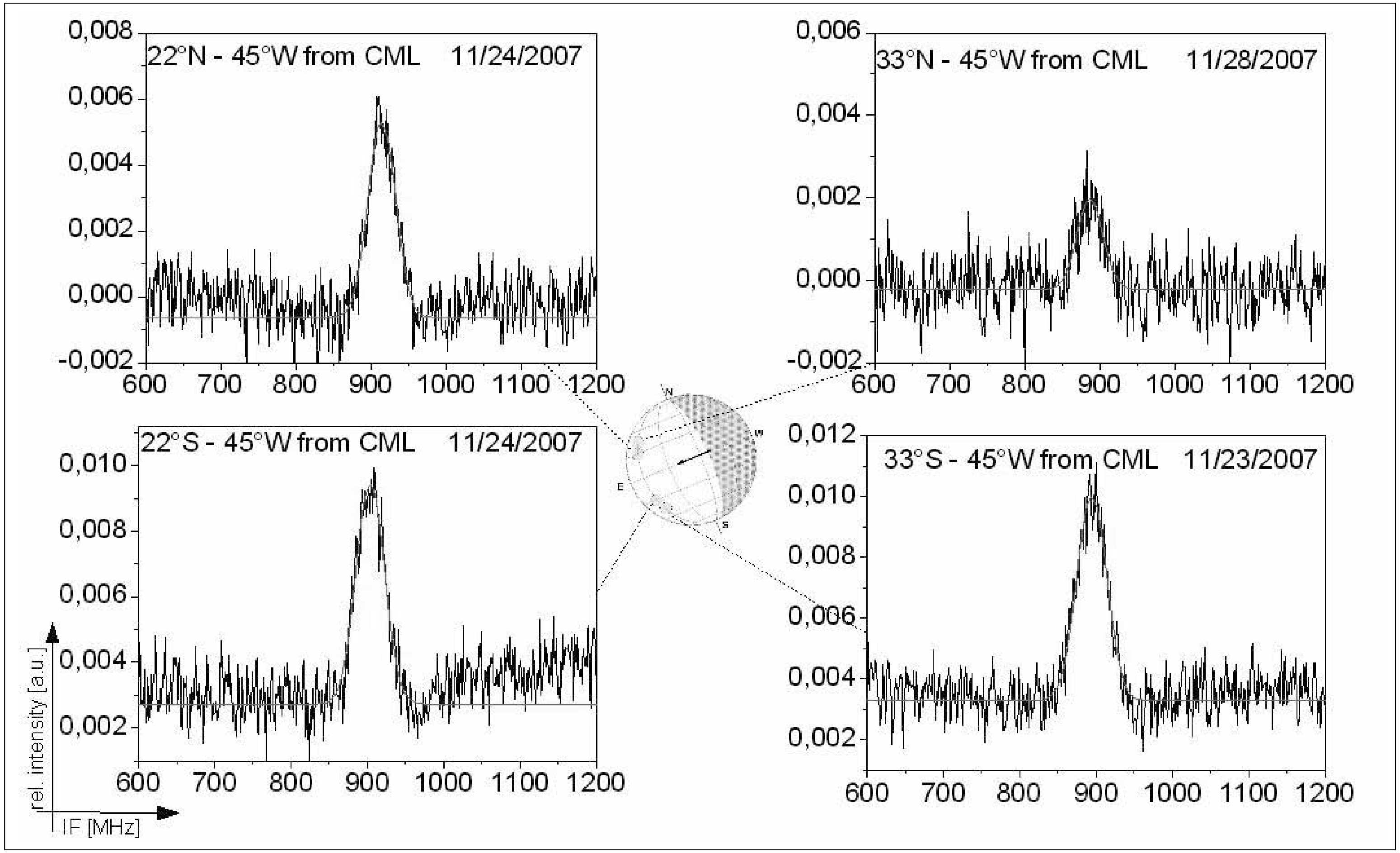

Figure 4.9: *Sample spectra at a positions 45°East from CML on Venus retrieved during the observation run at the McMath-Pierce Solar Telescope of the National Solar Observatory on Kitt Peak, Arizona/USA in November 2007. Plotted in black are the measured spectra with a spectral resolution of 1 Mhz whereas the red line gives the best Gaussian fit.*

4.1.2 Data Handling and Results for Venus Observations

The integration time for each spectrum was chosen such that a similar SNR for all spectra was reached thus yielding comparable uncertainties obtained from fitting each measured line with respect to width, intensity and frequency. Occasionally the spectra were combined from data samples acquired over several days in order to obtain a higher signal-to-noise ratio (SNR). This approach was especially necessary for the Venus campaign A in May 2007. Dates and integration times are noted in Tab. 4.2 and Tab. 4.3.

During the observation runs the true line profile of the non-LTE CO_2 P(2) emission line at 959.3917 cm^{-1} (10.423 μm) in the atmosphere of Venus was measured. A typical retrieved spectrum including a best fit to data is shown in Fig. 4.10. The emission line of this transition is not contaminated by telluric absorption features, making it a good probe of gas velocity.

A Gaussian line profile fitted to the ethylene absorption reference spectrum provides absolute frequency calibration of the LO. The frequency uncertainty in these fits (1 - σ confidence) reaches values as small as 0.3 MHz. Venusian CO_2 lines are fitted similarly using a Gaussian emission line profile, yielding the line-center frequency to high precision up to 0.3 MHz (see also errors given in Tab. 4.4).

The difference between the measured line frequency and the frequency predicted for the reference radial velocity yields the line-of-sight velocity v_{los} via the Doppler shift equation. The weighted beam centroid position on Venus is known, yielding the position at which the line-of-sight velocity is measured. For this position the line-of-sight velocity is converted to the horizontal velocity using the projection factor known from the observing geometry.

As mentioned above the observing geometry was not advantageous to retrieve information about the SS-AS flow. In order to compare these measurements with other observations and models a SS-AS flow was extracted from the observations on the planet based on two approximations:

a.) Assuming a constant zonal wind velocity along one latitude the corresponding zonal wind component measured from the limb observation can be subtracted from the measurement at 45° from CML. The resulting wind component describes the SS-AS flow and by projection along the trajectory from the SS-point to the AS-point the outflow SS-AS v_{SS-AS} can be determined.

b.) The second assumption is that the SS-AS horizontal outflow velocity increases linearly with the solar zenith angle (SZA) (see

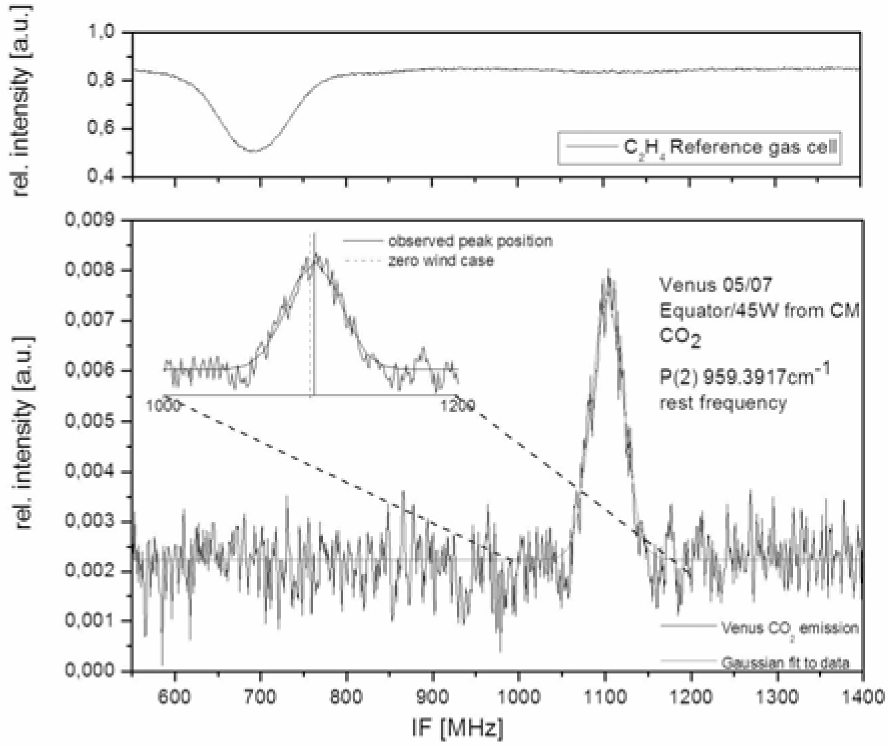

Figure 4.10: *Typical non-LTE CO_2 emission spectrum from Venus used to retrieve wind velocities from Doppler shifts. Shown is the P(2) line at 959.3917 cm^{-1}. Data was taken at the equator and 45° offset from Venus central meridian during the coordinated ground-based observing campaign to support Venus Express on June 3, 2007 (Campaign A). In the upper panel a spectrum from a reference gas cell was used to determine the exact LO frequency.*

chapter 2), reaching its maximum value v_{max} at the terminator. Hence we can calculate v_{max} using Equ. 2.1 and the outflow velocity v_{SS-AS} for any value of solar zenith angle. By doing this the SS-AS flow velocity at the terminator can be determined from velocity measurements anywhere on the disc.

A precise description of the retrieval of the SS-AS flow from line-of-sight velocities is given in Appendix C.

The results of mesospheric wind velocities by Doppler shift measurements of CO_2 non-LTE emission lines for both observing runs are given in Tab. 4.4 and Tab. 4.5 and displayed graphically in Fig. 4.11.

The sign of the frequency shift and the line-of-sight velocity is defined in reference to the observer. Negative frequency shifts and negative wind values for v_{los} indicate an approaching velocity with respect to the observer. In contrary the signs of zonal wind velocities (v_{zonal}) and the SS-AS flow velocities (v_{SS-AS}, v_{max}) are defined in reference to Venus. Positive zonal wind velocities have the same direction as the rotation of the solid planet. For Venus it is widely used to call this direction, describing also the orientation of the super-rotation, "retrograde". For the SS-AS flow velocity "positive" is defined as in the direction from the subsolar point to the antisolar point.

Table 4.4: *Overview of the retrieved line-of-sight velocities v_{los} in the atmosphere of Venus during the observation campaigns A and B in 2007 at the McMath-Pierce Solar Telescope (Kitt Peak, Arizona, USA). Given are date (occasionally data of different dates are added to one spectrum for analysis) and positions on the planet as well as integration time t_{int} on the planet (∼45% of total integration time), the ν_{los} and the resulting v_{los}. Negative frequency shifts and negative wind values for v_{los} indicate an approaching velocity (towards Earth). All errors are given at 1 - σ confidence.*

Venus Campaign A (Kitt Peak, May 2007)

	lat/long	date	t_{int}[min]	ν_{los}[MHz]	v_{los}[m/s]
1	67°N/limb	05/30,06/01	24	-2.0±0.4	-21±4
2	22°N/limb	05/30,06/01	18	-1.1±0.4	-11±4
3	0 ° /limb	05/28,05/30	18	-0.3±0.6	-3±7
4	22°S/limb	05/29,05/31,06/01,06/03	36	-0.7±0.4	-7±4
5	45°S/limb	05/30,05/31,06/01	30	-2.9±0.3	-30±3
6	67°S/limb	05/31,06/01,06/03	36	-1.6±0.4	-16±4
7	0 ° /45°W	05/28,05/30,06/04	36	-1.8±0.3	-18±3

Venus Campaign B (Kitt Peak, November 2007)

	lat/long	date	t_{int}[min]	ν_{los}[MHz]	v_{los}[m/s]
8	33°N/limb	11/25	24	3.8±0.8	40±9
9	22°N/limb	11/23	16	2.5±0.6	26±7
10	0 ° /limb	11/28	24	0.8±0.4	8±4
11	11°S/limb	11/23	16	3.0±0.7	31±7
12	22°S/limb	11/23	16	3.0±0.7	31±7
13	33°S/limb	11/23	16	0.9±0.2	9±24
14	56°S/limb	11/24	16	3.6±0.8	38±8
15	67°S/limb	11/24	24	3.3±1.	34±16
16	33°N/45°W	11/28	16	3.2±1.2	33±12
17	22°N/45°W	11/24	16	0.4±0.5	4±5
18	22°S/45°W	11/24	16	0.1±0.4	1±4
19	33°S/45°W	11/23	16	0.8±1.0	8±11

Table 4.5: *Overview of the retrieved wind velocities in the atmosphere of Venus for all observed positions (see also Tab. 4.4). Zonal wind velocities v_{zonal} and SS-AS flow velocities v_{SS-AS} are determined by line-of-sight velocities taking the beam-weighted beam centroid offset and the projection into account. The maximum cross terminator velocity v_{max} is with their 1 - σ errors. Positive zonal wind values indicate retrograde velocities, meaning rotation of the atmosphere in the same direction as the Venus solid body. Positive SS-SA wind velocities present a flow direction from the subsolar to antisolar point.*

Venus Campaign A (Kitt Peak, May 2007)

	lat/long	projection	v_{zonal}[m/s]	v_{SS-AS}[m/s]	v_{max}[m/s]
1	67°N/limb	0.91	23±5	-	-
2	22°N/limb	0.96	12±4	-	-
3	0° /limb	0.96	3±7	-	-
4	22°S/limb	0.96	7±4	-	-
5	45°S/limb	0.95	32±4	-	-
6	67°S/limb	0.91	18±4	-	-
7	0° /45°W	0.71	-	26±4	52±18

Venus Campaign B (Kitt Peak, November 2007)

	lat/long	projection	v_{zonal}[m/s]	v_{SS-AS}[m/s]	v_{max}[m/s]
8	33°N/limb	0.93	43±9	-	-
9	22°N/limb	0.94	28±7	-	-
10	0° /limb	0.94	9±4	-	-
11	11°S/limb	0.94	33±9	-	-
12	22°S/limb	0.94	33±9	-	-
13	33°S/limb	0.93	10±26	-	-
14	56°S/limb	0.89	42±9	-	-
15	67°S/limb	0.85	41±16	-	-
16	33°N/45°W	0.23	-	-23±54	-47±108
17	22°N/45°W	0.43	-	33±12	80±29
18	22°S/45°W	0.45	-	47±9	123±24
19	33°S/45°W	0.24	-	-7±44	-15±97

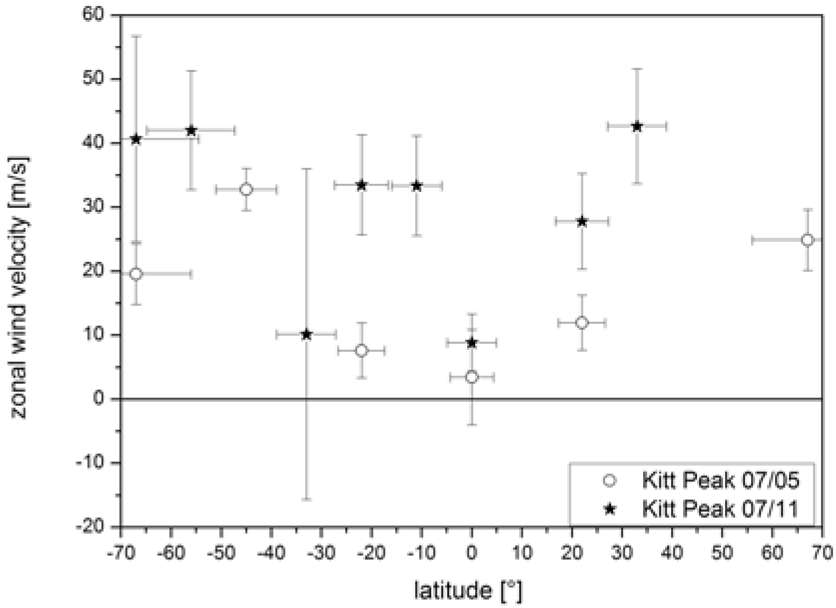

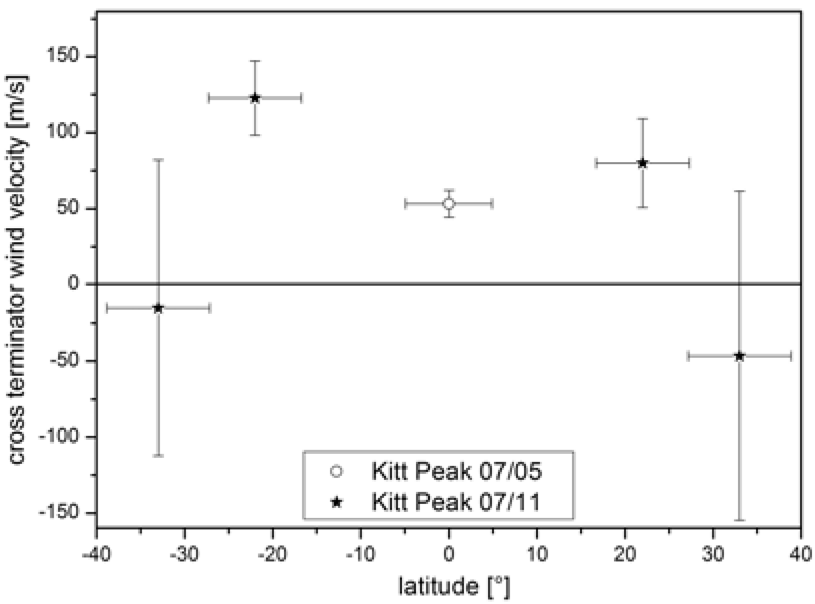

Figure 4.11: *Zonal wind velocities from West limb positions (upper panel) and SS-AS wind velocities retrieved from "on planet" observations (see Fig. 4.3 and 4.7). Data as taken from May and November 2007 (see Tab.4.5) at the McMath-Pierce solar telescope on Kitt Peak, Arizona. The total integration time is* ≥ 16 *min.*

4.1.3 Venus Observations - Data Interpretation and Comparison to other Observing Techniques

In a simplified model of the Venusian atmosphere the superrotation influence is assumed to decrease with altitude above ~ 90 km to be replaced by SS-AS flow dominance at an altitude above ~ 120 km [44, 45, 46, 47]. Probing an altitude region around 110 km the presented observations are targeting a region where both wind features are existent.

In the following, wind velocities which are also summarized in Tab. 4.5 will be marked with the letter A and B corresponding to the two observing campaigns A in May 2007 and B in November 2007.

The Zonal Wind Velocity

The results of both observation runs show no significant wind velocity at the equator. Values of only 3 ± 7 m/s (A) and 9 ± 4 m/s (B) show no indication for a superrotation component at the equator in the addressed altitude region. However an increase in zonal wind velocity with latitude towards the North and South up to 45 m/s was found during both observing runs. This result was unexpected since models assume a maximum zonal wind velocity at the equator for superrotation. All errors are given at 1 - σ confidence.

During observing campaign A a maximum zonal velocity of 32 ± 4 m/s was found at southern mid-latitude, 45 ° S. At higher latitude, 67 ° S, the velocity decreases once more to 18 ± 4 m/s and weak retrograde mid-latitude jets, parallel to Venus' rotation seem to be a possible interpretation. A suitable spectrum to investigate the northern mid-latitude was not obtained but the velocity at the same high northern latitude, 67 ° N, is similar to the south, 23 ± 5 m/s. Newman et al. [60] also found mid-latitude jets from Pioneer Venus radio occultation data with a maximum of 140 m/s at ~ 70 km, decreasing above that altitude.

During the observing run B a low wind value at the equator and higher values at both hemispheres were found. However the results at the southern hemisphere up to 67 ° S do not show a decrease from mid-latitudes towards the poles. Hence it does not support the conclusion of a mid latitude jet. Unfortunately, the zonal wind value at 45 ° S shows an extremely high 1 - σ error. For all other positions wind velocities between 30 and 45 m/s are found. For the northern hemisphere only positions at a latitude lower than 33 ° N were measured, showing an increase of the wind velocity compared to the equator with values of 28 ± 7 m/s at 22° N and 43 ± 9 m/s at 33° N.

Temporal variation on short and long time scales have to be considered, an assumption strengthened by previous observations of Goldstein et al. [45] (25 ± 15 m/s) and Schmülling et al. [49] (39.6 ± 2.6 m/s and 34.7 ± 1.1 m/s). They found slightly higher values for the equatorial zonal retrograde component using also mid-IR heterodyne spectroscopy hence probing the similar altitude region. On the other hand the results of Goldstein et al. [45] and Schmülling et al. [49] were retrieved by fitting a global wind field model (combining zonal velocities and SS-AS flow) to several observations on the planet. The results are therefore strongly model dependent and hence a direct comparison between their and our results might be deceptive. In addition, a different observing geometry might probe different altitudes. The SZA does not have a direct effect on emission altitude, but it may affect local temperature and thus affect the inflation of the atmosphere locally by changing the scale height. As there is a steep gradient in wind velocity with altitude, changes in the non-LTE emission altitude will lead to a substantial change in wind velocity. A detailed analysis of the solar induced non-LTE processes leading to the emission line will hopefully provide more precise altitude information in future.

An even higher value of 130 ± 15 m/s for the zonal retrograde flow at an altitude of 110 km is presented by Lellouch et al. [52]. More recent observation report high temporal variability from 63 ± 10 m/s (within the ground-based observing campaign to support VEX) to even prograde wind velocities of -120 ± 90 m/s (data taken July, August 2006) within months at an altitude of 102 km [63]. This supports a strong "long" term variability. Whereas within the differnt observing runs the published data show a robust day-to-day stability.

Using mm-wave observations of CO Shah et al. [50] retrieved mean values for zonal wind velocities of 132 ± 10 m/s providing a dataset over the entire Venusian disk (from 70° S to 60° N) with a spatial resolution comparable to our measurements.

Probing even lower into the atmosphere other techniques found higher zonal wind velocities. Published results are summarized in Tab. 2.1 and Tab. 2.2 and displayed in Fig. 4.12. At 74 km altitude Widemann et al. [53] found equatorial velocities of 83 ± 27 m/s by observation of visible CO_2 lines. More recently, also within the coordinated ground-based campaign to support VEX, Widemann et al. [64] presented values around 100 m/s. Other Doppler shift measurements using reflected Fraunhofer lines at visible wavelength report values of 151 ± 16 m/s [65] and slightly lower values between 66 ± 5 m/s and 91 ± 6 m/s are presented by Gabsi et al. [66].

Compared to these results our values at an altitude around 110 km are low especially with respect to the published results of Lellouch et al. [63] who found even an intensification of mesospheric circulation with altitude in contrary to theory were the zonal component should decrease with altitude.

The SS-AS Flow

During the two observing runs described above, data from five positions:
equator / 45 ° West from CML (A),
22 ° N / 45° West from CML (B),
22 ° S / 45° West from CML (B),
33 °N / 45 ° West from CML (B) and
33 °S / 45 ° West from CML (B)
are available to determine the SS-AS flow velocity. With respect to the assumptions concerning the maximum SS-AS flow velocity in chapter 2.1, v_{max} is found to be 52 ± 18 m/s at the equator from data from campaign A. During campaign B values for v_{max} of -47 ± 108 m/s at 33 ° N, 80 ± 29 m/s at 22° N, 123 ± 24 m/s at 22 ° S, and -15 ± 97 m/s at 33 ° S are found.

The values at the equator and lower latitudes are generally lower and in one case comparable to the 120 ± 30 m/s previously found by Goldstein et al. [45], and 118.5 ± 1.5 m/s and 129.2 ± 1.2 m/s found by Schmülling et al. [49] using similar mid-IR heterodyne measurements. The values at 33 ° North and South are lower showing high errors due to the observing geometry. But the disadvantageous observing geometry during the time of our observations limits the significance of our results.

Values for the cross terminator SS-AS flow can also be determined using other ground-based techniques. Lower values, close to the presented SS-AS flow velocities from 40 ± 45 m/s up to even 322 ± 25 m/s [63] are published suggesting extremely high temporal variability. An overview of ground-based measurements is given in Fig. 4.12 and Tab. 2.1).

The measured wind velocities presented in this work are generally lower than those measured in previous observations and support a hypothesis of temporal and local variability in the upper mesosphere of Venus. The observing geometry in both runs was favorable to measuring the zonal component but disadvantageous for measuring the SS-AS flow. Thus the retrieval uncertainties for the SS-AS component are quite large and additional observation of SS-AS velocity would be recommendable. Further observations are required for the SS-AS flow as well as for the zonal wind component to investigate dynamical variability and to answer questions on its nature, temporal and spatial behavior, and possible connections to other phenomena in the Venus upper atmosphere. IR heterodyne observations are valuable due to high spatial resolution compared to other ground-based techniques. In addition, although the exact altitude is not yet determined the wind information originates in a narrow altitude range thus data analysis is not model depended and no deconvolution of the observed lines is necessary (see chapter 5).

Table 4.6: *Bibliography of wind velocity presented in Fig. 4.12*

zonal wind velocities		max. terminator velocity	
#	citation	#	citation
1-15	Lellouch et al. [63]	1-3	this work
16-19	Widemann et al. [64]	4-12	Lellouch et al. [63]
20-23	Gabsi et al. [66]	13	Goldstein et al. [45]
24	Gaulme et al. [65]	14	Lellouch et al. [52]
25	Goldstein et al. [45]	15,16	Schmülling et al. [49]
26	Lellouch et al. [52]	17	Shah et al. [50]
27,28	Schmülling et al. [49]	18-20	Lellouch et al. [52]
29,30	this work	21	this work
31-33	Lellouch et al. [52]		
34	Widemann et al. [53]		
35	Newman et al. [60]		

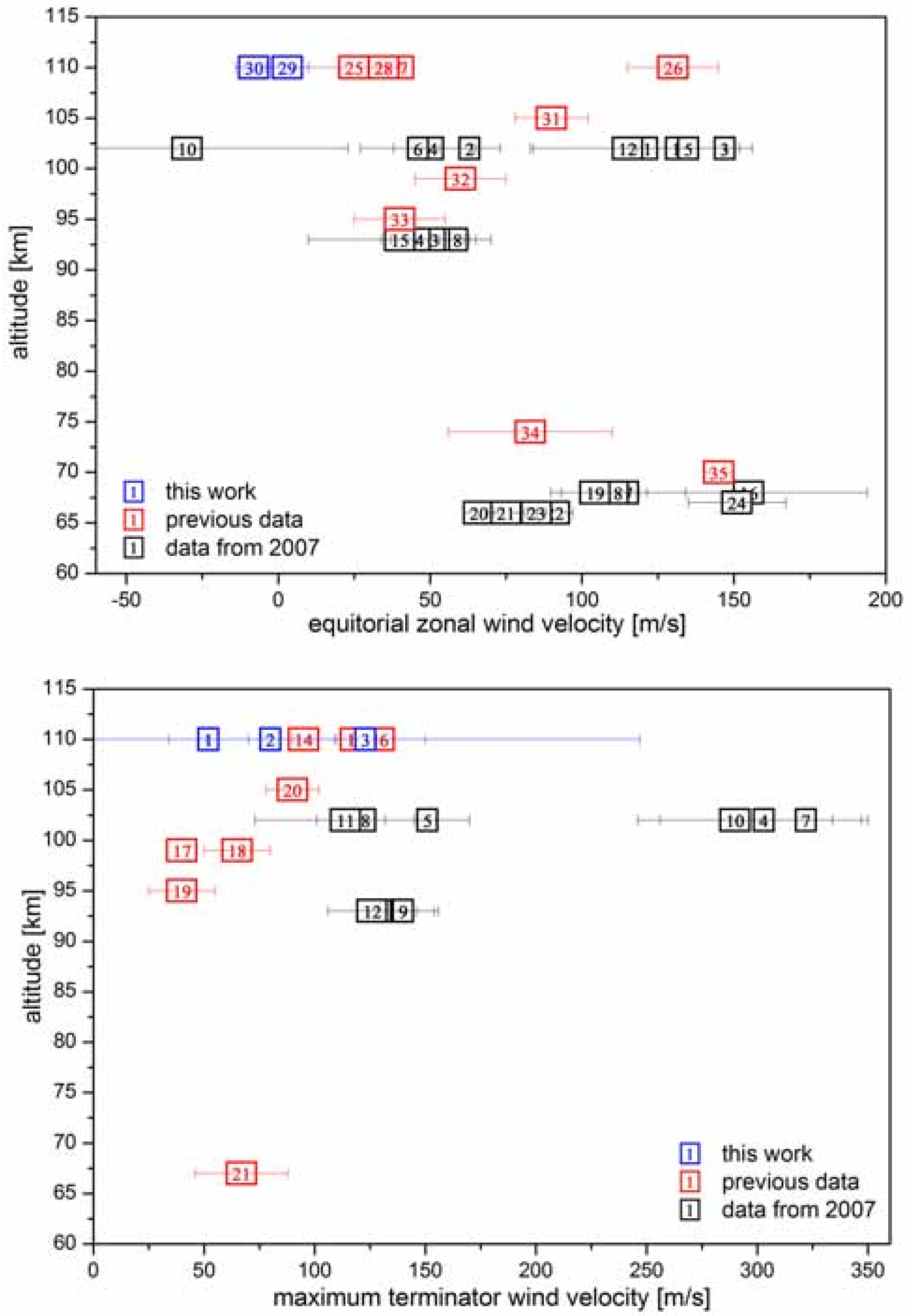

Figure 4.12: *Zonal wind velocities (upper panel) and maximum terminator velocities(lower panel) at different altitudes, gathered by different observing methods (mm-wave and visible observations of CO, MIR CO_2 observations). References are given in Tab. 4.6 Results in black were collected within in the ground-based observing campaign to support VEX and values in red are previous measurements from the eighties and nineties. Wind velocities retrieved within this work are plotted in blue. Values plotted in this figure are summarized in Tab. 2.1 and 2.2 including references.*

4.2 Observation of Dynamics in the Martian Mesosphere

Due to the significant similarities between Earth and Mars atmospheric models were transfered from Earth to Mars at an early point. With increasing computing power detailed low grid predictions about atmospheric parameters are possible. Especially over the past few years along with Mars Express the understanding of the Martian atmosphere improved significantly. However, direct measurement of dynamics and in particular observations of temporal variation on different time scales are still missing. This was the motivation to conduct several observing runs to measure wind velocities at different times and locations in the upper atmosphere of Mars. Of special interest was to verify a seasonal transition from a mid to high-latitude jet from the northern to the southern hemisphere as predicted by models [95]. To follow this evolution obser-

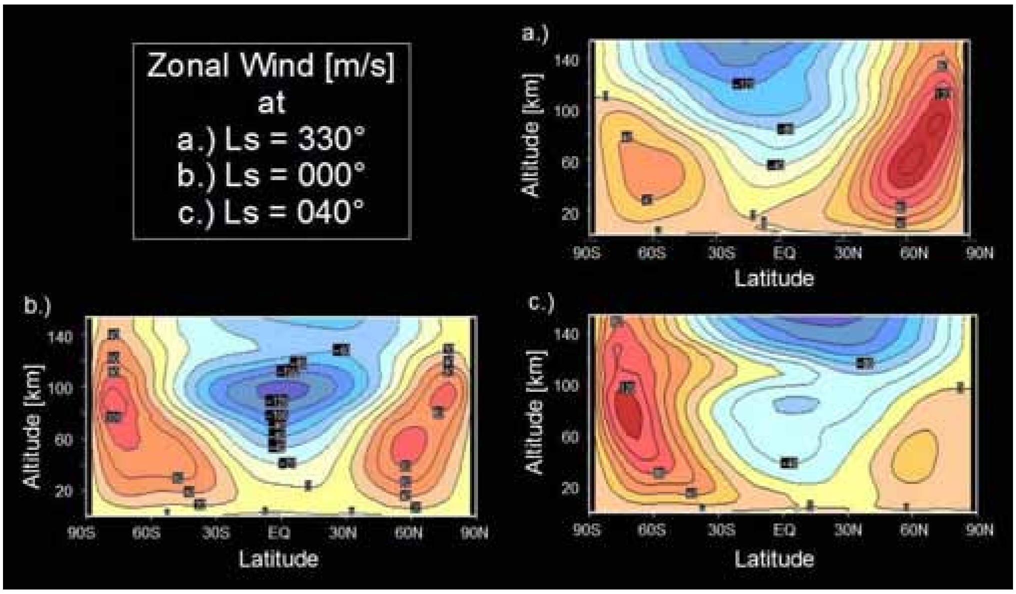

Figure 4.13: *Evolution of a mid to high-latitude jet over the range of a solar longitude of* L_s *=70 as predicted by Lewis et al. [95]. The upper left panel pictures the temperature at a solar longitude of* L_s *=330 (late northern hemisphere winter). A northern jet dominates at an altitude around 70 km. Later on this structure attenuates at* L_s *=0 (northern hemisphere spring equinox) as shown in the upper right panel. At a* L_s *=40 (late northern Spring) the jet dominates in the South. The lower panel shows the appearance of this southern jet.*

vations at different Martian seasons were accomplished. Mars opposition occurs when Earth, on its inner orbit, passes between the Sun and Mars. Due to the orbits of the two planets, this happens every 26 months.

At this time Mars has its maximum apparent diameter. Therefore, observation runs shortly before and after opposition are favorable for our mid-IR heterodyne technique since we also need a suitable Doppler shift between the planets to separate Martian CO_2 lines from their telluric counterparts. After the first observations in December 2005 ($L_s \sim 335$) the next posibilty to observe Mars was December 2007 ($L_s \sim 354$). An additional third observing run in March 2008 ($L_s \sim 41$) completed this data set. Observations, results and comparison with other measurements and models are presented in the following chapter. Due to convenient data availability the Martian Climate Database (MCD) was choosen [98] for model comparison. The MCD is based on a model developed at the Laboratoire de Météorologie Dynamique du CNRS(Paris) in collaboration with the University of Oxford, the Instituto de Astrofisica de Andalucia and with support from the European Space Agency and the Centre National d'Etudes Spatiales.

4.2.1 Observing Conditions: Mars

In 2003 the spectrometer THIS was used at the 1.5 m McMath-Pierce telescope of the National Solar Observatory on Kitt Peak, Arizona/USA to determine ozone abundances in the Martian atmosphere. During this run an initial measurement of CO_2 absorption and non-LTE emission at 10μm was performed to show the capability of the system to measure wind velocities. The observation was successful and later published in Sonnabend et al. [80]. A single point wind velocity measurement with THIS of 74 ± 22 m/s at 20°N was presented. This was the base for further investigations and the systematic wind velocity observations accomplished within this work. In total three observing runs addressing dynamics on Mars where performed. The first two took place at the McMath-Pierce Solar Telescope on Kitt Peak in December 2005 and November 2007. For the third observation we used the NASA Infrared Telescope Facility (IRTF) on Mauna Kea. This was also a technical challenge to the stability of the instrument since the instrument was mounted at a moving Cassegrain focus for the first time.

Mars Campaign A (Kitt Peak, December 2005)

On December 5 to 8, 2005 we observed Mars at the CO_2 P(2) transition at 959.3917 cm^{-1} using the McMath-Pierce Solar Telescope on Kitt Peak. The instrument THIS was mounted on the spectrograph table at the primary focus of the telescope. The total atmospheric and instrumental transmission was determined to be ~70%.

The angular diameter of Mars varied from 16.7 to 15.4 arcsec over the course of the observing period compared to the diffraction-limited FOV of the telescope of 1.7 arcsec. The pointing uncertainty was estimated to be below $\sim$1 arcsec. Mars was one month past opposition and the Earth-Mars Doppler shift varied between 9.8 and 11.4 km/s (receding) [94]. For Mars the acquisition time of $\sim$10 min for an individual spectrum is longer than for Venus due to the difference of the emission line intensities. The Doppler shift within this time period is < 18.5 m/s resulting in an acceptable line broadening of $\sim$ 1.8 MHz maximum.

Mars was illuminated 96 % with the subsolar point at $\sim$21 ° W of CML and $\sim$10.3 ° S from the equator. Martian season was late northern hemisphere winter at a Martian Solar Longitude of L_s $\sim$335.

In total, six different latitudes on Mars were observed during 102 single observations (consisting of one A and one B measurement), each lasting from 70 to 150 minutes. The sampled latitudes ranged from 45° North to 75° South and observations were carried out close to the limb covering a local time range of $\sim$3 h. Observing geometry is pictured in Fig. 4.14 indicating the observed positions at the FOV scaled to the planetary diameter. Observed positions are given in Tab. 4.7 giving dates, times and integration times.

Table 4.7: *Overview of the observed positions on Mars during the Mars campaign A at the McMath-Pierce Solar Telescope on Kitt Peak. Given are the position on Mars, observing dates, Martian season and local time, the quantity of included measurements (#), the scan numbers and the total integration time in minutes.*

Mars Campaign A (Kitt Peak, December 2005)

	lat./long.	date	start [UT]	end [UT]	season [Ls]	# meas.	ident. scan	int.time [min]
1	45 ° N/limb	12/05	3:07	5:40	335	16	(8-23)	320
2	0 ° /limb	12/05	1:42	2:51	335	8	(0-7)	160
3	0 ° /limb	12/05	5:23	8:42	335	20	(21-40)	400
4	15 ° S/limb	12/07	6:28	8:22	336	16	(28-43)	320
5	35 ° S/limb	12/08	1:00	3:00	338	10	(0-9)	200
6	60 ° S/limb	12/07	1:29	3:48	336	14	(0-13)	280
7	75 ° S/limb	12/06	1:00	9:33	336	16	(0-15)	320
8	75 ° S/limb	12/06	6:07	8:40	336	12	(27-46)	400

A sample spectrum is shown in Fig. 4.15. The signal-to-noise ratio (SNR) depends mainly on integration time and the surface temperature at the observed position on Mars which provides the quasi-blackbody contin-

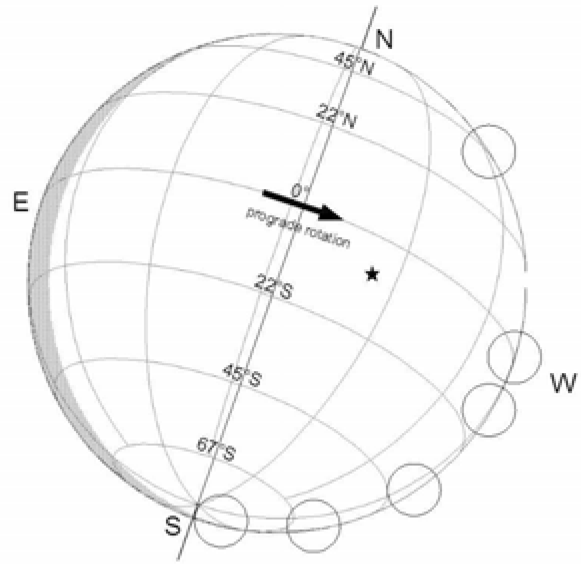

Figure 4.14: *Observing geometry of Mars during the Mars campaign A from December 5-8, 2005. The relative sizes of apparent diameter of the Martian disk (approximately 16 arcsec) and the FOV (1.7 arcsec) are indicated. Mars was almost totally illuminated (96 %) with a subsolar point at $\sim 21°$ W from CML and $\sim 10.3°$ S from the equator labeled by the black star. From limb observations line-of-sight velocities were retrieved for 6 different latitudes.*

uum level observed in the spectra.

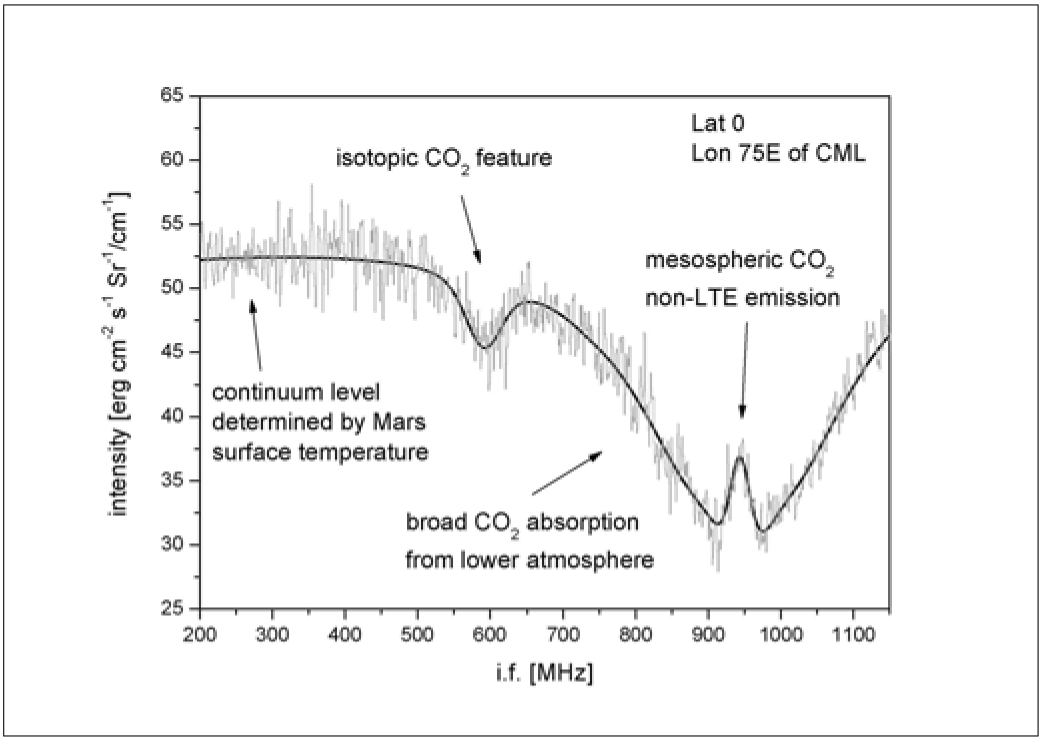

Figure 4.15: *Measured sample spectrum (grey) for Mars observations during campaign A taken at the equator and 75° East of CML demonstrating the structure of the spectra with a spectral resolution of 1 MHz. The black line gives the best fit to data.*

Mars Campaign B (Kitt Peak, November/December 2007)

To meet the requirements concerning Martian seasonal coverage the following observations were carried out and a solar longitude of $L_2 \sim 354$ between November 23 to December 3, 2007 again at the McMath-Pierce Telescope. The orbital position of Mars was approximately one month before opposition (date of opposition: December 24). The topocentric relative velocity between Earth and Mars varied between 4.9 and 7.8 km/s (approaching) [94]. Acquisition time for an individual spectra is again ~ 10 min with a variation in topocentric relative Earth-Mars Doppler shift of < 18.5 m/s.

Mars was almost fully illuminated with a subsolar point at $\sim 23°$ E from CML and $\sim 2.5°$ S. The apparent diameter was in the range between 14.4 and 15.3 arcsec similar to conditions for the observing run in 2005. The observing geometry is given in Fig. 4.16 and the relative size of the apparent diameter of the planet and the diffraction-limited FOV of $\sim$1.7 arcsec are pictured.

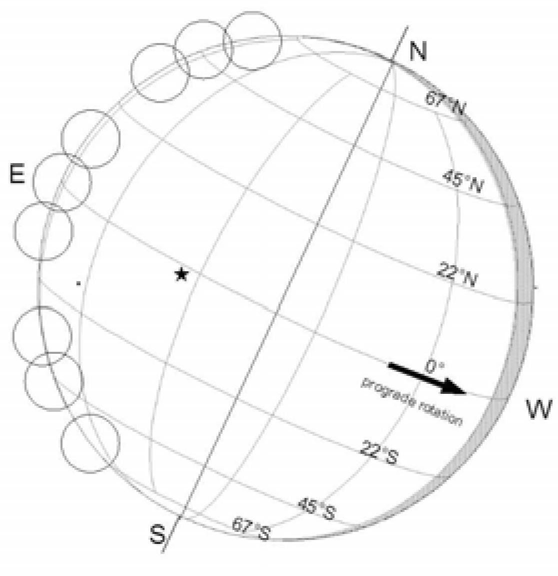

Figure 4.16: *Observing geometry of Mars during campaign B in November 23 and December 03, 2007. The field of view was $\sim$1.7 arcsec and the angular diameter of the Martian disk was $\sim$15 arcsec. Mars was almost totally illuminated and the black star marks the subsolar point at $\sim 23°$ E from CML and $\sim 2.5°$ S. Limb observations were accomplished at 9 different latitudes from 60° S to 57° N to retrieve line-of-sight velocities.*

74 single measurements (consisting of one A and one B measurement) provided data at 9 different latitudes on the planet (from 60 ° S to 57 ° N) along the morning limb. Relevant data for observations are summarized in Table 4.8.

Table 4.8: *Overview of the observed positions on Mars during the Mars campaign B at the McMath-Pierce Solar Telescope on Kitt Peak. Given are the observed position on Mars, observing dates and time, Martian season, the quantity of included single measurements (#), the identifiers of included scans (ident.) and the total integration time in minutes.*

Mars Campaign B (Kitt Peak, November/December 2007)

	lat./long.	date	start [UT]	end [UT]	season [Ls]	# meas.	ident. scan	int.time [min]
1	57 ° N/limb	11/27	11:20	11:47	354	1	(38-41)	20
2	45 ° N/limb	11/28	9:25	13:51	354	8	(18-34)	160
3	33 ° N/limb	12/03	10:30	12:07	357	5	(34-44)	100
4	11 ° N/limb	11/27	9:31	11:03	354	9	(20-37)	180
5	0 ° /limb	11/28	6:27	9:08	354	7	(0,1,3,4) (6-13) (16,17)	140
6	11 ° S/limb	11/24	9:00	14:12	352	12	(0,2,4,5,7) (9-12) (15-30)	240
7	33 ° S/limb	11/25	5:48	7:45	353	7	0-13	140
8	45 ° S/limb	11/23	9:05	11:14	352	8	(17-32)	160
9	45 ° S/limb	12/03	12:16	14:01	357	6	(45-56)	120
10	60 ° S/limb	11/25	9:36	11:14	353	6	(16-27)	120

On Mars the relative shift from the CO_2 absorption line originating at lower altitudes in the atmosphere to the non-LTE emission line from the upper atmosphere gives directly the wind shear between these two altitude regions. This technique was used for Mars in 2005 since a calibration gas cell to provide absolute frequency calibration was not implemented to the instrument then. This only became essential for Venus observations since the absorption feature on Venus is too broad and shallow to be useful due to the denser atmosphere.

The absolute frequency calibration using ethylene gas now provides the absolute wind velocity in the high atmosphere of Mars and was used form 2007 on. Two ethylene absorption lines are present (at

959.4075 cm^{-1} and 959.3072 cm^{-1}) within the observed bandwidth. Appearing in the same sideband as the Martian CO_2 feature the line 959.4075 cm^{-1} is chosen for determination of the absolute frequency position of the CO_2 line.

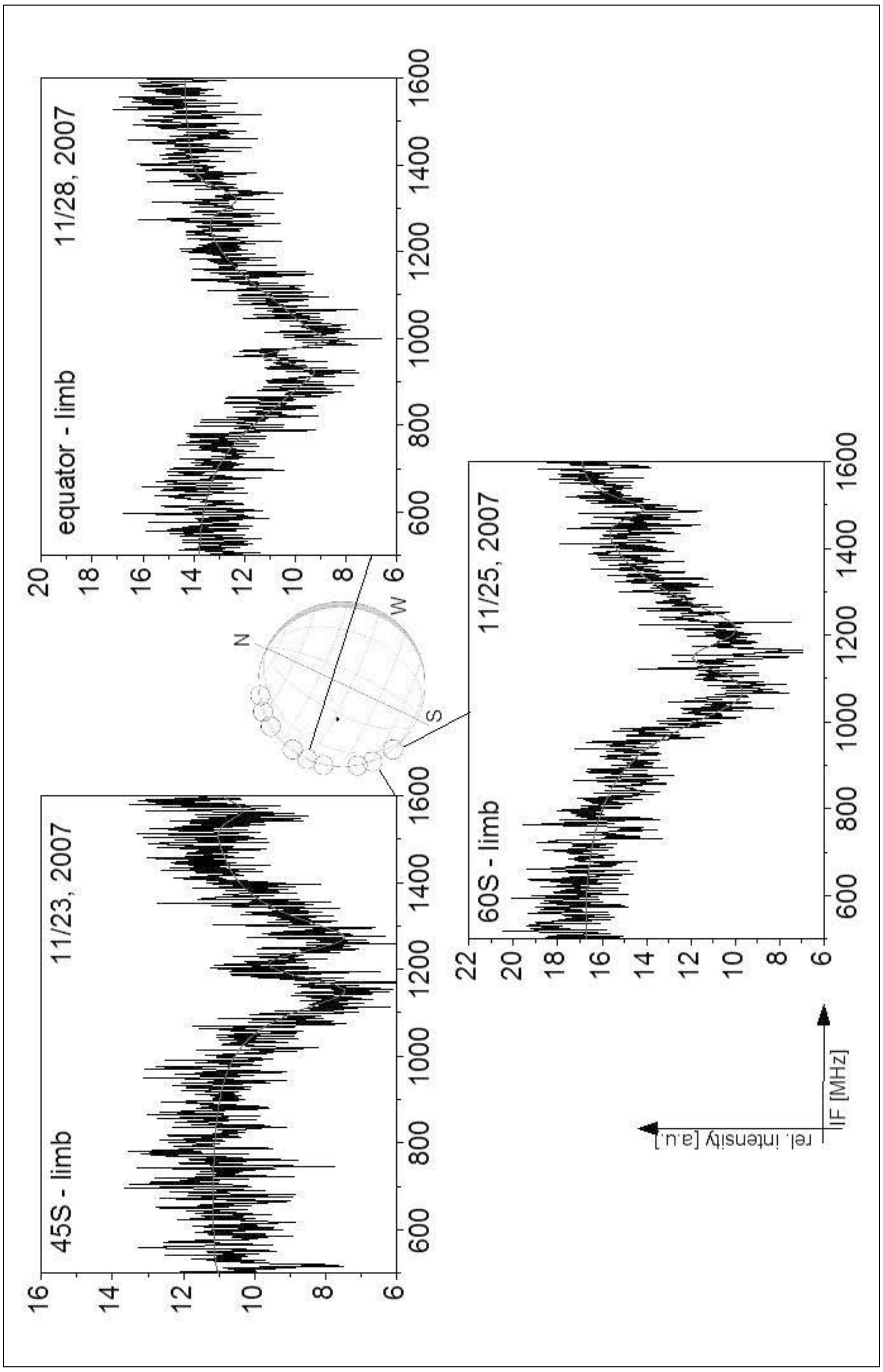

Figure 4.17: *Sample spectra with best fit taken during the Mars campaign B in November 23 and December 03, 2007. The spectral resolution is 1 MHz.*

Mars Campaign C (Mauna Kea, March 2008)

Before receding further away from Earth on its orbit around the Sun to meet Earth again only in 2009, Mars was observed again from March 03 to 06, 2008. Martian season at a solar longitude of $L_s \sim 42$ (northern hemisphere spring) completed the seasonal coverage to investigate the evolution of the jet shown in Fig. 4.13.

The apparent diameter of Mars varied between 8.6 and 8.9 arcsec. To obtain a spatial resolution similar to the observations in 2005 and 2007, when Martian apparent diameter was larger, we used the NASA IRTF on Mauna Kea in Hawaii, USA. The IRTF has a primary mirror of 3 m

Figure 4.18: *The NASA InfraRed Telescope Facility IRTF on Mauna Kea in Hawaii, USA with a 3.0 m mirror.*

diameter providing a diffraction-limited FOV at 10 μm of 0.8 arcsec.

The observing geometry is given in Fig. 4.19. The Martian disk was illuminated approximately 91 % with a subsolar point of 33 ° E from CML and 16° N. The topocentric relative velocity between Mars and Earth was $\sim$ 16.7 km/s [94].

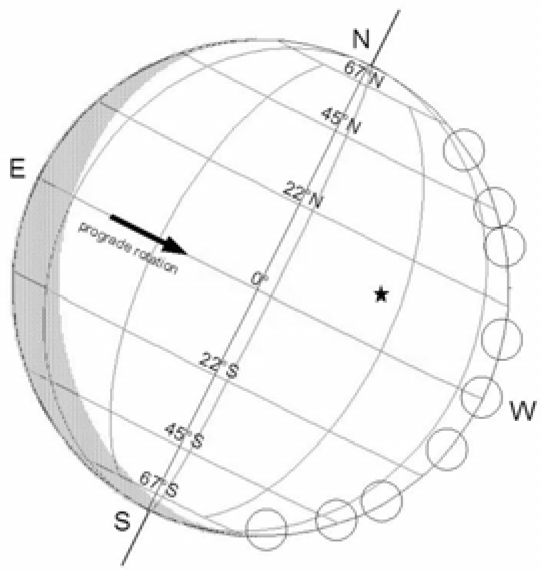

Figure 4.19: *Observing geometry for Mars Campaign C during March 03 to March 06, 2008. Like during the first two observation runs Mars was almost totally illuminated but this time the subsolar point at 33° E from CML and 16° N was close to the western limb. The FOV was 0.8 arcsec on an angular diameter of the Martian disk of ∼ 9 arcsec. 9 different latitudes were addressed for limb observations to gain line-of-sight wind velocities and one observation targeted the center of the planetary disk (CML/Equator).*

Limb observations at 9 different latitudes starting from 60 ° N to 60 ° S were performed. Observed positions and relevant observation parameters are summarized in Table 4.9. In total 35 single measurements (consisting of one A and one B spectrum) resulted in observations of 10 positions on the planet.

This time the P(4) line of CO_2 at 957.8005 cm^{-1} was observed. Two strong ethylene absorption lines from the implemented gas cell appeared within the detected bandwidth. Appearing in the upper side band, as well as the observed Martian CO_2 feature the 957.7641 cm^{-1} ethylene line was used for absolute frequency calibration.

Table 4.9: *Overview of the observed positions on Mars during the Mars Campaign C at the NASA IRTF on Mauna Kea in Hawaii, US. Given are the observed position on Mars, observing dates and time, Martian season, the quantity of included measurements (#), the identifier of included scans (ident.) and the total integration time in minutes.*

Mars Campaign C (Mauna Kea, March 2008)

	lat./long.	date	start [UT]	end [UT]	season [Ls]	# meas.	ident. scan	int.time [min]
1	60° N/limb	03/06	2:35	3:17	42	2	(0,2,3,6)	40
2	60° N/limb	03/06	7:40	8:17	42	3	(26-31)	60
3	45° N/limb	03/05	2:48	4:48	41	4	(6-8)	80
							(10,11)	
							(18-20)	
4	33° N/limb	03/06	4:28	5:23	42	4	(9-16)	80
5	15° N/limb	03/05	1:53	2:37	41	3	(0-5)	60
6	0° /limb	03/05	7:10	8:00	41	3	(36-41)	60
7	15° S/limb	03/05	8:08	9:01	41	3	(43-48)	60
8	33° S/limb	03/06	6:36	7:20	42	3	(20-25)	60
9	45° S/limb	03/05	4:57	6:50	41	7	(21-26)	140
							(28-35)	
10	60° S/limb	03/06	8:30	9:26	42	3	(32-37)	60

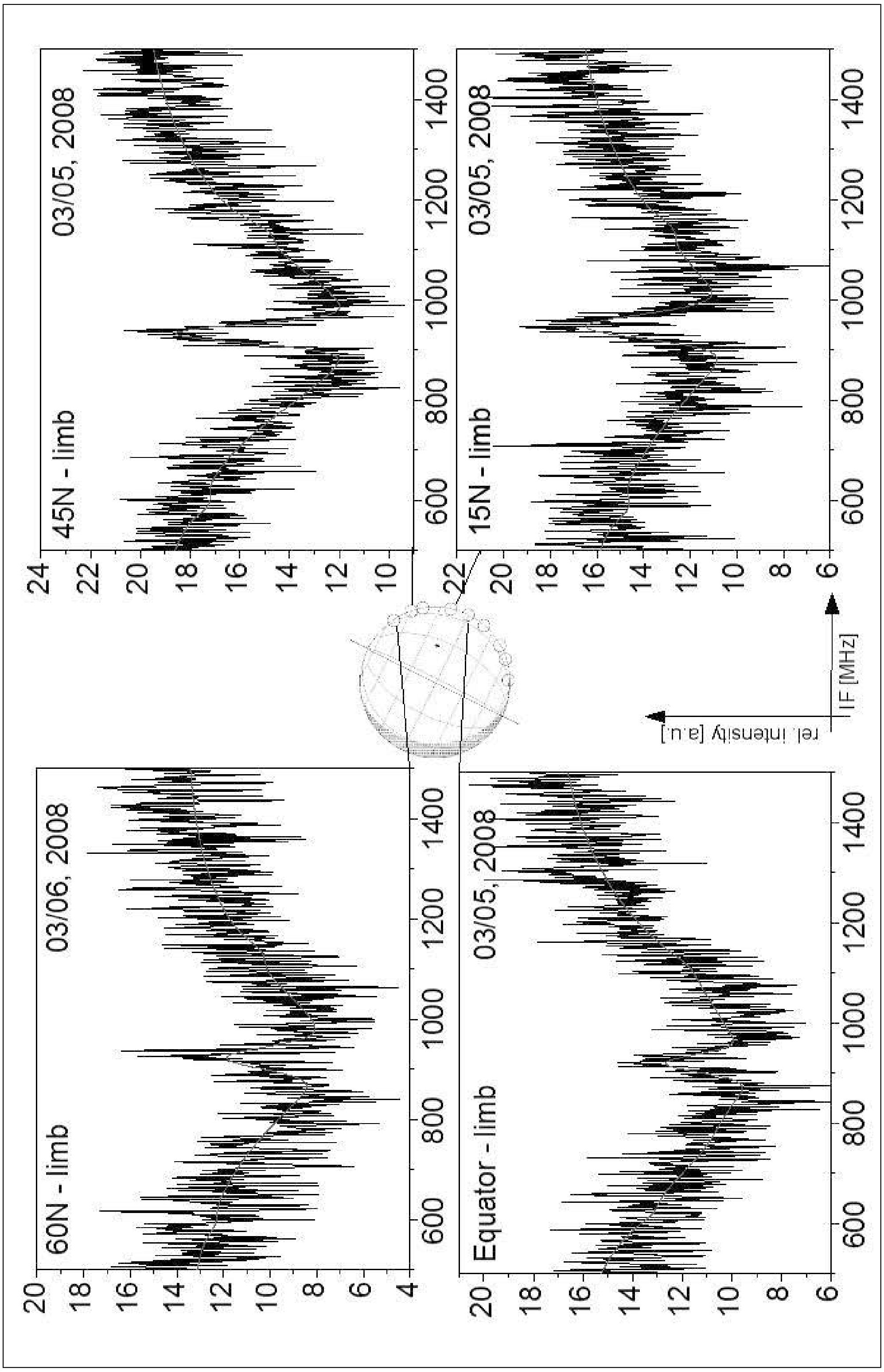

Figure 4.20: *Sample spectra with best fit taken at western limb from low to high latitudes during the observing campaign C at the NASA IRTF in March 2008. The spectral resolution of the measured data (black) is 1 MHz.*

4.2.2 Data Handling and Results of Mars Observations

During both observing runs on Kitt Peak the Martian P(2) line at 959.3917 cm^{-1} of the 10 μm-band was observed. Due to availability of a new QCL as LO the stronger P(4) line at 957.8005 cm^{-1} of the same band was observed during the observation run on Mauna Kea providing a higher SNR.

Measured single integrations were added to provide spectra with similar SNR. Integration time of the resulting spectra varied between 20-400 min depending on observing conditions (e.g. chosen position on Mars, weather, airmass).

The spectra were modeled and fitted with the BEAMINT radiative transfer code that was developed at NASA Goddard Space Flight Center [96]. BEAMINT combines a layer-by-layer radiative transfer modeling engine with an algorithm to combine the contribution from sub-resolution segments of the instrument beam to form the overall spectrum. This can be a noticeable improvement over a single point mean viewing angle model, especially when the viewing geometry is such that the beam sees contribution from a wide range of planetary longitudes. We used a 66-element model for the analysis of our observations. BEAMINT accepts planetary parameters, observation circumstances, molecular and thermal height profiles, and a molecular line atlas. The non-LTE component is not currently included in the radiative transfer code but added as a Gaussian profile describing the shape of the non-LTE emission. Parameters can be iterated until a best fit of a model spectrum to an observed spectrum is achieved. Uncertainties based on correlation between free parameters and the variance between the observed and model spectra are returned. The telluric contribution to the spectra was modeled using the terrestrial radiative transfer package GENLN2 [97]. For the presented results, Mars surface temperature, surface pressure, atmospheric thermal profile, and frequency position were iterated along with water abundance in the Earth's atmosphere and the total loss of signal due to misalignments etc. until the best fit to the observed data was reached. Initial parameters were taken from the "European Martian Climate Database" (MCD) [75], but were ultimately altered in the fitting process according to the fully resolved spectral line shapes.

Analysis methodology was different for the first observing run in 2005 and the following runs in 2007 and 2008 due to implementation of a gas cell for absolute frequency calibration into the instrument after the first run. The gas cell provides an absolute frequency calibration for the non-LTE emission relative to the gas cell spectrum and therefore information about the absolute wind velocity (independent from the absorption line). Without a gas cell the frequency shift between the Martian

CO_2 absorption and emission feature gives the wind velocity shear between high and low altitudes with the observing geometry taken into account. Analysis of the contribution functions plotted in Fig. 4.21 to the absorption line profile showed that most of the contribution to this line originates below the 3 mbar pressure level.

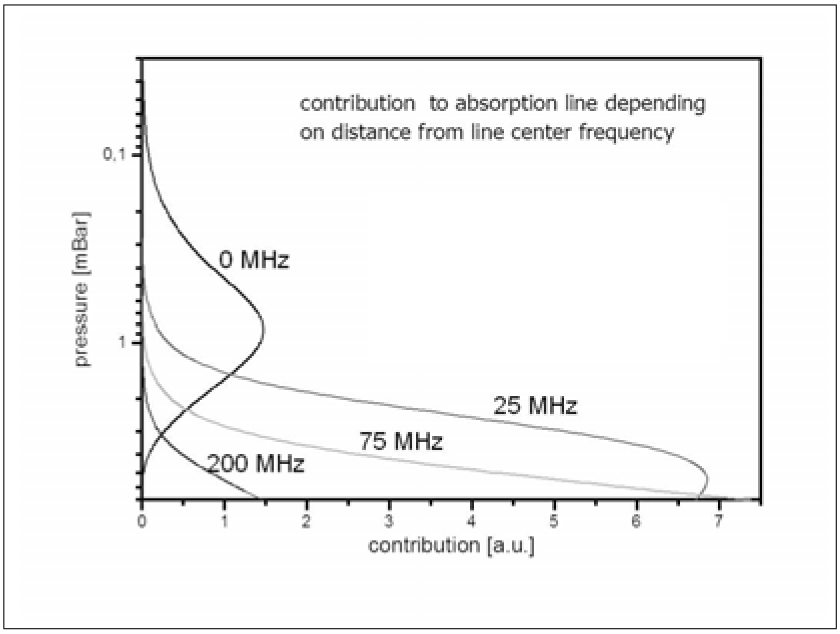

Figure 4.21: *Analysis of the contribution functions to the Martian* CO_2 *absorption line profile showed that most of the contribution to this line originates below the 3 mbar pressure level. The different lines indicate the contributions from the absorption line depending on distance form the line center.*

Wind velocities at the low altitudes are predicted to be low (in the range of few m/s). In both cases the fitted frequency offsets under assumption of the Mars solid-body rotation were then calculated and converted to beam-averaged line-of-sight wind velocities. Determination of the altitude of the emission-forming region presented a problem. Determination of the altitude via the temperature of the emitting material prooved to be unreliable since the temperature profile is variable. Therefore, we turned to observations by Maguire et al. [58] who determined the peak of the non-LTE emission from limb observations with the Thermal Emission Spectrometer (TES) on the Mars Global Surveyor (MGS) spacecraft to originate at ~65 km altitude, with the general range of the emission-forming region between 40 and 80 km altitude (see also Fig. 4.22). Investigation on altitude information of non-LTE emission lines on Venus will be extended to Mars as well (see chapter 5).

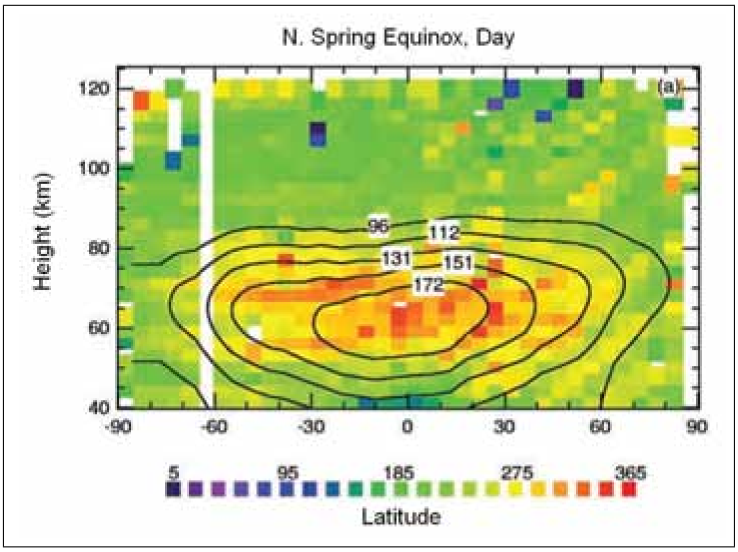

Figure 4.22: *Observed CO_2 hot band limb intensities at 10 μm at Martian northern spring equinox during day as seen by TES (Thermal Emission Spectrometer) on MGS (Mars Global Surveyor) published by Maguire et al. [58]. Radiance of the non-LTE emission is principally found in an altitude range between 40 and 80 km with an maximum at $\sim$65 km.*

An overview of the retrieved zonal wind velocities is presented in the Tab. 4.10, 4.11 and 4.12 below.

Table 4.10: Overview of the retrieved wind velocities in the mesosphere of Mars during the observing campaign A. Given are the position on the planet, date and the total integration time of observation. The given frequency shift is the relative shift ν_{los} between absorption and emission line hence the given line-of-sight wind velocity v_{los} is the wind shear between the low and upper atmosphere. Martian season was $L_s \sim 337$.

Mars Campaign A (Kitt Peak, December 2005)

	lat/long	date	t_{int}[min]	ν_{los}[m/s]	v_{los}[m/s]
1	45° N/limb	12/05	320	-2.2±1.4	-27±17
2	0° /limb	12/05	160	-6.8±1.1	-80±13
3	0° /limb	12/05	400	-4.5±0.9	-53±10
4	15° S/limb	12/07	320	-3.0±1.6	-35±19
5	35° S/limb	12/08	200	0.1±1.0	1±12
6	60° S/limb	12/07	280	2.2±1.1	25±12
7	75° S/limb	12/06	320	2.1±1.6	25±19
8	75° S/limb	12/06	400	4.1±2.4	51±29

Table 4.11: Overview of the retrieved wind velocities in the mesosphere of Mars during the Mars campaign B in 2007. Given are the position on the planet, date and the total integration time of observation. The absolute frequency shifts ν_{los} and line-of-sight wind velocity v_{los} are given as well. Martian season was $L_s \sim 354$.

Mars Campaign B (Kitt Peak, November and December 2007)

	lat/long	date	t_{int}[min]	ν_{los}[m/s]	v_{los}[m/s]
1	57° N/limb	11/27	20	15.4±6.0	148±58
2	45° N/limb	11/28	160	5.29±2.7	51±26
3	33° N/limb	12/03	100	-3.3±1.9	32±18
4	11° N/limb	11/28	180	0.5±1.1	5±11
5	0° /limb	11/28	140	-5.3±1.6	-51±15
6	11° S/limb	11/25	240	-4.1±1.7	-39±16
7	33° S/limb	11/25	2140	-10.4±1.5	-100±14
8	45° S/limb	11/23	160	-2.9±1.1	-28±13
9	45° S/limb	12/03	120	0.1±2.3	1±22
10	60° S/limb	11/25	120	11.1±3.1	107±30

Table 4.12: Overview of the retrieved wind velocities in the mesosphere of Mars during the Mars campaign C in 2008. Given are the position on the planet, date and the total integration time of observation. The absolute frequency shifts ν_{los} and absolute line-of-sight wind velocities v_{los} are given. Martian season was $L_s \sim 42$.

Mars Campaign C (Mauna Kea, March 2008)

	lat/long	date	t_{int}[min]	ν_{los}[m/s]	v_{los}[m/s]
1	60° N/limb	03/06	60	-11.2±2.4	107±23
2	60° N/limb	03/06	40	-3.3±1.3	32±12
3	45° N/limb	03/05	80	-1.9±1.1	18±11
4	33° N/limb	03/06	80	-1.3±1.3	13±12
5	15° N/limb	03/05	60	4.7±1.2	-45±12
6	0° /limb	03/05	60	8.5±2.3	-82±22
7	15° S/limb	03/05	60	23.8±2.4	-228±23
8	33° S/limb	03/06	60	14.4±1.0	-138±10
9	45° S/limb	03/05	140	12.5±2.4	-120±23
10	60° S/limb	03/06	60	12.6±4.7	-121±45

4.2.3 Mars Observations - Data Interpretation and Comparison to Model Prediction and other Observing Techniques

All observations during the first Mars campaign A in 2005 were performed near the western (evening) limb of Mars, fixing the local time of an observation at a given latitude. The 1 - σ retrieval errors range from 10 to 30 m/s mostly depending on the SNR of the data. We observed retrograde winds of - 27 $\pm$ 17 m/s in the northern hemisphere that were particularly strong (up to - 80 $\pm$ 13 m/s) in the equatorial region. In the southern hemisphere the mesospheric winds are still retrograde (- 36 $\pm$ 19 m/s) at low latitudes whereas at high latitudes it turns prograde to velocities between 25 $\pm$ 12 m/s and 50 $\pm$ 29 m/s. The increase by a factor of two within only a few hours later is surprising but not inconsistent with model predictions retrieved from [75].

As mentioned above, the origin of the non-LTE emission is assumed to be 50–90 km altitude, and all wind velocities (probed by the CO_2 emission feature) are retrieved relative to surface winds (probed by the CO_2 absorption feature). The presented results are consistent with the single point observation in 2003 where a strong retrograde wind of - 74 $\pm$ 22 m/s in the northern hemisphere was found [80].

A comparison of the measured data with zonal wind velocities predictions from the Martian Climate Database (MCD) [98] shows that the general latitudinal trend from 45 ° N to 75 ° S of the data is reproduced (see Fig. 4.23). The model was averaged over all longitudes, over altitude region between 50 and 92 km for the emission line and over a height between ground and 8 km for the absorption line. The results for the wind shear between the two altitude regimes are plotted in Fig. 4.23.

At the equator two observations at different MUTs (Martian Universal Time) were collected hence a more detailed comparison to the MCD is possible. The model predicts a lower zonal wind velocity at MUT 10 than at MUT 5. From the MCD database values of 62 m/s at MUT=10 and 80 m/s at MUT=5 were found [75]. The measured zonal wind velocities show the same behavior with values of 53 $\pm$ 10 m/s at MUT=10 and 80 $\pm$ 13 m/s at MUT=5 in agreement with the model within 1 - σ errors (see also Fig. 4.24).

Observations such as these provide a good general test of GCM predictions in altitude regions not well constrained by other measurement techniques. Additionally the comparison concerning different MUTs demonstrates nicely that also validation of short temporal variations of these models is possible by mid-IR heterodyne wind observations.

During Mars campaign B absolute wind velocities were retrieved. Retrograde winds of -51 $\pm$ 15 m/s were found at the equator as well as an

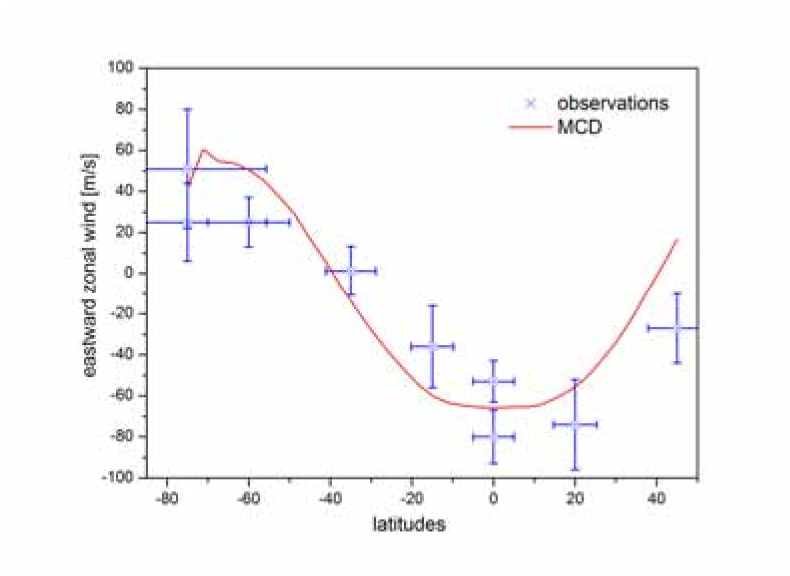

Figure 4.23: *Comparison of retrieved zonal wind shear between the ground to 8 km and from 50 to 92 km from observed data during the Mars campaign A in 2005 with the MCD [98]. The model data is averaged over all MUTs, a season from $L_s = 330$ to $L_s = 360$ and a height from 50 to 92 km.*

increase towards northern and southern latitudes. At 45 ° S values of -28 ± 13 m/s and 1 ± 22 m/s were observed whereas a stronger increase of 51 ± 26 m/s was seen in the northern hemisphere at 45 ° N. The same behavior is also evident at higher latitudes with values of 107 ± 30 m/s 60 ° S and 148 ± 58 m/s 57 ° N.

These results are in general agreement with the model. Values at high latitudes (57 ° North and 60 ° South) tend to be higher (by approximately 50 m/s) than predicted velocities as well as the value at 11 ° N. Whereas the measured wind at 33 ° S of 100 ± 14 m/s is significantly lower than the model result of 23 m/s. The given model results are averaged with respect to location, altitude and most relevant the averaging regarding Martian season from L_s=330 to 360. Hence variations within these value ranges are not represented by the given model results and can be the reason for the disagreements.

At least for one latitude (45 ° S) two observations at different MUTs were carried out. In one case the measured wind velocities of - 28 ± 13 m/s is lower than the averaged model prediction. In the other case the measured value of 1 ± 22 m/s agrees with the model within the error bars. A more detailed comparison concerning variations with MUT is pictured in Fig. 4.26. The figure shows that, like in the measurements there is no significant variation in wind velocity between the two MUTs up to an

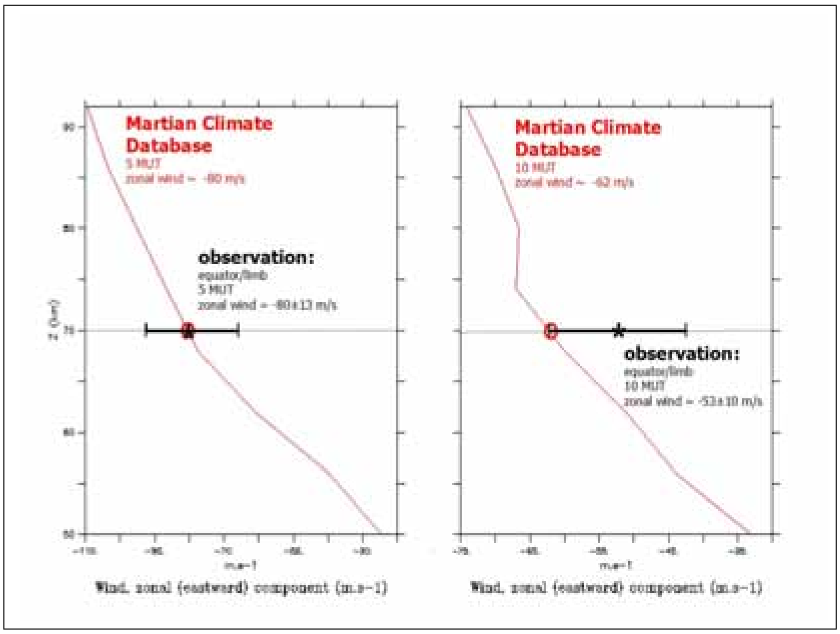

Figure 4.24: *Comparison of retrieved zonal wind shear between the ground to 8 km and from 50 to 92 km from observed data during the Mars campaign A in 2005 with the MCD [98] at Martian Universal Time (MUT) of 5 and 10.*

altitude of 80 km in the model. The disagreement between model and observation values can not be explained by averaging effects over MUT of the model.

In contrary to previous observations where a similar behavior in the northern and southern hemisphere was found a significant asymmetry is observed during the last Mars campaign C at the IRTF in 2008. At the equator a moderate redrograde wind of -82 ± 22 m/s changes into strong prograde wind of 107 ± 23 m/s towards high northern latitudes. Completely different strong retrograde winds up to - 228 ± 23 m/s are found in the southern hemisphere.

A comparison to the MCD is shown in Fig. 4.27, where the measured wind velocities follow the model predictions nicely in the northern hemisphere. The southern hemisphere observations diverge significantly not only from previous measurements but also from the model. In general wind velocities are found to be lower and values down to approximately -230 m/s are not explainable by any atmospherical processes in the Martian atmosphere.

Since the spectrometer THIS was used for the first time at a Cassegrain focus and hence moving during observations, high demands regarding the stability of the instrument were requested.

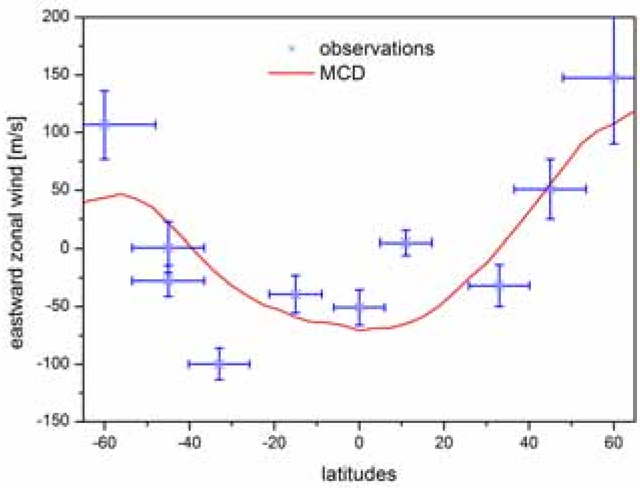

Figure 4.25: *Comparison of retrieved zonal wind velocities from observed data during the Mars campaign B in 2007 with the MCD [98]. The model data is averaged over all MUTs, a season from $L_s = 330$ to $L_s = 360$ and a height from 50 to 92 km.*

Although we frequently verified the beam path through the spectrometer during observations an offset between the assumed position and the actually observed position on Mars seems a reasonable suspicion to explain the unfeasible retrieved values. We found that all observations from the southern hemisphere have been accomplished past Mars transit. Observations in the North were made before transit with one exception at 60° N having a relatively low value of 32 ± 12 m/s compared to the pre-transit value of 107 ± 23 m/s.

Due to the mechanical circumstances at the Cassegrain focus of the IRTF the spectrometer is "flipped over" during transit of Mars. Hence it is conceivable that a misalignment between the optical and IR beam path occurred after transit. The most likely reason is a slight displacement of the optical camera resulting in an East-West offset of the observations on the planet. Offsets of various magnitudes were assumed and projection effects on the resulting wind velocities were calculated. The results for a beam offset of 1.4 arcsec (approximately two beam diameters) towards the Eastern limb is plotted in Fig. 4.28 moving the observed wind velocities close to the model values.

The measurements from the southern hemisphere can not be used for model validation or comparison with other measurements. Consequently investigations on the assembly and mounting of the guiding system are necessary and a continuous verification of both beam paths especially before and after transit is unavoidable for future observations

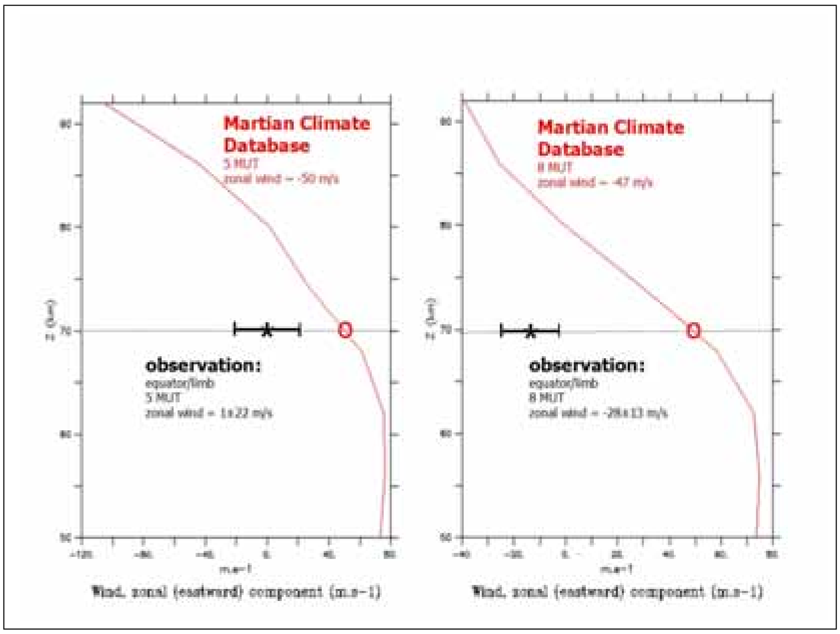

Figure 4.26: *Comparison of retrieved zonal wind velocities from observations carried out during the Mars campaign B in 2007 with predictions of the MCD [98] at Martian Universal Time (MUT) of 5 and 8.*

at telescopes with Cassegrain foci.

Finally only observations of zonal wind velocities from equator to a latitude of 60 ° N were used (see Fig. 4.29). Values from -82 ± 22 m/s at the equator to velocities of 107 ± 23 m/s increasing with latitude are found in good agreement with model predictions.

Apart from the problem of past transit measurements during the observing run in 2008 results of all three observing campaigns are in very good agreement with the model predictions. High latitude measurements at 60° North and South are found to be higher by approximately 50 m/s than model predictions for campaign B and C.

The displacement of a northern hemisphere yet at L_S=330 to the southern hemisphere at L_S=40 could not fully be validated due to missing observations at high latitudes. Like predicted a balanced situation in both hemispheres is found for L_S=354 as shown in Fig. 4.25. Unfortunately no data for the maximum jet velocity situation in both cases could be retrieved due to technical problems and observational constraints. However, the decreasing zonal wind velocities from the balanced situation to the season with a jet feature in the hemispheres of the disappearing jet indicate a general agreement with the model of Lewis et al. [95]. An overview of the evolution of high latitude zonal wind velocities with Martian season is given in the Table 4.13 below.

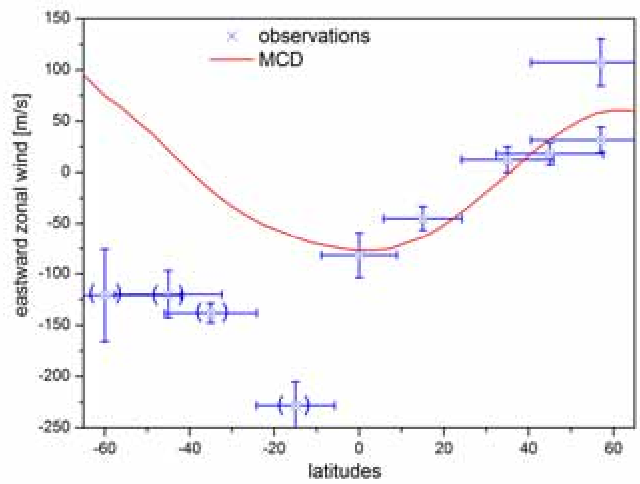

Figure 4.27: *Comparison of retrieved zonal wind velocities from observed data during the Mars campaign C in 2008 with the MCD [98]. The model data is averaged over all MUTs, a season from over $L_s = 0$ to $L_s = 30$ and a height from 50 to 92 km. Data values in parenthesis diverge significantly form the model results and, as described below, the disagreement is most likely due to instrumental misalignment during observation.*

Additional earth-based wind measurements have mainly been carried out by millimeter observations of CO probing an altitude between 35–80 km with a much lower spatial resolution than mid-IR heterodyne observations. Even interferometric observations only allowed 4x4 independent points on Mars [77]. Strong retrograde winds between 100 and 200 m/s are found at the western equator [77] and in the southern hemisphere [78, 79] (see also Tab. 4.14). Unfortunately Martian seasons of these observations are different to the presented observations within this work and therefore a detailed comparison is not possible.

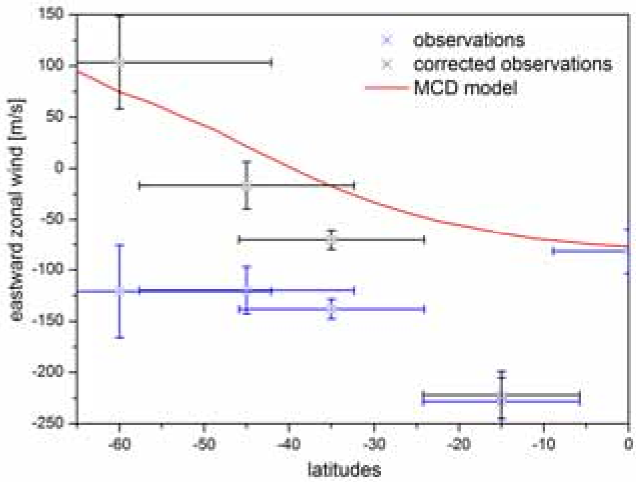

Figure 4.28: *Comparison of retrieved zonal wind velocities from observed data (blue) during the Mars campaign C in 2008 with the MCD [98] (red). Values in black show projection corrected values for observations at the southern hemisphere assuming a beam offset of two beam diameters towards East. The model data is averaged over all MUTs, a season from $L_s = 0$ to $L_s = 30$ and a height from 50 to 92 km.*

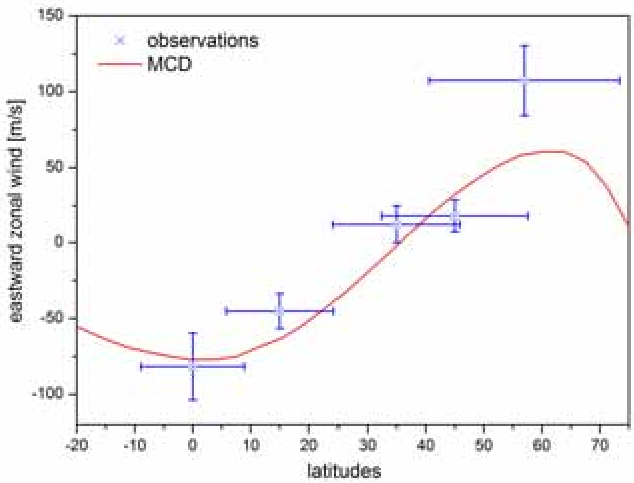

Figure 4.29: *Comparison of retrieved zonal wind velocities from data observed during the Mars campaign C in 2008 with the MCD [98]. The model data is averaged over all MUTs, a season from $L_s = 0$ to $L_s = 30$ and a height from 50 to 92 km.*

Table 4.13: Overview of zonal wind measurements at high latitudes to investigate the long term displacement of a high latitude yet in the North at a Martian season of L_s=332 to the South at a Martian season of L_s=42.

latitude	season	year of obs	wind velocity
60 ° N	335	2005	no data
60 ° N	354	2007	148±58
60 ° N	042	2008	107±23
60 ° S	335	2005	25±12
60 ° S	354	2007	107±30
60 ° S	042	2008	no data

Table 4.14: Overview of previous Martian Doppler wind observations

Transition	FOV [arcsec]	Mars [arcsec]	Lat. [°]	Alt. [km]	L_s	Wind [m/s]
CO_2 P(30)	2	11	20 ° N	60–80	308	-74 ± 22[1]
CO(2-1)	12	23.8	20 ° S	40–70	279	-160 ± 80[2]
CO(2-3)	13	25	20 ° S	35–80	251–254	-120– -200[3]
CO(1-0)(2-1)	5/8	9-23	° E0	45–69	140,196 262,317	-100 ± 20[4]

[1]Sonnabend et al. [80]
[2]Lellouch et al. [79]
[3]Clancy et al. [78]
[4]Moreno et al. [77]

Chapter 5

"Results! Why, man, I have gotten a lot of results. I know several thousand things that won't work." (Thomas A. Edison (1847-1931), US inventor)

Summary of Results and Outlook

Within this work it is demonstrated that infrared heterodyne spectroscopy is an excellent tool for direct measurements of high atmospheric winds on Mars and Venus by probing relative Doppler shifts of fully-resolved spectral features. The accuracy of the system THIS has proven to be sufficient to extend observation also to measurements of small scale variations within short time periods in the future.

In order to achieve a better comparison of the measured wind velocities to model predictions and other ground-based and space-based measurements, the altitude information about the origin of non-LTE emission has to be improved. Therefore determination of the emission-forming region directly from the observed spectra is a primary task for the future.

To investigate wind velocity and the nature of the non-LTE emission itself further observations for Mars and Venus are already planned on various CO_2 transitions. In addition observations of other molecules are planned as well as other planets (Saturn, Jupiter) and moons (Titan, Io) of our solar system. And even further away molecules in stars and stellar envelopes can be targets for the future.

A brief summary of the achieved results, future plans for instrument development and scientific applications is given in the following chapter.

5.1 Summary of Results

5.1.1 Wind Measurements on Venus

Model development for Venus upper atmosphere is still in progress and predictions are not reliable above 90 km yet. Hence no useful comparisons are possible. On the other hand coordinated observing campaigns opened the possibility to compare and to assemble data measured with other observing techniques. From May 23 to June 9, 2008 not only measurements with THIS but ground-based observations in the radio, submillimeter, infrared and visible wavelength region targeted the atmosphere of Venus with the main focus at the atmosphere region above Venus' cloud tops to support the spacecraft VEX.

The results achieved within this work are summarized in Fig. 5.1 and 5.2. So far comparison of the measured wind velocities with results from other observing techniques is only possible either probing the same altitude region observed at different times or observing at similar times with techniques probing other altitude region.

In general lower values of wind velocities than other measurements are found. The variation between the two observing runs was relatively moderate. Previous results of zonal wind velocities using also mid-IR heterodyne observations from 1990 and 1991 show insignificantly higher values [49, 45] with velocities in the range of a few tenth of m/s. From extrapolation of results from CO observation in the mm wavelength range Lellouch et al. [52] found even higher values for the same altitude range. These CO measurements probe an altitude region around 105 km and revealed recently [63] also high wind variability with time. An overview of ground-based measurements is pictured in Fig. 4.12 and summarized in Tab. 2.1 and 2.2.

As shown in chapter 4.1.3 the results for SS to AS flow in this work are comparable to other measurements [49, 45, 52] though observing geometry was not favorable for the extraction of the SS to AS flow.

In general the coordination of different ground-based observing techniques, revealed a much higher variability of dynamics in the Venusian atmosphere than thought before and the current picture of stable SS-AS flow and superrotation region is too simple. Many processes in the atmosphere of Venus are not yet fully understood and this is the motivation for scientists to continue with coordinated ground-based campaigns together with VEX observations. The next campaign is proposed for February 2009 and measurements with THIS are planned to contribute to investigations on Venusian dynamics and atmospheric variability.

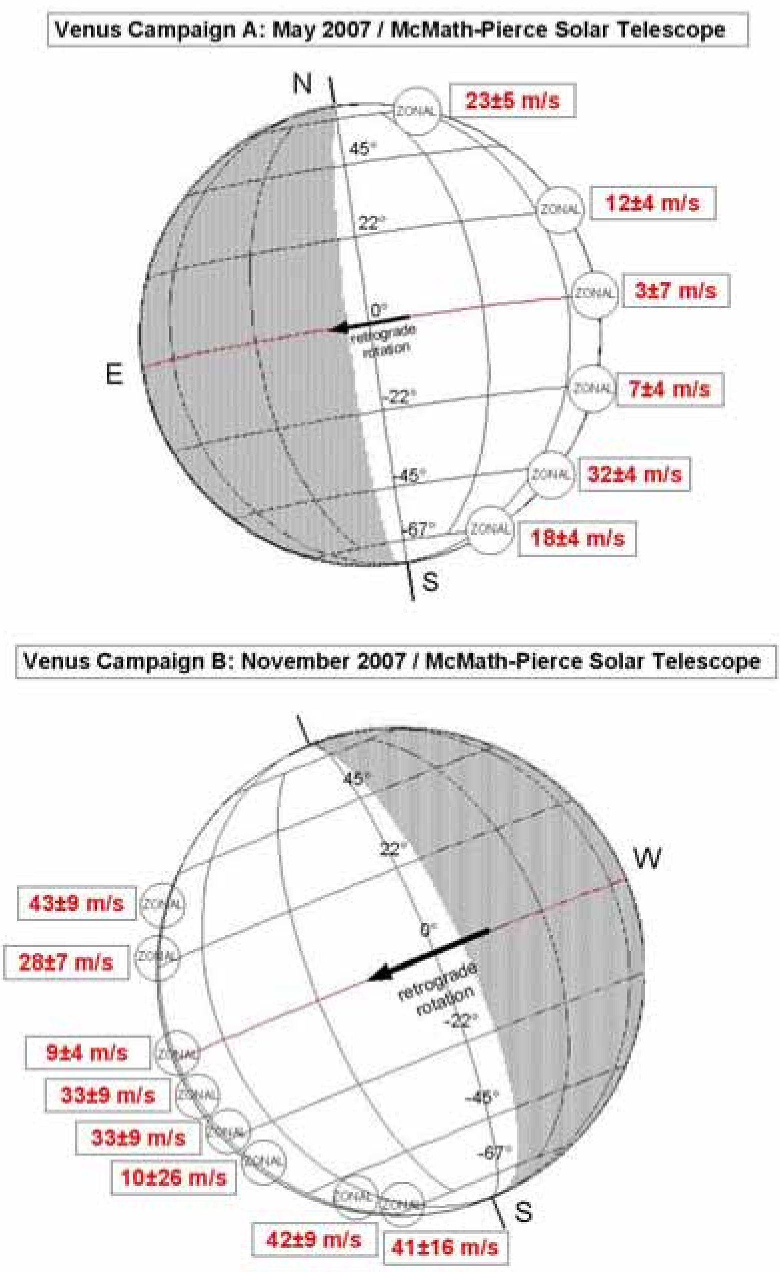

Figure 5.1: *Overview of retrieved results for zonal wind velocities for the indicated positions during the Venus campaigns A and B. Positive values give retrograde velocities, meaning rotation in the same direction as Venus solid body.*

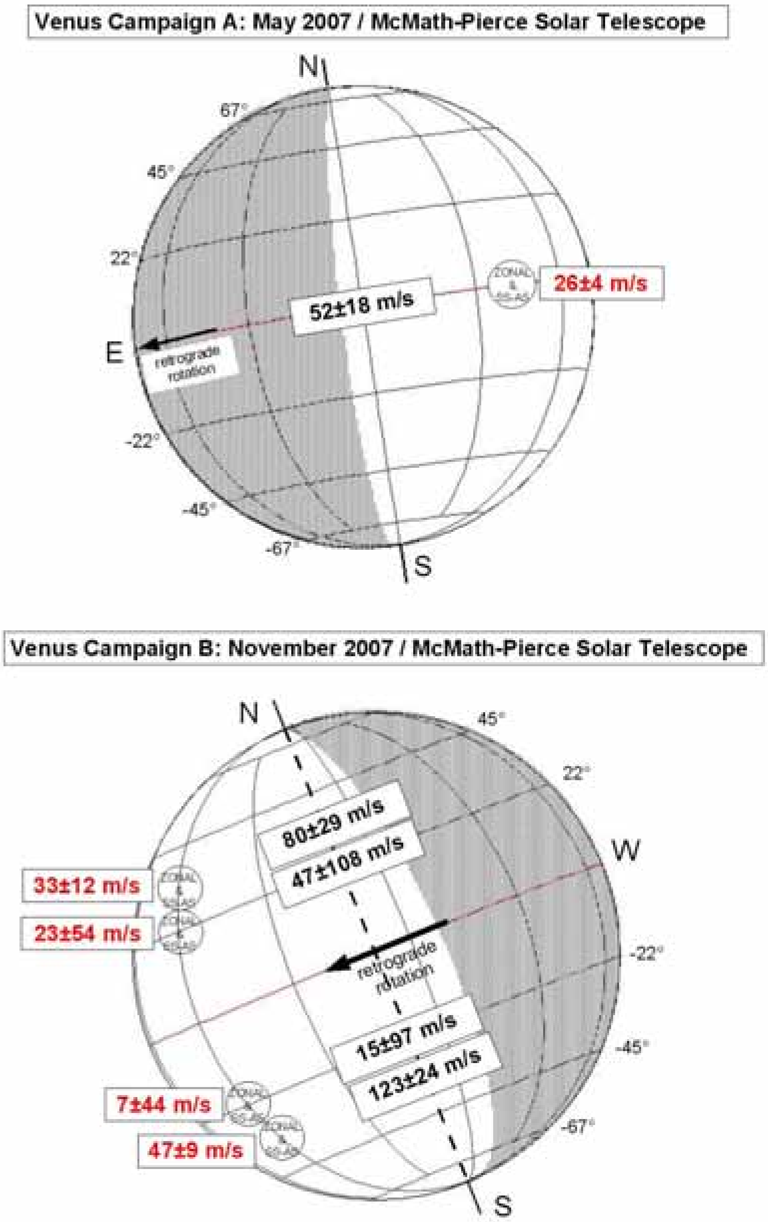

Figure 5.2: *Overview of results for the SS-AS flow on Venus retrieved during the Venus campaigns A and B. Quoted in red are SS-AS flow velocities along the trajectory from subsolar point to antisolar point at the given positions. Values given in black are the determined maximum cross terminator velocities retrieved from SS-AS flow velocities. A positive value indicates a flow direction from the SS point to the AS point.*

5.1.2 Wind Measurements on Mars

Fig. 5.3 summarizes all zonal wind velocities retrieved on Mars within three observing runs part of this work. The results are compared to the MCD model from Forget et al. [98] providing flexible availability of data through *http://johnson.lmd.jussieu.fr:8080/las/servlets/dataset*. In general all our observations could validate model predictions within 1 - σ errors. From 24 measured wind velocities during three observing runs only 6 measurements are found to diverge from model results. Three measurements are found to be higher (two at high latitudes during campaign B and C and one at 11 ° N during campaign B) and three position are found to have lower wind velocities (at latitude of 45 ° N (campaign A), 45 ° and 33 ° (campaign B)).

The disagreements might be due to averaging model predictions over season, longitudes and an altitude range. Especially comparison within small seasons ranges is not possible via the online database and future investigation directly with modelers are necessary.

Few comparisons with respect to various MUTs show that detailed comparisons are possible by heterodyne observations with THIS.

Like on Venus investigations on altitude information directly from the spectra is required hand in hand with detailed model comparison in respect of altitude. With that information the comparison can be extended to other GCMs [98, 95, 99, 100].

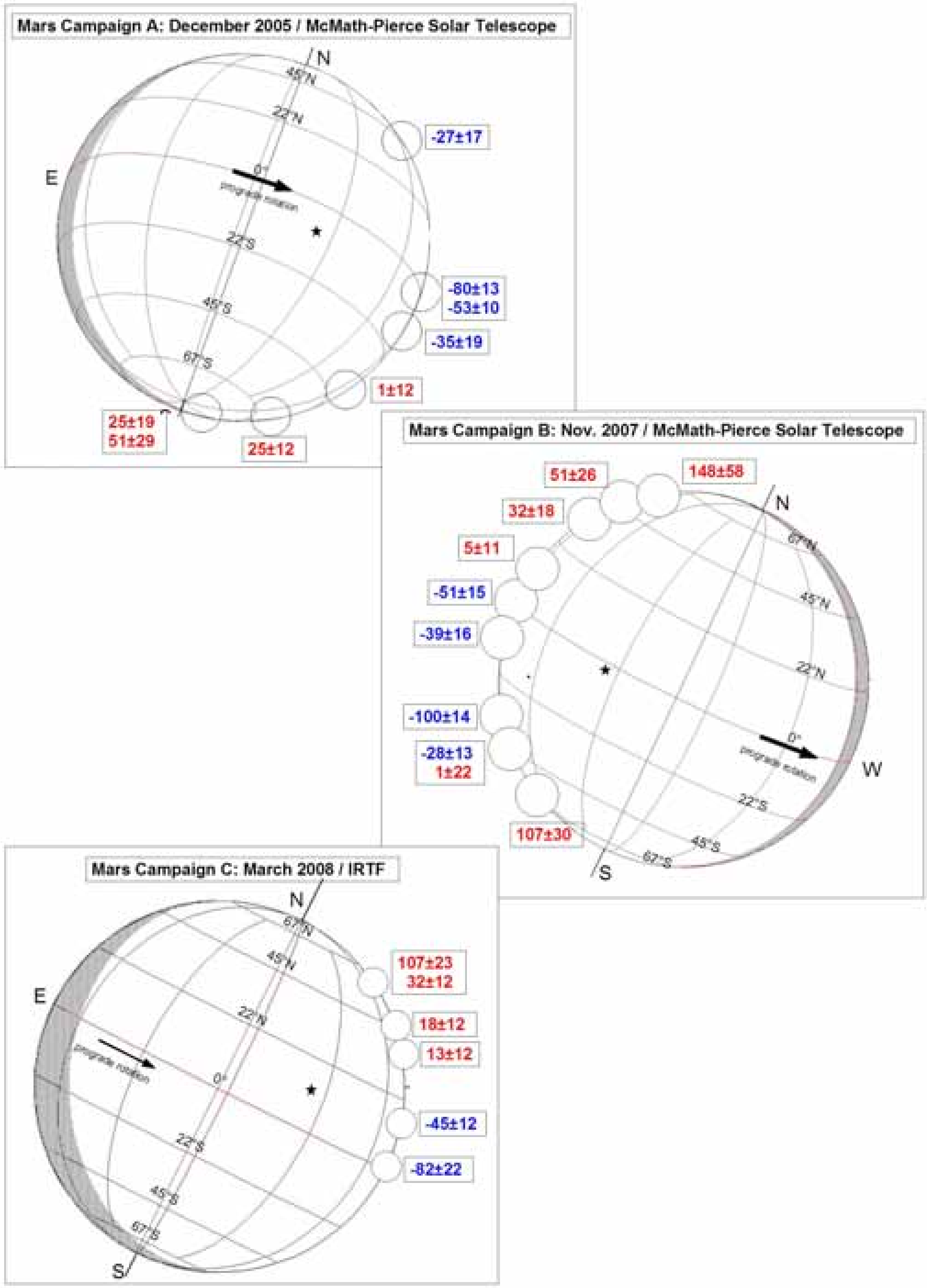

Figure 5.3: *Overview of retrieved results for zonal wind velocities on Mars during the three Mars campaigns A, B and C. Wind velocities are given in m/s, prograde wind velocities are written in red whereas blue numbers indicate retrograde wind velocities.*

5.2 Outlook Instrument

The observing run at the NASA IRTF has shown that moving the instrument with the telescope during observations, necessary on telescopes with Cassegrain focus, is on the edge of stability requirements for the instrument. Hence further investigations on the current setup are needed.

Another improvement concerns the necessary time for installation of the instrument at the telescope. The setup of THIS is already possible within a relatively short time of approximately one to two days with only two people. A further decrease of this time with increasing reliability would provide better convenience of operation and hence extended flexibility of the instrument.

As the sensitivity of heterodyne detection improves going to longer observing wavelength the implementation of LOs at longer wavelength is feasible and important to expand the field of suitable applications. In the 11-13 μm wavelength range such applications could include studying hydrocarbons in the outer planets or observations of atomic features in stellar atmospheres. Extension of the accessible wavelength range with THIS to 17 μm will allow observation of molecular hydrogen, the most abundant molecule in the universe. This involves investigation of 17 μm detector and laser devices provided by a collaboration with Jerome Faist and from the University of Neuchatel/Switzerland [101]. This is part of the current PhD work by Peter Kroetz within our group at the University of Cologne.

In addition an external cavity (EC) QCL system has been developed by Stupar [88],[89], allowing for the first time the use of multimode lasers as local oscillators. This system will tremendously improve the spectral coverage of the spectrometer THIS. While the individual singlemode devices used so far only cover a range of 3–5 cm^{-1} a multimode laser forced to singlemode operation using an external cavity can easily provide LO power over a range of tens of cm^{-1}. An EC will also allow observation of multiple transition lines in close temporal proximity, a mode of observation not yet possible with THIS. Another important advantage is that multimode lasers are far less expensive than singlemode devices. The current setup however cannot be used right away due to the lack of remote adjustments and mechanical and thermal stability. The needed performance will be established and verified for astronomical observations. Dušan Stupar, a PhD student within our group at the University of Cologne is currently working on this project.

A heterodyne system would also be applicable for interferometry. Several receivers would be needed including special requirements on phase locking of local oscillators and delay handling.

THIS is also planned to be a second generation instrument for the Stratospheric Observatory For Infrared Astronomy (SOFIA) providing a new field of scientific application due to better atmospheric conditions especially at longer wavelengths (see chapter 5.3.3). Beyond that a heterodyne system would also be feasible as spacecraft instrument providing high spatial resolution observations without any telluric disturbances.

As stated above several immediate tasks and long term developments are on the list for the heterodyne receiver THIS and depending on manpower and financial resources these projects will provide extension of present applications and open new fields of investigations as described below.

5.3 Outlook on Applications

5.3.1 Venus

Heterodyne spectroscopy of CO_2 at mid-infrared wavelengths is a powerful tool to study temperatures in the atmospheres of Venus. Modeling the process leading to the non-LTE emission [54, 56] is still mostly dependent on computational constraints, thus limiting the development of accurate complete models of the atmospheres of Venus. Possible differences between rotational, kinetic, and vibrational temperatures could provide important clues for understanding and modeling the non-LTE emission phenomenon. Kinetic temperatures can be calculated from the width of the lines. At the same time, rotational temperatures can be extracted from the distribution of line intensities for different rotational transitions in the 9.6 and 10.6 μm CO_2 bands. As long as stimulated emission is negligible kinetic linewidth and rotational distribution probe the physical temperature of the emitting gas as presented by Deming and Mumma [54] and Kaufl et al. [68]. Measurements were made by my colleague G. Sonnabend and me using the Heterodyne Instrument for Wind and Composition HIPWAC at the IRTF. HIPWAC is operated by a group around T. Kostiuk from the NASA Goddard Space Flight Center, Maryland, USA and results are published in Sonnabend et al. [82]. Additional measurements of rotational and kinetic temperatures on the dayside thermosphere and mesosphere of Venus will be useful for improving our understanding of the Venus thermal structure, non-LTE emission processes, and possible temporal and spatial variability.

Also trace constituents in the Venusian atmosphere are of interest. OCS e.g. has been identified as a potential tracer for the interaction between Venus lower and middle atmosphere. Current upper limits are higher than the proposed values by Mills [102]. Fully resolved ro-vibrational lines can give OCS abundances and can therefore help understanding this discrepancy.

5.3.2 Mars

In addition to wind information from frequency shifts, CO_2 features provide information about pressure near the surface on Mars due to the shape of the line wings of the absorption feature. This opens a possibility to measure low/high pressure wave patterns similar to weather systems on Earth.

Not only CO_2 but also molecules like O_3, CH_4, OCS, SO_2 or ClO show strong features in the mid-IR region and can provide information about atmospheric chemistry and biogenic processes. Analysis of line shapes of well-mixed species retrieves constraints on temperature profiles and photochemistry and temporal variations can be probed by the determination of abundances [103]. Many molecular species of interest are not only important in the Martian atmosphere but in all atmospheres of the terrestrial planets including Earth.

One specific opportunity of high spectral resolution of infrared heterodyne observations is the detection of Martian methane lines at 7.8 μm wavelength. This molecule came into focus due to implications for the possibility that microbial life could exist on Mars. High spectral resolution provides the possibility to unambiguously distinguish Martian and terrestrial absorption contributions during specific observing periods having a high Doppler-shift between Mars and Earth of $\geq$15 km/s resulting in a redshift of the Martian feature of $\sim$2.2 GHz. Abundances down to 10 ppb are detectable within $\sim$10 h of integration time with THIS including all losses introduced by optical and electronical components (see Fig. 5.4). Initial measurements at a promising line at 1277.4734 cm^{-1} were accomplished in March 2008 at NASA IRTF on Mauna Kea, Hawaii, USA, but results were limited by weather conditions. Nevertheless future measurements at suitable Doppler-shifts are planned.

5.3.3 Beyond Venus and Mars

Abundances of small hydrocarbons like CH_4, C_2H_2, C_2H_4 and C_2H_6 are of general interest in the atmospheres of the outer planets.

Observations of ethane e.g. have been already used to study conditions in the auroral region on Jupiter. Although Jupiter's magnetosphere has been thought to isolate it from the effects of the 11-year solar cycle variations, long-term observations of stratospheric auroral ethane emission

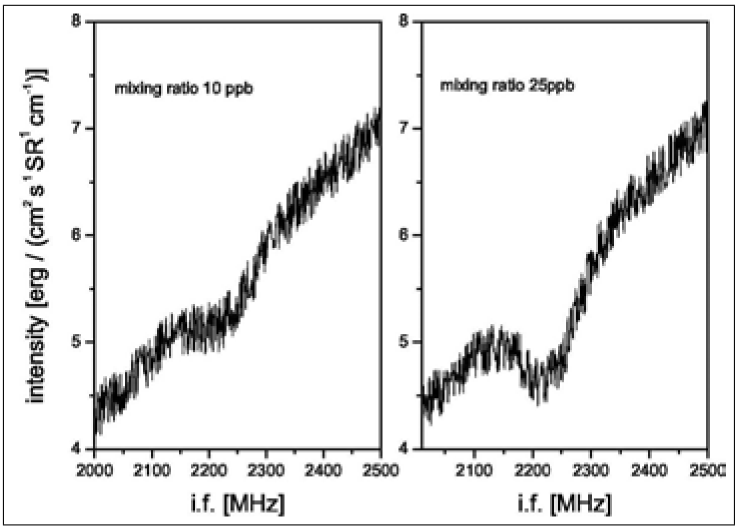

Figure 5.4: *Simulation of methane absorption line at 1277.4734 cm^{-1} incl. Earth transmittance as seen by the heterodyne receiver THIS. The spectra are calculated using the NASA GSFC planetary radiative transport code Codat BEAMINT [104]. Noise level is taken from recent THIS spectra and extrapolated for ~ 10 h of integration time. Temperature/pressure information for Mars was taken from the European Martian Climate Database (*http://johnson.lmd.jussieu.fr:8080/ las/servlets /dataset*).*

levels appear to correlate with solar activity [105]. Due to differences in the photochemical behavior of ethane and acetylene, observations of acetylene would be complementary to ethane observation and increase the understanding of the upper atmosphere of Jupiter. Mid-IR heterodyne observation at a wavelength of 12 μm of acetylene can only be accomplished with the instrument THIS due to the availability of QCLs as LOs.

With the planned extension of the wavelength range additional molecules are coming into the view of THIS. Fully resolved H_2 emission lines can be used to determine temperature profiles of the giant planets' atmospheres, especially on Uranus and Neptune, where no other atmospheric constituents are well mixed in the stratospheres.

Dynamical properties are not only of interest on Venus and Mars but also on planetary moons recently attracting increasing attention. High resolution detection of SO_2 features on Io at limb positions can be used to measure Doppler shifts and to determine wind velocities. A comparison at different positions of Io relative to Jupiter would provide quantitative information about the interaction of Io's atmosphere with the plasma torus around Jupiter [106]. In coordination with modelers a project to investigate Io's dynamical properties is in preparation.

High resolution observations of ethane emission lines emerging from Titans atmosphere have already revealed Doppler-shifts that determine global zonal wind velocity on Titan up to 190±90 m/s prograde speed [107] and further investigations are required.

Even though using THIS for planetary applications proved to be a very successful application on its own, the original goal was to develop an instrument for astrophysical observations, primary for investigations of the H_2 molecule in the interstellar medium. Mid-IR heterodyne technique might be the only feasible tool to investigate cold H_2 in the interstellar medium in absorption versus warm background sources due to the expected narrow linewidths.

Another application beyond planetary science is spectrally resolved observations of molecular features in stars and stellar envelopes like on IRC+10216, Alpha Orionis etc. Molecular absorption lines were already measured in sunspot. The linewidth and shape were used to calculate a kinetic temperature of 10000 K, which is much higher than the physical temperatures of sunspots [86]. Measurements of acetylene, methane and ethylene, and a search for ethane on IRC+10216 are already proposed for February 2009 as well as a observations of water on Alpha Orionis.

The retrieval of astronomical data with the receiver THIS has overcome the experimental status and systematic observations on scientific questions are possible. The future plan is not to have an unchanged "status quo" of the instrument but to continuously use the experimental experience of the people involved to open new fields of applications hand in hand with achieving a better convenience of operation and handling of the instrument.

Appendix A

Sensitivity of Heterodyne Detection

To determine T_{sys} the Y–factor measurement method is generally applied where system response R_i to thermal loads at different and known brightness temperatures J_i is measured.

$$Y = \frac{R_{hot}}{R_{cold}} \sim \frac{T_{sys} + J_{hot}}{T_{sys} + J_{cold}} \tag{A.1}$$

The brightness temperatures J_i of the loads at the operating wavelength are determined by Planck's law from the physical temperatures T_{phys} and the quantum limit T_{ql} using

$$J = T_{ql} \cdot \left(e^{\frac{T_{ql}}{T_{phys}}} - 1 \right)^{-1} \tag{A.2}$$

which is the spectral power in one single spatial mode, to which the receiver is sensitive to. Inverting Eq. A.1 directly yields the system noise temperature for each spectrometer channel:

$$T_{sys} = \frac{J_{hot} - Y \cdot J_{cold}}{Y - 1}$$

The system noise temperature for direct or heterodyne detection can be derived from noise considerations (see [14]). Neglecting contributions from detecter and bias and IF amplifiers for background limited operation T_{sys} is given for a heterodyne system by

$$T_{sys} = \frac{1}{2} \cdot \frac{T_{ql}}{\eta_H} \cdot (2 + 2 \cdot q \cdot \eta_H \cdot n) \tag{A.3}$$

where η_H is the efficiency of the heterodyne system which can be close two one for sensitive instruments. n is the single mode occupation number of thermal radiation given by the Bose-Einstein statistics (equal to J/T_{ql}, see A.2).

For a direct detection system T_{sys} is given by

$$T_{sys} = \frac{1}{2} \cdot \frac{T_{ql}}{\eta_D} \cdot \sqrt{2 \cdot q \cdot \eta_D \cdot s \cdot n} \tag{A.4}$$

again neglecting contributions from detecter and bias and IF amplifiers. η_D is the efficiency of the direct detection instrument which is usually significantly lower than 10% for high spectral resolution instruments. s is the number of spatial modes which are seen by the detector and is usually much larger than 1.

Compared to the also widely used noise-equivalent-power (NEP) the system noise temperature T_{sys} is not depending on spectral resolution. To relate the (frequency dependent) sensitivity of the spectrometer to other systems the conversion between NEP and T_{sys} is given below. The NEP is defined as the minimum detectable power of a system with a given post detection bandwidth of 1 Hz. To take the double side band(DSB) detection into account the resolution bandwidth δ_{res} has to be doubled.

With an integration time of 0.5 s this leads to the following relation between NEP and T_{sys} :

$$NEP = 2^{\frac{3}{2}} \cdot k_B \cdot T_{sys} \cdot \sqrt{\frac{\delta_{res}}{q}} \tag{A.5}$$

Where q is the ratio between fluctuation and resolution bandwidth q = $\frac{B_{fl}}{\delta_{res}}$ and is in the order of 1.5 for our system.

Appendix B

Temperatures and Fluxes

As mentioned above the measured spectra of the heterodyne spectrometer THIS are directly calibrated to brightness temperatures (antenna temperature) in reference to the 673 K blackbody. To get information about the flux of observed astronomical source these temperatures have to be converted into fluxes (depending on wavenumber) per steradians ($F_{\frac{1}{\lambda}}^{Sr}$) with commonly used units of $[\frac{erg}{sec \cdot cm^2 \cdot cm^{-1} \cdot Sr}]$. Fluxes per steradians are useful for extended sources like planets where the source distribution is larger than the telescope beam width (Fluxes can also be given depending on frequency $F_\nu^{Sr} = F_{\frac{1}{\lambda}}^{Sr}/c$.) hence the antenna aperture has no influence.

With the antenna theorem $\Omega_B \cdot A = \lambda^2$ which gives the solid angle of the telescope Ω_B the antenna temperature T_A can be related to the flux. Multiplying the solid angle of the telescope with the flux per steradians gives the total flux

$$F_\nu^{Sr} = \frac{k_B \cdot T_A}{\lambda^2} \quad \text{respectively} \quad F_{\frac{1}{\lambda}}^{Sr} = \frac{T_A \cdot k_B \cdot c}{\lambda^2} \tag{B.1}$$

and hence T_A:

$$T_A = \frac{F_\nu^{Sr} \cdot \lambda^2}{k_B} = \frac{F_{\frac{1}{\lambda}^{Sr}} \cdot \lambda^2}{k_B \cdot c}$$

In observational practice the characteristics of the used spectrometer, i.e. DSB detection or polarization effects must also be taken into account.

Appendix C

Venus Data Acquisition

The measured line-of-sight velocity v_{los} is a component of the SS-AS outflow velocity v_{SS-AS} along the trajectory from the subsolar point to the antisolar point. To transform the v_{los} into v_{SS-AS} the Cartesian coordinate system is displaced from subearth centroid to a subsolar centroid [108]. x, y, z are the coordinates of the observed position just as x_{SS}, y_{SS}, z_{SS} describe the position of the subsolar point. The coordinates of a point expressed by planetary longitude α and latitude β (and optional by an additional rotation angle ϕ) are given by

$$x = cos(\alpha) \cdot cos(\beta) \cdot cos(\phi) - sin(\beta) \cdot sin(\phi) \tag{C.1}$$

$$y = sin(\alpha) \cdot cos(\beta) \tag{C.2}$$

$$z = sin(\beta) \cdot cos(\phi) + cos(\alpha) \cdot cos(\beta) \cdot sin(\phi) \tag{C.3}$$

The unit vectors $\overrightarrow{S}$ (in the dirction of the sun) and $\overrightarrow{P}$ (in the dirction of the observed position) and $\overrightarrow{U}$ are the unit vectors of the new system.

$$\overrightarrow{U} = \frac{\overrightarrow{S} \times \overrightarrow{P}}{|\overrightarrow{S} \cdot \overrightarrow{P}|} \tag{C.4}$$

The SS-AS flow velocity $\overrightarrow{V}$ is now a tangent to the unit circle with the radius $\overrightarrow{P}$ and orthogonal to $\overrightarrow{U}$ and hence

$$\overrightarrow{V} = \overrightarrow{U} \times \overrightarrow{P} \tag{C.5}$$

is valid. To retrieve the x component of the SS-AS outflow, which is the value of interest, the measured line-of-sight velocity has to be transformed into

$$v_{SS-SA} = \overrightarrow{V}(x)_{SS-SA} = v_{los} \cdot [z \cdot (\frac{(x \cdot z_{SS} - z \cdot x_{SS})}{sin(SZA)}) - y \cdot (\frac{(y \cdot x_{SS} - x \cdot y_{SS})}{sin(SZA)})]^{-1} \tag{C.6}$$

With Equ. 2.1 the maximum wind velocity v_{max} at the terminator can be determined for a given outflow velocity v_{SS-AS} retrieved from the Equ. C.6 above.

Bibliography

[1] Website. Available online at `http://solarsystem.nasa.gov/multimedia/gallery/terr_sizes.jpg`; visited on October 2008.

[2] M. M. Abbas, M. J. Mumma, T. Kostiuk, and D. Buhl. Sensitivity limits of an infrared heterodyne spectrometer for astrophysical applications. *Appl. Opt.*, 15:427–436, 1976.

[3] A. L. Betz, M. A. Johnson, R. A. McLaren, and E. C. Sutton. Heterodyne detection of CO2 emission lines and wind velocities in the atmosphere of Venus. *Astrophysical Journall*, 208:L141–L144, September 1976.

[4] A. Delahaigue, D. Courtois, C. Thiébeaux, S. Kalité, and B. Parvitte. Atmospheric laser heterodyne detection. *Infrared Physics and Technology*, 37:7–12, February 1996.

[5] H. Fukunishi, S. Okano, M. Taguchi, and T. Ohnuma. Laser heterodyne spectrometer using a liquid nitrogen cooled tunable diode laser for remote measurements of atmospheric O3 and N2O. *Appl. Opt.*, 29:2722–2728, June 1990.

[6] M. Koide, M. Taguchi, H. Fukunishi, and S. Okano. Ground-based remote sensing of methane height profiles with a tunable diode laser heterodyne spectrometer. *Geophysical Research Letters*, 22:401–404, February 1995. doi: 10.1029/95GL00051.

[7] T. Kostiuk, F. Espenak, M. J. Mumma, and P. Romani. Infrared studies of hydrocarbons on Jupiter. *Infrared Physics*, 29:199–204, May 1989.

[8] T. Kostiuk, K. E. Fast, T. A. Livengood, T. Hewagama, J. J. Goldstein, F. Espenak, and D. Buhl. Direct measurement of winds of Titan. *Geophysical Research Letters*, 28:2361–2364, June 2001. doi: 10.1029/2000GL012617.

[9] D. W. Peterson, M. A. Johnson, and A. L. Betz. Infrared heterodyne spectroscopy of CO_2 on Mars. *Natur*, 250:128–130, July 1974. doi: 10.1038/250128a0.

[10] H. Rothermel, H. U. Kaeufl, and Y. Yu. A heterodyne spectrometer for astronomical measurements at 10 micrometers. *Astronomy and Astrophysics*, 126:387–392, October 1983.

[11] F. Schmülling, B. Klumb, M. Harter, R. Schieder, B. Vowinkel, and G. Winnewisser. High-Sensitivity Mid-Infrared Heterodyne Spectrometer With a Tunable Diode Laser as a Local Oscillator. *Appl. Opt.*, 37:5771–5776, August 1998.

[12] G. Sonnabend, M. Sornig, P. J. Kroetz, R. T. Schieder, and K. E. Fast. High spatial resolution mapping of Mars mesospheric zonal winds by infrared heterodyne spectroscopy of CO_2. *GRL*, 33: 18201–+, September 2006. doi: 10.1029/2006GL026900.

[13] R. T. Menzies. *Laser heterodyne detection techniques*, pages 297–353. Laser monitoring of the atmosphere. (A77-22051 08-35) Berlin and New York, Springer-Verlag, 1976, p. 297-353., 1976.

[14] R. Schieder. Noise at Direct- and Heterodyne-Detection at Infrared Wavelenths. *Journal of Quantitative Spectroscopy and Radiative Transfer*, 2008. submitted.

[15] T. Kostiuk and M. J. Mumma. Remote sensing by IR heterodyne spectroscopy. *Appl. Opt.*, 22:2644–2654, 1983.

[16] R. Schieder. High resolution diode laser and heterodyne spectroscopy with applications toward remote sensing. *Infrared Physics and Technology*, 35:477–486, April 1994.

[17] R. T. Ku and D. L. Spears. High-sensitivity infrared heterodyne radiometer using a tunable-diode-laser local oscillator. *Optics Letters*, 1:84–86, September 1977.

[18] D. Glenar, T. Kostiuk, D. E. Jennings, D. Buhl, and M. J. Mumma. Tunable diode-laser heterodyne spectrometer for remote observations near 8 μm. *Appl. Opt.*, 21:253–259, January 1982.

[19] G. Sonnabend, D. Wirtz, F. Schmulling, and R. Schieder. Tuneable Heterodyne Infrared Spectrometer for atmospheric and astronomical studies. *Appl. Opt.*, 41:2978–2984, May 2002.

[20] G. Sonnabend, D. Wirtz, and R. Schieder. Evaluation of quantum-cascade lasers as local oscillators for infrared heterodyne spectroscopy. *Appl. Opt.*, 44:7170–7172, November 2005.

[21] D. Wirtz. *Erste Beobachtungen mit dem abstimmbaren Infrarot-Heterodynsystem THIS.* PhD thesis, I. Physikalisches Institut der Universtiät zu Köln, Cologne, Germany, February 2005.

[22] W. S. Adams and T. Dunham, Jr. Absorption Bands in the Infra-Red Spectrum of Venus. *Publications of the Astronomical Society of the Pacific*, 44:243–245, August 1932.

[23] C. H. Mayer, T. P. McCullough, and R. M. Sloanaker. Observations of Venus at 3.15-CM Wave Length. *Astrophysical Journal*, 127:1–+, January 1958.

[24] L. S. Elson. Preliminary results from the Pioneer Venus Orbiter infrared radiometer - Temperature and dynamics in the upper atmosphere. *Geophysical Research Letters*, 6:720–722, September 1979.

[25] F. W. Taylor, D. J. Diner, L. S. Elson, D. J. McCleese, J. V. Martonchik, J. Delderfield, S. P. Bradley, J. T. Schofield, J. C. Gille, and M. T. Coffey. Temperature, cloud structure, and dynamics of Venus middle atmosphere by infrared remote sensing from Pioneer Orbiter. *Science*, 205:65–67, July 1979.

[26] C. Boyer and P. Guérin. Étude de la Rotation Rétrograde, en 4 Jours, de la Couche Extérieure Nuageuse de Vénus. *Icarus*, 11: 338–+, November 1969.

[27] V. V. Kerzhanovich and S. S. Limaye. Circulation of the atmosphere from the surface to 100 KM. *Advances in Space Research*, 5:59–83, 1985. doi: 10.1016/0273-1177(85)90198-X.

[28] C. C. Counselman, S. A. Gourevitch, R. W. King, G. B. Loriot, and E. S. Ginsberg. Zonal and meridional circulation of the lower atmosphere of Venus determined by radio interferometry. *Journal of Geophysical Research*, 85:8026–8030, December 1980.

[29] R. W. Carlson, K. H. Baines, L. W. Kamp, P. R. Weissman, W. D. Smythe, A. C. Ocampo, T. V. Johnson, D. L. Matson, J. B. Pollack, and D. Grinspoon. Galileo infrared imaging spectroscopy measurements at Venus. *Science*, 253:1541–1548, September 1991.

[30] D. Crisp, S. McMuldroch, S. K. Stephens, W. M. Sinton, B. Ragent, K.-W. Hodapp, R. G. Probst, L. R. Doyle, D. A. Allen, and J. Elias. Ground-based near-infrared imaging observations of Venus during the Galileo encounter. *Science*, 253:1538–1541, September 1991.

[31] S. Limaye, J. Warell, B. C. Bhatt, P. M. Fry, and E. F. Young. Multi-observatory observations of night-side of Venus at 2.3 micron - atmospheric circulation from tracking of cloud features. *Bulletin of the Astronomical Society of India*, 34:189–+, June 2006.

[32] R. Z. Sagdeyev, V. V. Kerzhanovitch, L. R. Kogan, V. I. Kostenko, V. M. Linkin, L. I. Matveyenko, R. R. Nazirov, S. V. Pogregenko, I. A. Struckov, R. A. Preston, J. Purcel, C. E. Hildebrand, V. A. Grishmanovskiy, A. N. Kozlov, E. P. Molotov, J. E. Blamont, L. Boloh, G. Laurans, P. Kaufmann, J. Galt, F. Biraud, A. Boischot, A. Ortega-Molina, C. Rosolen, G. Petit, P. G. Mezger, R. Schwartz, B. O. Ronnang, R. E. Spencer, G. Nicolson, A. E. E. Rogers, M. H. Cohen, R. M. Martirosyan, I. G. Moiseyev, and J. S. Jatskiv. Differential VLBI Measurements of the Venus Atmosphere Dynamics by Balloons - VEGA Project. *Astronomy and Astrophysics*, 254:387–+, February 1992.

[33] S. S. Limaye and V. E. Suomi. Cloud motions on Venus - Global structure and organization. *Journal of Atmospheric Sciences*, 38: 1220–1235, June 1981.

[34] S. S. Limaye, C. Grassotti, and M. J. Kuetemeyer. Venus: Cloud level circulation during 1982 as determined from Pioneer cloud photopolarimeter images. I - Time and zonally averaged circulation. *Icarus*, 73:193–211, February 1988. doi: 10.1016/0019-1035(88) 90093-0.

[35] S. S. Limaye. Venus: Cloud level circulation during 1982 as determined from Pioneer cloud photopolarimeter images. II - Solar longitude dependent circulation. *Icarus*, 73:212–226, February 1988. doi: 10.1016/0019-1035(88)90094-2.

[36] W. B. Rossow, A. D. del Genio, and T. Eichler. Cloud-tracked winds from Pioneer Venus OCPP images. *Journal of Atmospheric Sciences*, 47:2053–2084, September 1990.

[37] M. J. S. Belton, P. J. Gierasch, M. D. Smith, P. Helfenstein, P. J. Schinder, J. B. Pollack, K. A. Rages, D. Morrison, K. P. Klaasen, and C. B. Pilcher. Images from Galileo of the Venus cloud deck. *Science*, 253: 1531–1536, September 1991.

[38] A. Toigo, P. J. Gierasch, and M. D. Smith. High resolution cloud feature tracking on Venus by Galileo. *Icarus*, 109:318–336, June 1994. doi: 10.1006/icar.1994.1097.

[39] M. Pätzold, B. Häusler, M. K. Bird, S. Tellmann, R. Mattei, S. W. Asmar, V. Dehant, W. Eidel, T. Imamura, R. A. Simpson, and G. L. Tyler. The structure of Venus' middle atmosphere and ionosphere. *nature*, 450:657–660, November 2007. doi: 10.1038/nature06239.

[40] I. de Pater and J. Lissauer. *Planetary Sciences*. Planetary Sciences, by Imke de Pater and Jack Lissauer. Cambridge University Press, 2001, 544 pp., 2001.

[41] Website. Available online at `http://en.wikipedia.org/wiki/Image:Venus$_-$circulation.jpg`; visited on October 2008.

[42] W. J. Markiewicz, D. V. Titov, S. S. Limaye, H. U. Keller, N. Ignatiev, R. Jaumann, N. Thomas, H. Michalik, R. Moissl, and P. Russo. Morphology and dynamics of the upper cloud layer of Venus. *Natur*, 450:633–636, November 2007. doi: 10.1038/nature06320.

[43] G. Piccioni, P. Drossart, A. Sanchez-Lavega, R. Hueso, F. W. Taylor, C. F. Wilson, D. Grassi, L. Zasova, M. Moriconi, A. Adriani, S. Lebonnois, A. Coradini, B. Bézard, F. Angrilli, G. Arnold, K. H. Baines, G. Bellucci, J. Benkhoff, J. P. Bibring, A. Blanco, M. I. Blecka, R. W. Carlson, A. di Lellis, T. Encrenaz, S. Erard, S. Fonti, V. Formisano, T. Fouchet, R. Garcia, R. Haus, J. Helbert, N. I. Ignatiev, P. G. J. Irwin, Y. Langevin, M. A. Lopez-Valverde, D. Luz, L. Marinangeli, V. Orofino, A. V. Rodin, M. C. Roos-Serote, B. Saggin, D. M. Stam, D. Titov, G. Visconti, M. Zambelli, E. Ammannito, A. Barbis, R. Berlin, C. Bettanini, A. Boccaccini, G. Bonnello, M. Bouye, F. Capaccioni, A. Cardesin Moinelo, F. Carraro, G. Cherubini, M. Cosi, M. Dami, M. de Nino, D. Del Vento, M. di Giampietro, A. Donati, O. Dupuis, S. Espinasse, A. Fabbri, A. Fave, I. F. Veltroni, G. Filacchione, K. Garceran, Y. Ghomchi, M. Giustini, B. Gondet, Y. Hello, F. Henry, S. Hofer, G. Huntzinger, J. Kachlicki, R. Knoll, K. Driss, A. Mazzoni, R. Melchiorri, G. Mondello, F. Monti, C. Neumann, F. Nuccilli, J. Parisot, C. Pasqui, S. Perferi, G. Peter, A. Piacentino, C. Pompei, J.-M. Reess, J.-P. Rivet, A. Romano, N. Russ, M. Santoni, A. Scarpelli, A. Semery, A. Soufflot, D. Stefanovitch, E. Suetta, F. Tarchi, N. Tonetti, F. Tosi, and B. Ulmer. South-polar features on Venus similar to those near the north pole. *Natur*, 450:637–640, November 2007. doi: 10.1038/nature06209.

[44] P. J. Gierasch, R. M. Goody, R. E. Young, D. Crisp, C. Edwards, R. Kahn, D. Rider, A. del Genio, R. Greeley, A. Hou, C. B. Leovy, D. McCleese, and M. Newman. The General Circulation of the Venus Atmosphere: an Assessment. In S. W. Bougher, D. M. Hunten, and R. J. Philips, editors, *Venus II: Geology, Geophysics, Atmosphere, and Solar Wind Environment*, pages 459–+, 1997.

[45] J. J. Goldstein, M. J. Mumma, T. Kostiuk, D. Deming, F. Espenak, and D. Zipoy. Absolute wind velocities in the lower thermosphere of Venus using infrared heterodyne spectroscopy. *Icarus*, 94:45–63, November 1991. doi: 10.1016/0019-1035(91)90140-O.

[46] S. W. Bougher, R. E. Dickinson, E. C. Ridley, R. G. Roble, A. F. Nagy, and T. E. Cravens. Venus mesosphere and thermosphere. II - Global circulation, temperature, and density variations. *Icarus*, 68:284–312, November 1986. doi: 10.1016/0019-1035(86)90025-4.

[47] S. W. Bougher, R. G. E. Roble, R. E. Dickinson, and E. C. Ridley. Venus mesosphere and thermosphere. III - Three-dimensional general circulation with coupled dynamics and composition. *Icarus*, 73:545–573, March 1988. doi: 10.1016/0019-1035(88)90064-4.

[48] T. Kostiuk. Physics and chemistry of upper atmospheres of planets from infrared observations. *Infrared Physics and Technology*, 35:243–266, April 1994.

[49] F. Schmülling, J. Goldstein, T. Kostiuk, T. Hewagama, and D. Zipoy. High precision Wind measurements in the upper Venus atmosphere. In *Bulletin of the American Astronomical Society*, volume 32 of *Bulletin of the American Astronomical Society*, pages 1121–+, October 2000.

[50] K. P. Shah, D. O. Muhleman, and G. L. Berge. Measurement of winds in Venus' upper mesosphere based on Doppler shifts of the 2.6-mm (C-12)O line. *Icarus*, 93:96–121, September 1991. doi: 10.1016/0019-1035(91)90167-R.

[51] D. Buhl, G. Chin, and J. J. Goldstein. Discovery of a Doppler-limited CO line in the upper mesosphere of Venus - A new dynamical probe. *Astrophysical Journal*, 369:L17–L20, March 1991. doi: 10.1086/185949.

[52] E. Lellouch, J. J. Goldstein, J. Rosenqvist, S. W. Bougher, and G. Paubert. Global circulation, thermal structure, and carbon monoxide distribution in Venus' mesosphere in 1991. *Icarus*, 110: 315–339, August 1994. doi: 10.1006/icar.1994.1125.

[53] T. Widemann, E. Lellouch, and A. Campargue. New wind measurements in Venus' lower mesosphere from visible spectroscopy. *Planetary and Space Science*, 55:1741–1756, October 2007. doi: 10.1016/j.pss.2007.01.005.

[54] D. Deming and M. J. Mumma. Modeling of the 10-micron natural laser emission from the mesospheres of Mars and Venus. *Icarus*, 55:356–368, September 1983. doi: 10.1016/0019-1035(83)90108-2.

[55] M. A. Johnson, A. L. Betz, R. A. McLaren, C. H. Townes, and E. C. Sutton. Nonthermal 10 micron CO2 emission lines in the atmospheres of Mars and Venus. *Astrophysical Journall*, 208:L145–L148, September 1976.

[56] C. Roldan, M. A. Lopez-Valverde, M. Lopez-Puertas, and D. P. Edwards. Non-LTE Infrared Emissions of CO_2 in the Atmosphere of Venus. *Icarus*, 147:11–25, September 2000. doi: 10.1006/icar.2000.6432.

[57] M. J. Mumma, D. Buhl, G. Chin, D. Deming, F. Espenak, T. Kostiuk, and D. Zipoy. Discovery of natural gain amplification in the 10-micrometer carbon dioxide laser bands on Mars - A natural laser. *Science*, 212:45–49, April 1981.

[58] W. C. Maguire, J. C. Pearl, M. D. Smith, B. J. Conrath, A. A. Kutepov, M. S. Kaelberer, E. Winter, and P. R. Christensen. Observations of high-altitude CO_2 hot bands in Mars by the orbiting Thermal Emission Spectrometer. *Journal of Geophysical Research (Planets)*, 107:5063–+, September 2002. doi: 10.1029/2001JE001516.

[59] T. A. Livengood, T. Kostiuk, K. E. Fast, J. N. Annen, G. Sonnabend, and T. Hewagama. Meridional Mapping of Mesospheric Temperatures from CO_2 Emission along the MGS Ground Track. In *Bulletin of the American Astronomical Society*, volume 35 of *Bulletin of the American Astronomical Society*, pages 913–+, May 2003.

[60] M. Newman, G. Schubert, A. J. Kliore, and I. R. Patel. Zonal winds in the middle atmosphere of Venus from Pioneer Venus radio occultation data. *Journal of Atmospheric Sciences*, 41:1901–1913, June 1984.

[61] M. Rengel, P. Hartogh, and C. Jarchow. Mesospheric vertical thermal structure and winds on Venus from HHSMT CO spectral-line observations. *Planetary and Space Science*, 56:1368–1384, August 2008. doi: 10.1016/j.pss.2008.07.004.

[62] R. T. Clancy, B. J. Sandor, and G. H. Moriarty-Schieven. Venus upper atmospheric CO, temperature, and winds across the afternoon/evening terminator from June 2007 JCMT sub-millimeter line observations. *Planetary and Space Science*, 56:1344–1354, August 2008. doi: 10.1016/j.pss.2008.05.007.

[63] E. Lellouch, G. Paubert, R. Moreno, and A. Moullet. Monitoring Venus' mesospheric winds in support of Venus Express: IRAM 30-m and APEX observations. *Planetary and Space Science*, 56:1355–1367, August 2008. doi: 10.1016/j.pss.2008.06.010.

[64] T. Widemann, E. Lellouch, and J.-F. Donati. Venus Doppler winds at cloud tops observed with ESPaDOnS at CFHT. *Planetary and Space Science*, 56:1320–1334, August 2008. doi: 10.1016/j.pss.2008.07.005.

[65] P. Gaulme, F.-X. Schmider, C. Grec, A. López Ariste, T. Widemann, and B. Gelly. Venus wind map at cloud top level with the MTR/THEMIS visible spectrometer, I: Instrumental performance and first results. *Planetary and Space Science*, 56:1335–1343, August 2008. doi: 10.1016/j.pss.2008.06.014.

[66] Y. Gabsi, J. L. Bertaux, A. Hauchecorne, J. Schmitt, and S. Guibert. Measuring Venus' winds using the Absolute Astronomical Accelerometer: Solid super-rotation model of Venus' clouds. *Planetary and Space Science*, 56:1454–1466, October 2008. doi: 10.1016/j.pss.2008.07.016.

[67] M. Lopez-Puertas and F.W. Taylor. *Non-LTE Radiative Transfer in the Atmosphere*. World Scientific Publishing Co. Pte. Ltd., P O Box 128, Farrer Road, Singapore 912805, series on atmospheric, oceanic and planetary phyics - vol.3 edition, 2001. ISBN 981-02-4566-1.

[68] H. U. Kaufl, H. Rothermal, and S. Drapatz. Investigation of the Martian atmosphere by 10 micron heterodyne spectroscopy. *Astronomy and Astrophysics*, 136:319–325, July 1984.

[69] P. Drossart, G. Piccioni, J. C. Gérard, M. A. Lopez-Valverde, A. Sanchez-Lavega, L. Zasova, R. Hueso, F. W. Taylor, B. Bézard, A. Adriani, F. Angrilli, G. Arnold, K. H. Baines, G. Bellucci, J. Benkhoff, J. P. Bibring, A. Blanco, M. I. Blecka, R. W. Carlson, A. Coradini, A. di Lellis, T. Encrenaz, S. Erard, S. Fonti, V. Formisano, T. Fouchet, R. Garcia, R. Haus, J. Helbert, N. I. Ignatiev, P. Irwin, Y. Langevin, S. Lebonnois, D. Luz, L. Marinangeli, V. Orofino, A. V. Rodin, M. C. Roos-Serote, B. Saggin, D. M. Stam, D. Titov, G. Visconti, M. Zambelli, C. Tsang, E. Ammannito, A. Barbis, R. Berlin, C. Bettanini, A. Boccaccini, G. Bonnello, M. Bouyé, F. Capaccioni, A. Cardesin, F. Carraro, G. Cherubini, M. Cosi, M. Dami, M. de Nino, D. Del Vento, M. di Giampietro, A. Donati, O. Dupuis, S. Espinasse, A. Fabbri, A. Fave, I. Ficai Veltroni, G. Filacchione, K. Garceran, Y. Ghomchi, M. Giustizi, B. Gondet, Y. Hello, F. Henry, S. Hofer, G. Huntzinger, J. Kachlicki, R. Knoll, D. Kouach, A. Mazzoni, R. Melchiorri, G. Mondello, F. Monti, C. Neumann, F. Nuccilli, J. Parisot, C. Pasqui, S. Perferi, G. Peter, A. Piacentino, C. Pompei, J.-M. Réess, J.-P. Rivet, A. Romano, N. Russ, M. Santoni, A. Scarpelli, A. Sémery, A. Soufflot, D. Stefanovitch, E. Suetta, F. Tarchi, N. Tonetti, F. Tosi, and B. Ulmer. A dynamic upper atmosphere of Venus as revealed by VIRTIS on Venus Express. *Natur*, 450:641–645, November 2007. doi: 10.1038/nature06140.

[70] A. Kliore, D. L. Cain, G. S. Levy, V. R. Eshleman, G. Fjeldbo, and F. D. Drake. Occultation Experiment: Results of the First Direct

Measurement of Mars's Atmosphere and Ionosphere. *Science*, 149: 1243–1248, September 1965.

[71] C. A. Barth, C. W. Hord, J. B. Pearce, K. K. Kelly, G. P. Anderson, and A. I. Stewart. Mariner 6 and 7 ultraviolet spectrometer experiment: Upper atmosphere data. *J. Geophys. Res.*, 76:2213–2227, 1971.

[72] C. A. Barth, C. W. Hord, A. I. Stewart, A. L. Lane, M. L. Duck, and G. P. Anderson. Mariner 9 ultraviolet spectrometer experiment: Seasonal variation of ozone on Mars. *Science*, 179:795–796, February 1973.

[73] R. Hanel, B. Conrath, W. Hovis, V. Kunde, P. Lowman, W. Maguire, J. Pearl, J. Pirraglia, C. Prabhakara, B. Schlachman, G. Levin, P. Straat, and T. Burke. Investigation of the Martian Environment by Infrared Spectroscopy on Mariner 9 (A 5. 2). *Icarus*, 17:423–+, October 1972.

[74] S. L. Hess, R. M. Henry, C. B. Leovy, J. E. Tillman, and J. A. Ryan. Meteorological results from the surface of Mars - Viking 1 and 2. *J. Geophys. Res.*, 82:4559–4574, September 1977.

[75] Website. Available online at `http://johnson.lmd.jussieu.fr:8080/las/servlets/dataset?catitem=0`; visited on October 2008.

[76] G. L. Villanueva. *The High Resolution Spectrometer for SOFIA-GREAT: Instrumentation, Atmospheric Modeling and Observations*. PhD thesis, Max-Planck-Institut fuer Sonnensystemforschung, November 2004.

[77] R. Moreno, E. Lellouch, T. Encrenaz, F. Forget, E. Chassefiere, F. Hourdin, and S. Guilloteau. Wind measurements in Mars' middle atmosphere at equinox and solstice: IRAM Plateau de Bure interferometric CO observations. In F. Forget, M. A. Lopez-Valverde, M. C. Desjean, J. P. Huot, F. Lefevre, S. Lebonnois, S. R. Lewis, E. Millour, P. L. Read, and R. J. Wilson, editors, *Mars Atmosphere Modelling and Observations*, pages 134–+, February 2006.

[78] R. T. Clancy, B. J. Sandor, G. H. Moriarty-Schieven, and M. D. Smith. Mesospheric winds and temperatures from JCMT submillimeter CO line observations during the 2003 and 2005 Mars oppositions. In F. Forget, M. A. Lopez-Valverde, M. C. Desjean, J. P. Huot, F. Lefevre, S. Lebonnois, S. R. Lewis, E. Millour, P. L. Read, and R. J. Wilson, editors, *Mars Atmosphere Modelling and Observations*, pages 135–+, February 2006.

[79] E. Lellouch, J. Rosenqvist, J. J. Goldstein, S. W. Bougher, and G. Paubert. First absolute wind measurements in the middle atmosphere of Mars. *Astrophysical Journal*, 383:401–406, December 1991. doi: 10.1086/170797.

[80] G. Sonnabend, D. Wirtz, V. Vetterle, and R. Schieder. High-resolution observations of Martian non-thermal CO_2 emission near 10 μm with a new tuneable heterodyne receiver. *Astronomy and Astrophysics*, 435:1181–1184, June 2005. doi: 10.1051/0004-6361:20042393.

[81] Website. Available online at `http://sealevel.jpl.nasa.gov/overview/climate-climatic.html`; visited on October 2008.

[82] G. Sonnabend, M. Sornig, P. Kroetz, D. Stupar, and R. Schieder. Ultra high spectral resolution observations of planetary atmospheres using the Cologne tuneable heterodyne infrared spectrometer. *Journal of Quantitative Spectroscopy and Radiative Transfer*, 109:1016–1029, April 2008.

[83] G. Sonnabend. *Aufbau und Charakterisierung des Infrarot-Heterodyn-Spektrometers THIS*. PhD thesis, I. Physikalisches Institut der Universtiät zu Köln, Cologne, Germany, 2002.

[84] F. Schmülling. *Entwicklung eines hochauflösenden Infrarot-Heterodynspektrometers mit einem Bleisalz-Diodenlaser als Lokaloszillator.* PhD thesis, I. Physikalisches Institut der Universtiät zu Köln, Cologne, Germany, 1997.

[85] M. Harter. *Entwicklung eines hochauflösenden Infrarot-Heterodynspektrometers zur Messung von atmosphärischen Spurengasen.* PhD thesis, I. Physikalisches Institut der Universtiät zu Köln, Cologne, Germany, 1992.

[86] G. Sonnabend, D. Wirtz, R. Schieder, and P. F. Bernath. High-Resolution Infrared Measurements of H_2O and SiO in Sunspots. *Solar Physics*, 233:205–213, February 2006. doi: 10.1007/s11207-006-2488-9.

[87] R. Maulini, A. Mohan, M. Giovannini, J. Faist, and E. Gini. External cavity quantum-cascade laser tunable from 8.2 to 10.4 μm using a gain element with a heterogeneous cascade. *Applied Physics Letters*, 88(20):201113–+, May 2006. doi: 10.1063/1.2205183.

[88] D. Stupar. *Untersuchungen eines Quantenkaskadenlasersystems mit einem externen Resonator.* PhD thesis, I. Physikalisches Institut der Universtiät zu Köln, Cologne, Germany, 2007.

[89] D. Stupar, J. Krieg, P. Krötz, G. Sonnabend, M. Sornig, T. F. Giesen, and R. Schieder. Fully reflective external-cavity setup for quantum-cascade lasers as a local oscillator in mid-infrared wavelength heterodyne spectroscopy. *Applied Optics*, 47:2993–2997, June 2008.

[90] M. Olbrich. *A 3 GHz instantaneous bandwidth Acousto-Optical spectrometer with 1 MHz resolution.* PhD thesis, I. Physikalisches Institut der Universtiät zu Köln, Cologne, Germany, 2007.

[91] Paul E. Goldsmith. *Quasioptical Systems - Gaussian Beam Quasioptical Propagation and Applications*. IEEE Press, 1998.

[92] R. M. Williams, J. F. Kelly, J. S. Hartman, S. W. Sharpe, M. S. Taubman, J. L. Hall, F. Capasso, C. Gmachl, D. L. Sivco, J. Baillargeon, and A. Y. Cho. Kilohertz linewidth from frequency-stabilized mid-infrared quantum cascade lasers. *Optics Letters*, 24:1844–1846, December 1999.

[93] R. T. Clancy, B. J. Sandor, and G. H. Moriarty-Schieven. Observational definition of the Venus mesopause: vertical structure, diurnal variation, and temporal instability. *Icarus*, 161:1–16, January 2003. doi: 10.1016/S0019-1035(02)00022-2.

[94] Website. Available online at `http://ssd.jpl.nasa.gov/horizons.cgi`; visited on October 2008.

[95] S. R. Lewis, M. Collins, P. L. Read, F. Forget, F. Hourdin, R. Fournier, C. Hourdin, O. Talagrand, and J.-P. Huot. A climate database for Mars. *Journal of Geophysical Research*, 104:24177–24194, October 1999. doi: 10.1029/1999JE001024.

[96] T. Hewagama, J. Goldstein, D. Buhl, F. Espenak, K. Fast, T. Kostiuk, and T. A. Livengood. Spectral Line Analysis for Planetary Atmospheric Dynamics Retrieval. In *Bulletin of the American Astronomical Society*, volume 30 of *Bulletin of the American Astronomical Society*, pages 1093–+, September 1998.

[97] D. P. Edwards. GENLN2: A general line-by-line atmospheric transmittance and radiance model. Version 3.0: Description and users guide. Technical report, January 1992.

[98] F. Forget, E. Millour, F. González-Galindo, A. Spiga, S. R. Lewis, L. Montabone, P. L. Read, M. A. López-Valverde, G. Gilli, M.-C. Desjean, J.-P. Huot, and McD/Gcm Development Team. The New (Version 4.2) Mars Climate Database. *LPI Contributions*, 1353:3098–+, July 2007.

[99] C.-V. Meister, P. Hartogh, G. Villanueva, and U. Berger. Annual behaviour of the general circulation of the Martian atmosphere. *EGS - AGU - EUG Joint Assembly, Abstracts from the meeting held in Nice, France, 6 - 11 April 2003, abstract 4257*, pages 4257–+, April 2003.

[100] R. M. Haberle, J. B. Pollack, J. R. Barnes, R. W. Zurek, C. B. Leovy, J. R. Murphy, H. Lee, and J. Schaeffer. Mars atmospheric dynamics as simulated by the NASA AMES General Circulation Model. I - The zonal-mean circulation. *J. Geophys. Res.*, 98:3093–3123, February 1993.

[101] F. R. Giorgetta, E. Baumann, D. Hofstetter, C. Manz, Q. Yang, K. Koehler, and M. Graf. InGaAs/AlAsSb quantum cascade detectors operating in the near infrared. *Applied Physics Letters*, 91 (11):111115–+, September 2007. doi: 10.1063/1.2784289.

[102] F. P. Mills. *I. Observations and photochemical modeling of the Venus middle atmosphere. II. Thermal infrared spectroscopy of Europa and Callisto*. PhD thesis, CALIFORNIA INSTITUTE OF TECHNOLOGY, 1998.

[103] K. Fast, T. Kostiuk, T. Hewagama, M. F. A'Hearn, T. A. Livengood, S. Lebonnois, and F. Lefèvre. Ozone abundance on Mars from infrared heterodyne spectra. *Icarus*, 183:396–402, August 2006. doi: 10.1016/j.icarus.2006.03.012.

[104] T. Hewagama, J. Goldstein, T. A. Livengood, D. Buhl, F. Espenak, K. Fast, T. Kostiuk, and F. Schmülling. Beam integrated high-resolution infrared spectra: Accurate modeling of thermal emission from extended clear atmospheres. *Journal of Quantitative Spectroscopy and Radiative Transfer*, 109:1081–1097, April 2008.

[105] T. Kostiuk, T. Livengood, K. Fast, T. Hewagama, D. Buhl, F. Schmülling, and J. Goldstein. Jovian northern ethane aurora and the solar cycle. In *Bulletin of the American Astronomical Society*, volume 32 of *Bulletin of the American Astronomical Society*, pages 1020–+, October 2000.

[106] J. Saur, F. M. Neubauer, D. F. Strobel, and M. E. Summers. Io's ultraviolet aurora: Remote sensing of Io's interaction. *Geophysical Research Letters*, 27:2893–2896, September 2000. doi: 10.1029/2000GL003824.

[107] T. Kostiuk, T. A. Livengood, G. Sonnabend, K. E. Fast, T. Hewagama, K. Murakawa, A. T. Tokunaga, J. Annen, D. Buhl, F. Schmülling, D. Luz, and O. Witasse. Stratospheric global winds

on Titan at the time of Huygens descent. *Journal of Geophysical Research (Planets)*, 111(10):7–+, July 2006. doi: 10.1029/2005JE002630.

[108] J.J. Goldstein. *Absolute wind measurements in the lower thermosphere of Venus using infrared heterodyne spectoscopy.* PhD thesis, University of Pennsylvania, USA, 1990.

Acknowledgements

I would like to thank all the people who contributed in the development of this work. I especially thank my supervisor Prof. Dr. Rudolf Schieder for the guidance and sharing of knowledge over many years.

Without the former and present THIS-Team it would have not been possible to carry out this work. Many thanks to the whole team for the help, input, tolerance and all the shared moments of desperations, freakiness and (sometimes even) success in the lab, office and at the telescopes. First of all I would like to thank Guido Sonnabend for his extraordinary support, I wish all the best to Peter Kroetz and Dušan Stupar for their thesis, and many thanks to Daniel Wirtz for the unique introduction in the beginning of my work.

I would also like to thank the Goddard Heterodyne Team, John Annen, Juan Delgado, Kelly Fast, Tilak Hewagama, Theodor Kostiuk and Tim Livengood for sharing their experience and knowledge. I enjoyed our coordinated scientific and/or fun projects.

In addition I thank Luca Montabone for his support and explanations about Mars GCM and Thomas Widemann for cooperation on Venus observations and proof-reading my work.

Part of this observations were carried out at the National Solar Observatory's McMath-Pierce Solar Telescope on Kitt Peak, Arizona, USA. The National Solar Observatory is operated by the Association of Universities for research in Astronomy, Inc. (AURA) under cooperative agreement with the National Science Foundation. I would like to thank Claude Plymate and Eric Galayda for their support during several observing runs.

Furthermore observations were carried out at the NASA Infrared Telescope Facility (IRTF) on Mauna Kea, Hawaii, USA. I would like to thank Lars Bergknut, Dave Griep, Bill Golisch, George Koenig, Imai Namahoe Paul Sears and Alan Tokunaga, as well as other staff members for their help during the observation run.

Many thanks goes to the teams of the mechanical and electronic workshop of our institute for their essential support in modifications of the spectrometer and associated hardware. Also many thanks the secretaries for their help to get along with contracts, customs, bills and a lot more.

Zum Schluss möchte ich mich noch bei meiner Familie und meinen Freunden bedanken, bei Hannes und Julian für ihre unglaubliche Geduld und Nachsicht, bei meinen Eltern für ihre bedingungslose

Unterstützung und Anerkennung über viele Jahre und bei all den Freunden, die mich auf verschiedenste, individuelle Weise begleitet und unterstützt haben: Danke Anni, Christian, Johanna, Jürgen, Mario und Pat.

This work was funded by the German *Deutsche Forschungsgemeinschaft, (DFG)* through Grant **SO879/1-1** (2007-2008) and through Special Grant **494/D2** (2000-2008)

'Ich versichere, dass ich die von mir vorgelegte Dissertation selbständig angefertigt, die benutzten Quellen und Hilfsmittel vollständig angegeben und die Stellen der Arbeit - einschließlich Tabellen, Karten und Abbildungen -, die anderen Werken im Wortlaut oder dem Sinn nach entnommen sind, in jedem Einzelfall als Entlehnung kenntlich gemacht habe; dass diese Dissertation noch keiner anderen Fakultät oder Universität zur Prüfung vorgelegen hat; dass sie - abgesehen von unten angegebenen Teilpublikationen - noch nicht veröffentlicht worden ist sowie, dass ich eine solche Veröffentlichung vor Abschluss des Promotionsverfahrens nicht vornehmen werde.

Die Bestimmungen der Promotionsordnung sind mir bekannt. Die von mir vorgelegte Dissertation ist von Herrn Prof. Dr. Rudolf Schieder betreut worden.'

Köln, 05.11.2008 Manuela Sornig

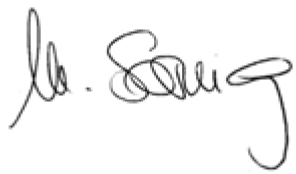

Teile dieser Arbeit sind bzw. werden in folgenden Publikationen veröffentlicht:

M. Sornig, T. Livengood, G. Sonnabend, P. Krötz, D. Stupar, T. Kostiuk, R. Schieder, "Venus upper atmosphere winds from heterodyne spectroscopy of CO_2 at $10\,\mu$m wavelength", Planetary and Space Sciences, Volume 56, Issue 10, p. 1399-1406 (2008), doi:10.1016/j.pss.2008.05.006

G. Sonnabend, M. Sornig, P. Krötz, D. Stupar and R. Schieder, "Ultra high spectral resolution observations of planetary atmospheres using the cologne tuneable heterodyne infrared spectrometer", Journal of Quantitative Spectroscopy & Radiative Transfer, vol. 109, issue. 6, p. 1016-1029.(2007), doi:10.1016/j.jqsrt.2007.12.003

G. Sonnabend, M. Sornig, P. Krötz, K. Fast, R. Schieder, "High Spatial Resolution Mapping of Mars Mesospheric Zonal Winds by Infrared Heterodyne Spectroscopy of CO_2", Geophysical Research Letters, vol. 33, issue 18, CiteID L18201 (2006), doi:10.1029/2006GL026900

Curriculum Vitae

Persönliche Daten:

- geboren am 30. Juli 1973 in Schladming, Steiermark, Österreich
- Nationalität: Österreich
- Status: verheiratet, 1 Kind (geboren: 12. August 1999),

Ausbildung:

- aufgewachsen in: Frauenberg/Admont & Rottenmann, Österreich
- Volksschule: Admont (1979-1981)
  Rottenmann (1981-1983)
- Hauptschule: Rottenmann (1983-1987)
- Berufsbildende Höhere Schule: BBA für Kindergartenpädagogik (1987-1992)
  Matura: Juni 1992
- Immatrikulation an der Technischen Universität Graz: Oktober 1992
- Inskription Technische Physik: Oktober 1993
- Abschluss des ersten Studienabschnittes:"Technische Physik": Mai 1996
- Auslandssemester an der Universität Claude Bernard in Lyon/Frankreich: Jänner - Juni 1998
- Diplomarbeit bei AVL-List GmbH (Motorenentwicklungsfirma) und dem Institut für Experimentalphysik mit dem Thema: "Analyse und Optimierungsvorschläge zur Aufnahme und Auswertung von planarer, Laser induzierten Fluoreszenz am Einzylinderglasmotor"
- Abschluss des Studiums / Diplom für Technische Physik: März 2003
- Beginn der Doktorarbeit an der Universität zu Köln: Jänner 2004

Praktika und Berufserfahrung:

- Sommerjob am Synchrotron ELETTRA in Triest/Italien, Institut für Biophysik und Röntgenforschung:
  Mithilfe bei Aufbau der Small Angle X-Ray Scattering-beamline (SAXS-beamline),
  Juli - Oktober 1995
- Sommerjob am Max-Planck-Institut Garching/Deutschland:
  Kalibrationsmessungen der Transmissionsgitter des Röntgensatelliten AXAF,
  Juli - Oktober 1996
- Sommerjob am Max-Planck-Institut Garching/Deutschland:
  Mithilfe bei der Vorbereitung der Kamera EPIC für den Röntgensatelliten XMM,
  Juli - Oktober 1997
- Sommerjob an der Universität Hawaii, Institut für Astronomie:
  Identifikation und Charakterisierung von Röntgenquellen (ROSAT),
  Juli - Oktober 1998
- Studentenjob bei AVL-List GmbH (Motorenentwicklungsfirma):
  Messung und Auswertung laserinduzierten Fluoreszenzaufnahmen am Einzylinderglasmotor, Oktober 1998 – Juli 1999
- Wissenschaftliche Hilfskraft am I. Pysikalischen Institut der Universität zu Köln:
  Betreuung von Grundpraktika in Physik, Übungsbetreuung zu den Vorlesungen "Mathematik für Naturwissenschaftler", "Experimentalphysik1" und "Experimentalphysik2", seit 2004